Title

Physics-based Probabilistic Failure Modeling of Non-metallic Pipelines in Oil and Gas Applications

Author

Stewart, Theresa Mae

Publication Date

2023

UNIVERSITY OF CALIFORNIA

Los Angeles

Physics-based Probabilistic Failure Modeling of Non-metallic Pipelines in Oil and Gas Applications

A dissertation submitted in partial satisfaction of the
requirements for the degree Doctor of Philosophy in
Materials Science and Engineering

by

Theresa Mae Stewart

2023

ABSTRACT OF THE DISSERTATION

Physics-based Probabilistic Failure Modeling of Non-metallic Pipelines in Oil and Gas Applications

by

Theresa Mae Stewart
Doctor of Philosophy in Materials Science and Engineering
University of California, Los Angeles, 2023
Professor Ali Mosleh, Chair

The use of composite pipelines has grown in recent years as an alternative to steel in the oil and gas industry, due to their excellent corrosion resistance and high specific strength. Among these developments, thermoplastic composite pipes have seen a recent rise in research and use due to their greater flexibility and impact resistance than traditional thermoset-matrix composites. To understand and predict the performance of these materials in the field, studies have derived experimental, analytical, and theoretical estimates of the mechanical and thermal properties of thermoplastic composite pipes (TCP) and reinforced thermoplastic pipe (RTP) in dry conditions, but studies in wet or corrosive environments are currently restricted to the empirical domain. A better understanding of the performance of thermoplastic-matrix composites in marine and water-saturated environments is needed, because 30% of the world's current oil and gas supply is

produced offshore; the offshore portion of the upstream segment of the oil and gas industry has risen dramatically in recent years, and this trend is expected to continue [1], [2].

To address part of this gap in modeling capability, this research used a probabilistic approach to predict degradation rates of the constituent polymer matrix and reinforcement fibers within an individual composite ply given the local temperature and the amounts of absorbed fluids. This method was applied by developing a TCP simulation code, which consists of three major time-dependent processes: 1) absorption of oil- and water-based fluids for each layer of the pipe given spatial and temporal variations in the diffusivity parameters, 2) evaluation of the local composite properties given the amount of degradation to the matrix and fibers during each time window, and 3) prediction of the stresses at each ply under defined thermomechanical loading conditions given the current state of each ply's mechanical properties and subsequent determination of ply failures. The ply failures determined from the third process incur further reduction in the stiffness of the failed ply, resulting in greater amounts of stress applied to the remaining un-failed plies until all plies in the laminate have failed, thus constituting a progressive failure mechanism.

In order to model these processes while accounting for various uncertainties in material and environmental inputs, new methods for estimating certain process factors, such as diffusivity and the extent of composite stiffness and strength reduction following degradation and ply failure, are developed using comparisons to real-world data. Similarly, to verify the validity of each of the three major physical processes in this simulation, the results of each given set of controlled inputs are compared to experimental data on TCP and RTP from various lab and field experiments. It was found that in cases where the observed degradation was low, agreement with the model was generally good, but the model tended to underestimate the amount of degradation

in the more severe cases. Future work will aim to improve the prediction capabilities of this method by adjusting the existing processes in the model and incorporating factors that the model currently does not consider, such as fillers and the pH of absorbed fluids.

Finally, the model presented herein has been implemented as a new module in a pre-existing online application initially developed to predict the reliability of metallic pipes in a real world environment, in order to provide insights to the oil and gas industry on the risks of certain locations. The current implementation for the non-metallic pipes includes a prediction of the failure rates, mechanical stiffness degradation, and fluid absorption for segments of pipe, with plans to add maintenance and sensor placement features in the future.

The dissertation of Theresa Mae Stewart is approved.

Enrique A. Lopez Droguett

Jaime Marian

Jenn-Ming Yang

Ali Mosleh, Committee Chair

University of California, Los Angeles

2023

Dedication

To my family and friends, who made this possible.

Table of Contents

List of Figures

List of Tables

List of Abbreviations

1D, 2D, 3D	One-, two-, and three-dimensional, respectively
API	American Petroleum Institute
BFRP	Basalt-Fiber Reinforced Polymer
CLT	Classical Lamination Theory
DNV	Det Norske Veritas
FEA	Finite Element Analysis
FRP	Fiber Reinforced Polymer
GFRP	Glass Fiber Reinforced Polymer
HCL	Hybrid Causal Logic
HDPE	High-Density Polyethylene
IFP	Institute Francais de Petrole
NACE	National Association of Corrosion Engineers
PA	Polyamide
PE	Polyethelyne
PEEK	Polyetheretherketone
PEKK	Polyetherketoneketone
PP	Polypropylene
PSIM	Pipeline System Integrity Management
PSIM-NM	Pipeline System Integrity Management Non-Metallic Module
PVDF	Polyvinylidene Fluoride
RTP	Reinforced Thermoplastic Pipe
SEM	Scanning Electron Microscope
TCP	Thermoplastic Composite Pipe
TP	Thermoplastic (polymer)

TS	Thermosetting (polymer)
TSF	Time Shift Factor
UMAT	User Material (ABAQUS)
UV	Ultraviolet

Acknowledgements

I would like to express my gratitude to everyone who supported me during my time as a graduate student at UCLA. First, I would like to thank my graduate advisor, Prof. Ali Mosleh, for his support and guidance, and for providing me the opportunity to work as a researcher at the B. John Garrick Institute for the Risk Sciences (GIRS). I would also like to extend my gratitude to Prof. Mosleh for his financial support during my time at UCLA. I would like to thank Prof. Enrique Lopez Droguett, Prof. Jaime Marian, and Prof. Jenn-Ming Yang for their service on my committee.

Additionally, I would like to thank all my colleagues at the institute for their help and support throughout the years. I would like to thank Dr. Mihai Diaconeasa, Agatha Diaconeasa, Arjun Earthperson, Dr. Zahra Mahmoodzadeh, Dr. Wadie Chalgham, and Dr. Marilia Ramos for their support and guidance while I was still determining the direction of my studies as a Ph.D student. I would like to thank Adam Barsotti for his help in understanding and reviewing literature materials. I would like to thank my colleagues and friends Bineh Ndefru and Karthik Sankaran for their help on various modeling and technical problems, as well as providing a supportive group environment. I would like to extend my thanks to Joselyne Saldana for her amazing help and support during my time at GIRS.

I would also like to thank my friends Paula Toth and Ammar Askar for their assistance with python coding, as well as Uzias Rivera and Dr. Wadie Chalgham for implementing the python code into an online software platform.

Finally, I would like to thank my family and friends who supported and encouraged me during my journey as a Ph.D. student.

Vita

Education

2017 B.S. Materials Engineering GPA: 3.3/4.0

California Polytechnic State University, San Luis Obispo

San Luis Obispo, California

Research Experience

Graduate Researcher: The B. John Garrick Institute for the Risk Sciences, UCLA

- Worked with contacts from the System Reliability Group at Jet Propulsion Laboratories (JPL) to design a versatile online system reliability analysis tool. This work included testing of the online software by building system reliability models for existing cubesat and rover missions and comparing to existing analysis methods for validity.
- Developed a COVID-19 community response and spread model along with two other graduate students. This model tracked a population of individuals as they made decisions to participate in several categories of public and private events which could lead to exposure to the COVID-19 virus. The potential effects of different vaccine and quarantine policies on community spread were modeled for various hypothetical scenarios.

Start Date: 2017/06; *End Date:* 2023/06

Supervisor's Name: Prof. Ali Mosleh

Publications

T.M. Stewart, J.A. Martinez, and P.L. Szeto, 2017, "The Relationship Between Structural Parameters and Mechanical Properties of Cactus Spines," *Senior Project report submitted to California Polytechnic State University, San Luis Obispo*

M.A. Diaconeasa, T.M. Stewart, A. Mosleh, B.J. Garrick, 2018, "A Quantitative Risk Assessment Study of the Initiation of an Inadvertent Nuclear War," *Proceedings of The International Workshop on Catastrophic Risk*, Los Angeles CA

B. Ndefru, K. Sankaran, T.M. Stewart, A. Mosleh, A. Earthperson, N. Zawalick, 2022, "Risk-Informed Decision-Making Tool for Covid-19 Community Behavior and Intervention Scenario Assessment," *Proceedings of the International Conference on Probabilistic Safety Assessment and Management*, Honolulu HI

B. Ndefru, K. Sankaran, T.M. Stewart, A. Mosleh, A. Earthperson, N. Zawalick, 2022, "Risk-Informed Decision-Making Tool for Covid-19 Community Behavior and Intervention Scenario Assessment," *Proceedings of the Annual Meeting of the Society for Risk Analysis*, Tampa FL

T.M. Stewart, A. Mosleh, 2023, "Probabilistic Physics of Failure Modeling of Non-Metallic Pipelines in Oil and Gas Applications," *Proceedings of the 69th Annual Reliability and Maintainability Symposium*, Orlando FL

1 Introduction

1.1 Motivation

Steel has long been the material of choice for oil and gas pipes due to its high strength and low cost. Over many years of operation, however, exposure to corrosive fluids degrades the metal pipes, increasing the risk of leaks or bursts. According to a NACE study, the annual cost of corrosion in the oil and gas industry is estimated around \$1.372 billion (AMPP, 2022 [3]), and the risk of corrosion increases further as more oil extraction moves to offshore fields and hostile environments. As a result, production of polymer composite pipes has increased significantly over the last few decades, with particular interest in flexible pipes for use in offshore oil and gas extraction. In addition to corrosion resistance, composite materials have a high strength-to-weight ratio, making them an attractive choice for offshore drilling (Marsh, 2013 [4]; Osborne, 2013 [5]). Composites have been successfully used in construction of offshore platform structures including firewater piping, and in offshore transport of aqueous liquids (Gibson, 2002 [6]); Feih et al., 2004 [7]).

Industry application and testing is currently being performed by several companies worldwide, including GE Oil and Gas, Strohm (formerly Airborne Oil & Gas), Magma Global Limited, and Petrobras. Several experimental, analytical, and numerical studies of thermoplastic composite pipe (TCP) and reinforced thermoplastic pipe (RTP) have been performed to verify fitness for use in the field since these technologies were first introduced to the Oil and Gas industry in the 1990s. However, failure of composite materials, especially considering the viscoelasticity and thermal sensitivity of thermoplastic materials makes behavior prediction complex and highly variable. To date, no comprehensive models linking the plausible degradation and failure mechanisms of TCP and RTP as applied in the oil and gas industry have been made.

1.2 Background

1.2.1 Thermoplastic Composite Pipes

Reinforced polymer pipes are used in structural applications where weight and corrosion resistance are key considerations. Flexible applications such as risers, jumpers, and reeled pipes also require flexibility from the pipes, which can be achieved with a thermoplastic matrix such as in thermoplastic composite pipes (TCP). These applications are shown in Figure 1.1, and a schematic of a TCP is shown in Figure 1.2.

Figure 1.1. a) Riser [8] b) Jumper c) Spooled Pipe [9]

Liners and covers are used to protect the reinforcing laminate plies from environmental degradation and wear and tear. It is advantageous for the liner and cover to be fully bonded to the reinforcing layer. Depending on the application, the reinforcing layer will need to sustain a combination of pressure, axial, flexural, and shear loads in addition to thermal loading. The pipe must also be able to handle cyclic loads as it is pressurized and depressurized, in addition to other cyclic loading from ocean currents or spooling.

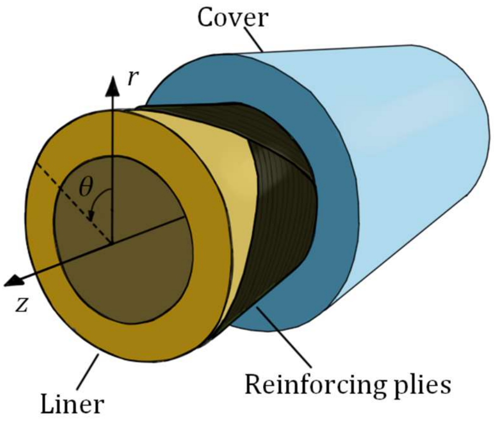

Figure 1.2. TCP Pipe Design with Liner and Cover, displaying radial axes *r, θ*, and *z*

The composite laminate is composed of a set of plies of aligned fibers held together by a polymer matrix. To produce the pipe shape, the fibers are wound around the thermoplastic inner liner either as filaments or in a pre-preg tape, and the outer cover is extruded over the laminate. The liner and cover are made of the same polymer as the laminate matrix so that the three layers can be bonded together (de Kanter and Leijten, 2009 [10]).

A wide variety of fiber and matrix materials may be used in a composite, depending on the desired properties. Some of the most commonly used materials for oil and gas applications are described below.

The most commonly used fibers are E-glass and carbon. Mechanical properties of these fibers are listed in Table 1.1. Carbon fiber offers a significantly higher specific strength and stiffness which allows for thinner cross sections and lower weight for the same loads. Though glass fibers have a lower specific stiffness, this can be an advantage in applications where higher flexibility is required, and glass-fiber composites generally have a higher toughness.

Table 1.1. Mechanical Properties of Carbon and E-glass fibers [11]

Material	*Specific Gravity*	*Tensile Strength (GPa)*	*Specific Strength (GPa)*	*Modulus of Elasticity (Gpa)*	*Specific Modulus (GPa)*
Carbon	1.78-2.15	1.5-4.8	0.7-2.7	228-724	106-407
E-Glass	2.58	3.45	1.34	72.5	28.1

Both materials have low thermal expansion coefficients – 5.0×10^{-6} °C for E-glass and -0.6 to -0.5×10^{-6} °C for carbon fibers in the longitudinal direction and 7.0 to 10.0×10^{-6} °C in the transverse direction. The negative thermal expansion coefficient of carbon fibers can be advantageous in applications with thermal cycling as the fibers can serve to counteract the positive thermal expansion of the matrix. Both glass and carbon fibers are highly environmentally resistant, but carbon fiber composites must ensure the fibers are insulated from contact with metallic components, as they act as a cathode in galvanic corrosion.

1.2.2 History of TCP

Beginning in the 1980s, the aerospace industry was developing thermoplastic composites and fiber placement techniques, in which thermoplastic composite tapes are deposited and fused via a melt-fuse process. Around this time, an early prototype of steel pipe wrapped with a thermoplastic composite was developed by the Institute Francais de Petrole (IFP) and Composites Aquitaine for choke and kill lines, but this technology never became commercialized.

The 1990s saw a rise in development of large-diameter carbon fiber/epoxy pipes for offshore use, but these projects never became widely commercialized. Reinforced thermoplastic pipes (RTP) were first introduced to the offshore oil and gas industry in the 1990s, with TCP being introduced in the late 2000s [12].

Early projects for TCP include designs and manufacturing processes for spoolable, flexible deepwater risers being developed by ABB and a collaboration between Soficar, Doris, Freyssinet and Total. A joint industry program between Shell, Statoil, Total, BP, BG Group, Petrobras, Chevron and SBM Offshore was launched in 2009 to design, manufacture, and test a carbon fiber/PA11 riser (Kremers, 2022 [13]).

Airborne piloted a continuous offshore downline production facility in 2010 that was successfully implemented by Dutch contractor Van Oord. Airborne would later invest in a full-scale production site for TCP, which initially produced jumpers and downlines before moving to more demanding applications like flowlines and risers. Airborne, through its dedicated company Airborne Oil & Gas continues to develop a range of materials, from lower cost Glass/PE pipes to high-performance Carbon/PVDF pipes. Another major developer for TCP, Magma Global, began development in 2010 for a concept similar to Airborne, but with a different manufacturing process and end-fitting designs, as well as a focus on Carbon/PEEK (Kremers, 2022 [13]).

Standards for composite usage in offshore environments have been published by both DNV [14], [15] and API/ISO [16], [17]. The DNV standard was initially published in 2015 to address the lack of a global design and qualification standard for TCP, and aid in commercialization of these materials.

For offshore applications, TCP has been tested for 3500m (approximately 11,500 ft) water depth (van Onna, de Kanter, and Steuten, 2012 [18]) for ultra-high-pressure loads (over 70 MPa/10000 psi). Low pressure reinforced thermoplastic polymer (RTP) pipes have been applied in oilfields with generally good results over a 10 to 15-year period (Qi et al, 2011 [19]; 2012 [20]). As the requirements are not as high for onshore pipes, the less expensive unbonded RTPs are more commonly used.

1.3 Scope

The scope of this research covers bonded thermoplastic composite pipes (TCP) and reinforced thermoplastic pipes (RTP) made from polypropylene (PP), polyethylene (PE), or polyamide (PA) matrices and carbon or glass fibers. Pipes will be subject to possible combinations of pressure, axial, and torsion loading as well as thermal gradients and exposure to fluid (internal and external) which may contain abrasive elements. Temporal variation in loading and environmental conditions on the inside and outside of the pipe are considered in this model, and spatial variations are observed my modeling differences in conditions between segments.

This work will not cover degradation resulting from prolonged sun exposure or other forms of radiation. Extreme, non-design loads such as natural disasters will not be considered in this analysis.

1.4 Pipe Failure Modes

This section describes the various failure modes and mechanisms that may occur in oil and gas applications for thermoplastic composite materials. An overview of this section is provided in Table 1.2.

Table 1.2. Root Causes of Failure

Failure Mode	*Failure Mechanisms*	*Factors*	*Relevant Applications*
Burst	Fiber failure, Yielding, Wear Softening	Internal pressure, Temperature, Thermomechanical Cycling, Fluid exposure	Risers, jumpers, line pipes, spoolable pipes
Collapse	Fiber failure, Matrix cracking, Yielding Softening	External pressure, Temperature, Thermomechanical Cycling, Fluid exposure	Risers, spoolable pipes
Buckling	Fiber failure, Matrix cracking, Delamination, Yielding Softening	Compression loads, flexure loads, Temperature, Fluid exposure	Risers, jumpers, spoolable pipes
Puncture, scratches	Wear, Yielding Softening	Impact, out-of-plane loads, Temperature	Risers, jumpers, line pipes, spoolable pipes
Ovalization	Fiber failure, Yielding softening	Temperature, Fluid exposure	Risers, jumpers, line pipes, spoolable pipes
Excessive deformation	Fiber failure, Yielding Softening	Temperature, Fluid exposure	Risers, jumpers, line pipes, spoolable pipes
Loss of fluid tightness	Matrix cracking, Liner/cover failure, Wear	Fluid exposure, Cycling, Abrasive elements, Impact	Risers, jumpers, line pipes, spoolable pipes

Thermoplastic composites are highly susceptible to temperature changes, which is their main limiting factor in application. Exposure to high temperatures or temperature cycling may cause mechanical property changes and induce thermal strains which increase the likelihood of yielding and cracking and ultimately the likelihood of catastrophic failure.

1.4.1 Fracture

Failure of anisotropic materials needs to be evaluated not just by the type of loading (tensile, compressive, or shear) but by the loading direction relative to the material's local axis. For a single unidirectional ply, the axes 1, 2, and 3 are defined as longitudinal (parallel to fibers), transverse (in plane perpendicular) and out-of-plane.

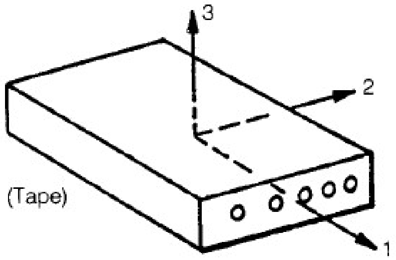

Figure 1.3. Composite Axes

Evaluation of stresses in an individual composite ply is performed using classical lamination theory (CLT). This theory assumes the laminate deforms under plane stress, and the strain experienced by an individual ply is the same as the strain experienced by the laminate as a whole. This allows the stress-strain relationship for a ply *k* to be defined by Equation 1.1.

$$\begin{bmatrix} \sigma_1 \\ \sigma_2 \\ \tau_{12} \end{bmatrix}^{(k)} = \begin{bmatrix} \bar{C}_{11} & \bar{C}_{12} & 0 \\ \bar{C}_{12} & \bar{C}_{22} & 0 \\ 0 & 0 & \bar{C}_{66} \end{bmatrix}^{(k)} \begin{bmatrix} \varepsilon_1 \\ \varepsilon_2 \\ \gamma_{12} \end{bmatrix}^{(k)} \tag{1.1}$$

1.4.1.1 In-Plane

Depending on the axis and type of load, the following failure modes in Table 1.3 will be dominant for in-plane loads.

Table 1.3. In-Plane Failure Modes

Load	*Direction*	*Failure*
Tensile	Longitudinal	Fiber breakage
Tensile	Transverse	Matrix cracking
Compressive	Longitudinal	Fiber crushing
Compressive	Transverse	Matrix yielding
Shear	Any	Shear cracking

The simplest way of evaluating failure of a composite is with the maximum stress or maximum strain criterion. These methods state that failure will occur when at least one stress (or strain in maximum strain) in axis 1 or 2 exceeds the ultimate stress (or strain).

For example, Eq. 1.2a describes the ultimate stress criterion for tensile stress in directions 1 and 2, and Eq. 1.2b describes the ultimate strain criterion.

$$\boldsymbol{\sigma_1 > F_{1t} \qquad \sigma_2 > F_{2t}} \tag{1.2a}$$

$$\boldsymbol{\varepsilon_1 > \varepsilon_{1t}^u \qquad \varepsilon_2 > \varepsilon_{2t}^u} \tag{1.2b}$$

In many cases, loading is not exactly along the axes described in Figure 1.3 and it is necessary to use a failure criterion which accounts for the possibility of multiple failure modes occurring. Several competing theories exist to describe the interactions between these failure modes, the most popular being Hashin, Tsai-Hill and Tsai-Wu. The failure envelopes for the Tsai-Hill and Tsai-Wu criteria are shown in Figure 1.4a and 1.4b, respectively.

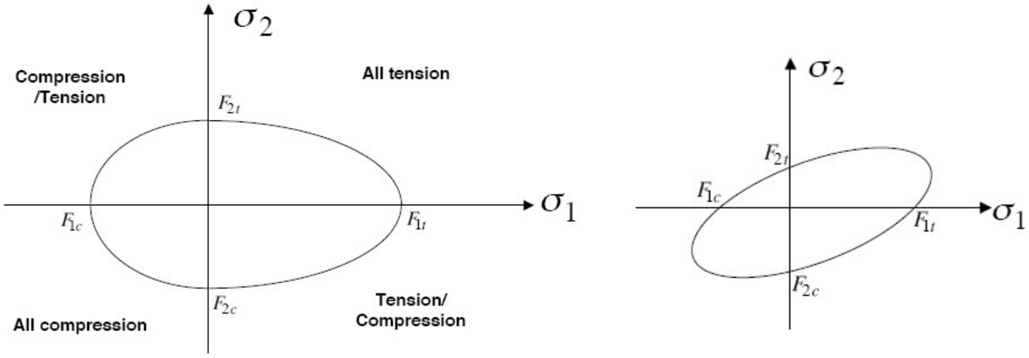

Figure 1.4. a) Tsai-Hill Failure Envelope **b) Tsai-Wu failure envelope**

Figure 1.5. Delamination [78]

Following failure of one ply, progressive failure of other plies can be evaluated by assuming the failed ply cannot carry a load and redistributing the load to the remaining plies. This process can be repeated until the entire laminate fails.

1.4.1.2 Out-of-Plane

In most applications, it is not sufficient to evaluate failures only from in-plane stresses. Delamination is a major cause of failure in composites that can remain and grow undetected until severe damage has occurred. Delamination is caused by interlaminar stresses ($\sigma_3, \tau_{13}, \tau_{23}$) which may be the result of:

- Material discontinuities at free edges, holes, and interfaces between plies with different properties (e.g. Poisson's ratio)
- Structural loading of a curved laminate
- Impact damage

Due to the high dependence of interlaminar stress on geometry, these stresses usually need to be evaluated with finite element and finite difference methods. Once the interlaminar stress is known, predicting the initiation of delamination can be evaluated through either a stress-based criterion such as Kim-Soni or the Quadratic Delamination criterion, or by a fracture mechanics approach.

Delamination has three fundamental failure modes which can occur in combination:

1. Opening
2. In-plane shearing
3. Tearing or scissoring shear

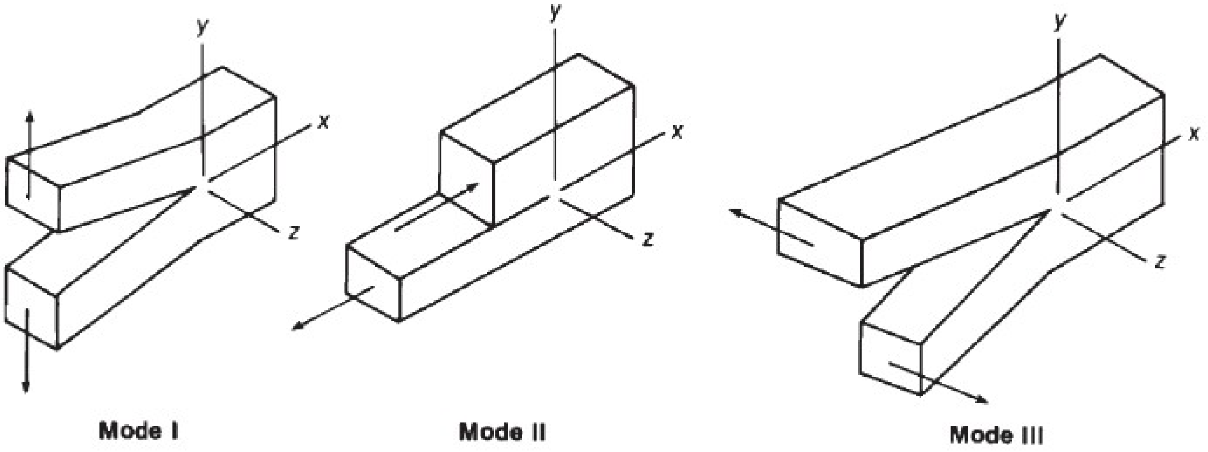

Figure 1.6. Delamination Modes

Under total delamination (complete separation of one ply from another), it can be assumed that there is no load transfer between the disconnected plies and the laminate stiffness can be evaluated by the portion of undamaged laminate remaining. For partially delaminated laminates, the stiffness reduction can be evaluated using the portions of damaged area relative to the undamaged area (see Figure 1.7).

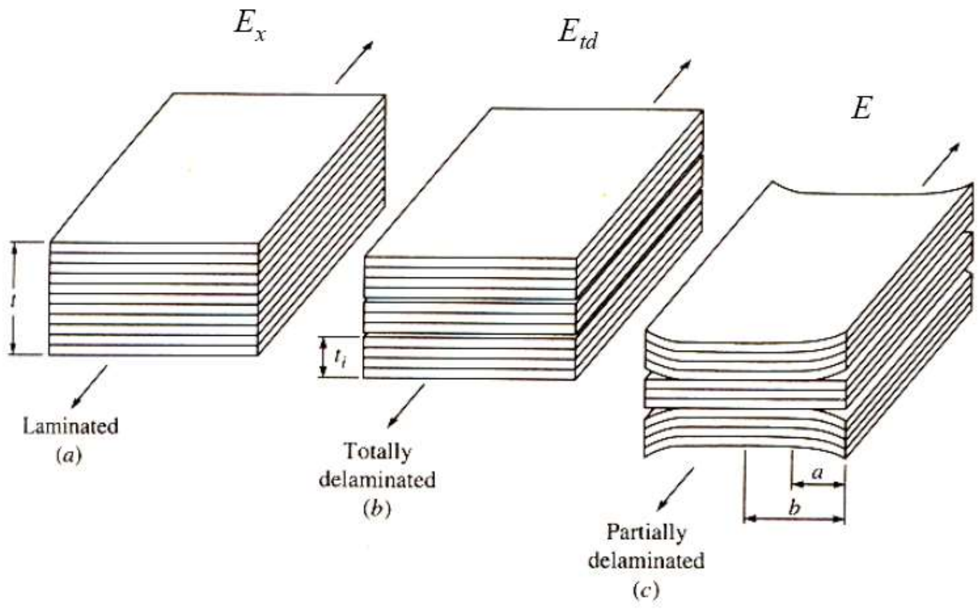

Figure 1.7. Undamaged, total, and partial delamination of a composite laminate [21]

1.4.1.3 Fracture of composites

Unlike in isotropic materials, crack size cannot be taken as a universal measure of damage. Instead, it is critical to consider the damage zone ahead of the crack, which may encompass fiber pull out, fiber rupture, interfacial debonding, matrix deformation, and matrix cracking.

In pipelines, fracture failures most commonly present in the form of burst, collapse, or buckling.

1.4.1.4 Collapse and Burst Failures

Pressure is the main service load of pipelines. Burst and collapse are defined as the failure of pipes under internal and external pressure, respectively.

Figure 1.8. Burst under internal pressure [22]

Figure 1.9. Collapse under external pressure [22]

While pressure, which is an out-of-plane load, would initially seem to be an especially dangerous type of loading for composites, laminated pipes can be designed to distribute this load so that it can be withstood safely.

Under axisymmetric loading, segments of the pipe may be evaluated on only the radial axis, *r*, as defined in Figure 1.2. The problem can be solved analytically as with in-plane loading by using the internal and external pressure as boundary conditions. For example, if there is internal pressure P_0 and no external pressure, the boundary conditions are given in Equation 1.3.

$$\boldsymbol{\sigma_r^{(1)}(r_1) = -P_0} \qquad \boldsymbol{\sigma_r^{(N)}(r_{N+1}) = 0} \tag{1.3}$$

Assuming perfect bonding between layers, interface continuities used in the solution are given in Equation 1.4.

$$\sigma_r^{(k)}(r_k) = \sigma_r^{(k+1)}(r_k) \qquad u_r^{(k)}(r_k) = u_r^{(k+1)}(r_k) \tag{1.4}$$

Lastly, the axial tension and torque integrals are given in Equation 1.5.

$$\begin{gathered} 2\pi \sum_{k=1}^{N} \int_{r_k}^{r_{k+1}} \sigma_z^{(k)}(r) r dr = \pi r_0^2 P_0 \\ 2\pi \sum_{k=1}^{N} \int_{r_k}^{r_{k+1}} \tau_{z\theta}^{(k)}(r) r^2 dr = 0 \end{gathered} \tag{1.5}$$

1.4.2 Deformation

Some deformation of the structure is tolerated and accounted for in the design. If this deformation becomes excessive, however, it can weaken the walls of the pipe and alter the geometry. Since most thermoplastic matrices are made from ductile materials, deformation will often occur before fracture and can be used as an early indicator of failure.

Deformation can be in the form of axial elongation or compression, torsion, bending, ovalization, or diameter changes. Plastic deformation can accumulate over cyclic loading.

Ovalization is the stretching or squishing of an initially circular pipe in one direction. It is detrimental to the performance of the pipe as it increases the stress in one direction. Measurement of ovality is defined by the API [23] using Equation 1.6.

$$Ovality = \frac{D_{max}-D_{min}}{D_{max}+D_{min}} \tag{1.6}$$

1.4.3 Buckling

Buckling is a local failure which can occur under compressive stresses from external pressure, bending, axial compression, or thermal deformation.

Buckling analysis is carried out with a finite-element methods. Modeling efforts have been carried out by Wang et. al [24] and Yu et. al [25] to predict the maximum allowable stress, critical bending angle, and post-buckling behavior of TCP considering nonlinear behavior of the polymer matrix. Hastie et. al performed modeling of TCP under combined bending and thermal stress [26]. These models generally consider a pipe with one fixed end and one end which is free to rotate, such as in Figure 1.10.

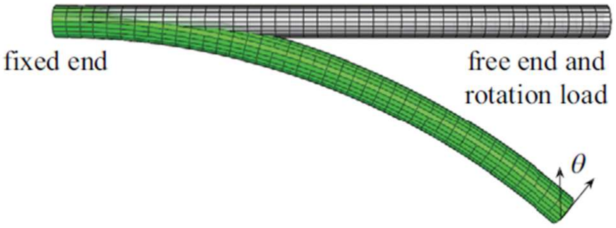

Figure 1.10. Boundary conditions from Wang et. al [24]

1.4.4 Wear

Exposure to fluid flow and abrasive elements gradually removes material. Similar to deformation, this process is gradual and some degree of material removal is usually accounted for in the design. Over time, thinning of the pipe wall will increase the likelihood of failure, so monitoring of the pipe thickness to detect areas of significant material removal is needed.

1.4.5 Liner and cover failure

The polymer liner and cover protect the composite laminate from environmental degradation and wear. They are susceptible to environmental degradation including fluid absorption, wear, UV degradation, oxidation, and thermal damage. The liner or cover is considered failed when it can no longer maintain fluid tightness, which can be due to:

- Polymer fracture
- Polymer yielding
- Debonding
- Crazing
- Permeability change

1.5 Aging Mechanisms

1.5.1 Mechanical Aging

Composite materials are susceptible to fatigue from mechanical and thermal stresses which can be amplified by chemical agents. Fatigue damage may present in the form of matrix cracking, fiber cracking and breaking, and delamination. Flexible matrices, such as those made from thermoplastic polymers, offer a higher resistance to fatigue damage.

1.5.1.1 Creep

Creep is defined as deformation of materials at elevated temperatures and low to moderate stress over an extended period of time. Creep affects all types of materials, but it can be an especially major issue in composites which have matrices with low T_g or T_m, which is true of most thermoplastic polymers. Composite creep behavior is highly related to the stress level and temperature. When the stress level is higher than 50% of the ultimate stress, the secondary creep phase is significantly shortened and rupture occurs quickly.

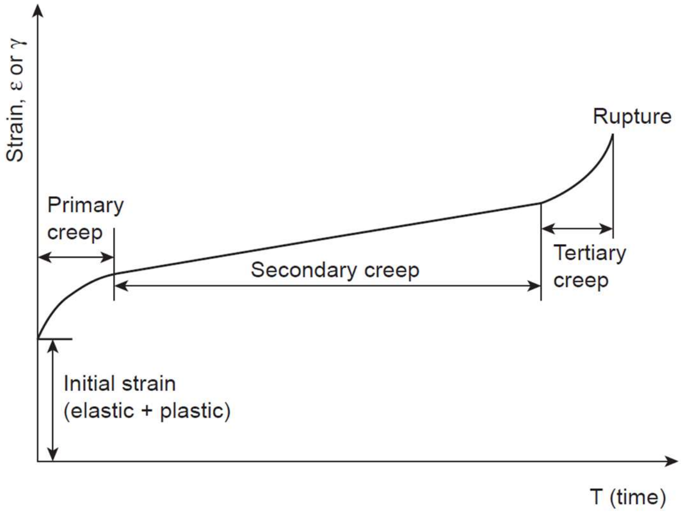

Figure 1.11. Creep strain vs. time [27]

Creep occurs in three stages:

Primary creep: Elastic and plastic deformation, decreasing rate over time; occurs very quickly upon loading

Secondary creep: Steady-state, rate is relatively constant with time

Tertiary creep: Acceleration of creep until failure – visible voids, cracks, etc. form

Several models exist to predict creep deformation in thermoplastic composites with good results. Several models for predicting creep deformation in thermosetting and thermoplastic composite pipes are described below.

Findley's power law model (Eq.1.7) was developed for polymers. It has been verified for thermosetting composites to predict short term creep data and the secondary creep phase. The parameters *m* and *n* are experimentally determined.

$$\varepsilon = \varepsilon_0 + m(t)^n \tag{1.7}$$

The Boltzmann-Volterra model (Eq. 1.8) defines a stress-strain relationship for viscoelastic polymers, where J_0 is the time-dependent creep compliance and *K* is the creep kernel function.

$$\varepsilon = J_0\sigma(t) + \int_0^t \sigma(s)K(t-s)d\tau \tag{1.8}$$

The kernel function *K(t-s),* shown in Eq. 1.9, characterizes strain developing after load application. A_i and τ_i are a discrete relaxation spectrum.

$$K(t-s) = \sum_{i=1}^{k} \frac{A_i}{\tau_i} e^{-\frac{t-s}{\tau_i}} \tag{1.9}$$

The Schapery model uses a nonlinear viscoelastic theory from the fundamentals of irreversible thermodynamic principles to define an analytical form of time-stress superposition. For a case of uniaxial loading under isothermal conditions, the creep strain is defined as shown in Eq. 1.10.

$$\varepsilon = g_0 D_0 \sigma + \int_0^t D_t(\psi - \psi') \frac{dg_2\sigma}{d\tau} d\tau \tag{1.10}$$

In this model, D_0 is the initial creep compliance and D_t is transient creep compliance. ψ and ψ' are reduced time parameters and g_0, g_1, and g_2 are stress-dependent material parameters. This model becomes the Boltzmann superposition model for linear viscoelastic materials under low stress conditions. This model has shown good results for predicting creep of thermoplastic materials but there has not been any report of application to FRPs so far.

The strain energy model was developed specifically for the creep response of FRPs by GangaRao and Liang [28]. In this model, the energy release rate per unit time *dU/dt* is found to be constant and characteristic of the constituent materials under similar loading conditions (e.g. bending, compression, or tension). This model is described in Eq. 1.11, where ε_{max} is the maximum bending strain and ε_{ult} is the static ultimate strain at failure. The parameters *a* and *b* are empirically determined creep coefficients.

$$\frac{dU}{dt} = a\left(\frac{\varepsilon_{max}}{\varepsilon_{ult}}\right)^b \tag{1.11}$$

The creep life is then defined by Eq. 1.12, where U_J is the strain energy expended by a GFRP composite at time *t* after sustained load application, and U_0 is the strain energy under three-point bending of GFRP at the initial load application.

$$\varepsilon = \frac{U_J - U_0}{a\left(\frac{\varepsilon_{max}}{\varepsilon_{ult}}\right)^b} \tag{1.12}$$

1.5.1.2 Fatigue

Fatigue is defined as progressive damage caused by cyclic loading at loads below the ultimate or even yield stress of a material. Fatigue damage in composites is generally not in the form of crack growth as in metals, but is a distribution of damage to the fiber, matrix, and interfaces spread over the material. Damage mechanisms from fatigue in composites include:

- Fiber fracture
- Matrix cracking
- Matrix crazing
- Fiber buckling
- Fiber matrix debonding
- Delamination

Fatigue damage is highly dependent on matrix properties, and environmental changes (such as temperature or moisture) will have significant impacts on the lifetime of the material. Continuous fiber composites generally perform well under fatigue, but their performance is highly dependent on loading direction.

Due to the complexity of fatigue failure in composites, most life assessment methods are empirical. Both types describe damage as some function of past damage, stress (σ), strain (ε), and cycles. A generic form of this function is shown in Eq. 1.13.

$$\frac{dD}{dN} = f(D, \sigma_i, \varepsilon_i, N, \dots) \tag{1.13}$$

Two main categories of these empirical models exist: residual strength models, and residual stiffness models.

Residual strength models require testing a sample to failure to measure. The model developed by Reifsnider and Stinchomb assumed the strength degraded as a power function of *N*.

Stiffness or modulus degradation do not require destructive testing and use modulus reduction below an allowable threshold as a measure of failure. A modification of this approach was developed by Hwang and Han, which defines failure as occurring when the fatigue resultant strain reaches the static ultimate strain. This modification allows for consideration of accumulated strain from cycling. The degradation equation for this approach is described in Eq. 1.14, where *A* and *c* are material constants.

$$\frac{dE}{dN} = -Acn^{c-1} \tag{1.14}$$

1.5.2 Chemical Aging

Chemical aging includes changes in the physical and chemical structure of the composite material caused by the exposure, uptake, and reactions with external media. Depending on the nature of the fluid, polymer chemistry, and fiber type, the form and degree of this degradation may vary greatly.

1.5.3 Moisture Uptake

Though many polymeric materials and their composites are resistant to electrochemical corrosion, uptake of moisture can cause changes in matrix properties and degrade bonds between the matrix and fibers. Condensation polymers, such as polyamides, are even more susceptible to moisture exposure due to their solubility in water. As moisture uptake is a diffusion process, the severity of these effects is dependent on the temperature. Wet-dry and freeze-thaw cycles can accelerate the degradation from moisture uptake.

Fiber interactions with moisture vary as well. Glass fibers, for instance, are resistant to chemical changes from exposure to water, but physical changes to the surrounding matrix and degradation of bonds may damage the fiber or cause debonding. Carbon fibers, on the other hand, act as a cathode in a galvanic cell which can corrode metals in contact with the composite [29].

As mentioned earlier, condensation polymers used in matrices and aramid fibers are particularly susceptible to degradation from moisture exposure. This is because of the polar structure of the polymer molecules, which allows water to attach to the polymer, increasing moisture uptake. These materials can also undergo hydrolysis, a phenomenon in which the chemical bonds are broken down, resulting in significant reduction in mechanical properties and even dissolution of the material [30].

1.5.3.1 Moisture uptake models

The most basic and frequently used model for diffusion in composite pipes is the one-dimensional Fickian diffusion equation, shown in Equation 1.15. This equation relates the time dependence and space dependence of the concentration by the diffusivity parameter of the fluid in the material, *D*.

$$\frac{\partial c}{\partial t} = D\frac{\partial^2 c}{\partial x^2} \tag{1.15}$$

The moisture uptake from 1D Fickian diffusion is calculated according to Equation 1.16. The moisture content at any time *t* is calculated relative to the ultimate moisture content M_∞ which is measured experimentally.

$$M_t = M_\infty\left\{1 - \frac{8}{\pi^2}\sum_{n=0}^{\infty}\frac{1}{(2n+1)^2}\exp\left[-\frac{Dt}{h^2}\pi^2(2n+1)^2\right]\right\} \tag{1.16}$$

An expansion of the Fickian model, shown in Equation 1.17, was proposed by Berens and Hopfenberg [31] which considered the moisture uptake contribution from polymeric relaxation ($M_{t,R}$) in addition to Fickian diffusion ($M_{t,F}$). This is particularly important at higher temperatures where relaxation becomes significant.

$$M_t = M_{t,F} + M_{t,R} \tag{1.17}$$

The Fickian contribution is described by Equation 1.16 and the relaxation contribution $M_{t,R}$ is determined by Equation 1.18, where $M_{\infty,R}$ is the ultimate relaxation moisture content.

$$M_{t,R} = M_{\infty,R}[1 - \exp(-kt)] \tag{1.18}$$

Langmuir's model for water absorption assumes that absorption occurs in two distinct but related phases. First, water molecules in the mobile phase are absorbed into the material with diffusion coefficient D_γ. Then, molecules are bound to the molecular structure of the polymer with a probability γ and become unbound with a probability β. The classic form of this model is shown in Equation 1.19.

$$M_t = M_\infty \left(\frac{\beta}{\gamma + \beta} e^{-\gamma t} \left[1 - \frac{8}{\pi^2} \sum_{l=1}^{\infty(odd)} \frac{e^{-\kappa l^2 t}}{l^2} \right] + \frac{\beta}{\gamma + \beta} \left(e^{-\beta t} - e^{-\gamma t} \right) + \left(1 - e^{-\beta t} \right) \right) \tag{1.19}$$

$$2\gamma, 2\beta \ll \kappa \quad \kappa = \pi^2 D_\gamma / (2\delta)^2$$

Where δ is half of the sample thickness and D_γ is measured experimentally. This model is found to have better agreement when the polymer matrix has a high affinity for the fluid. A comparison of single phase Fickian absorption with Langmuir two-phase absorption is shown in Figure 1.12.

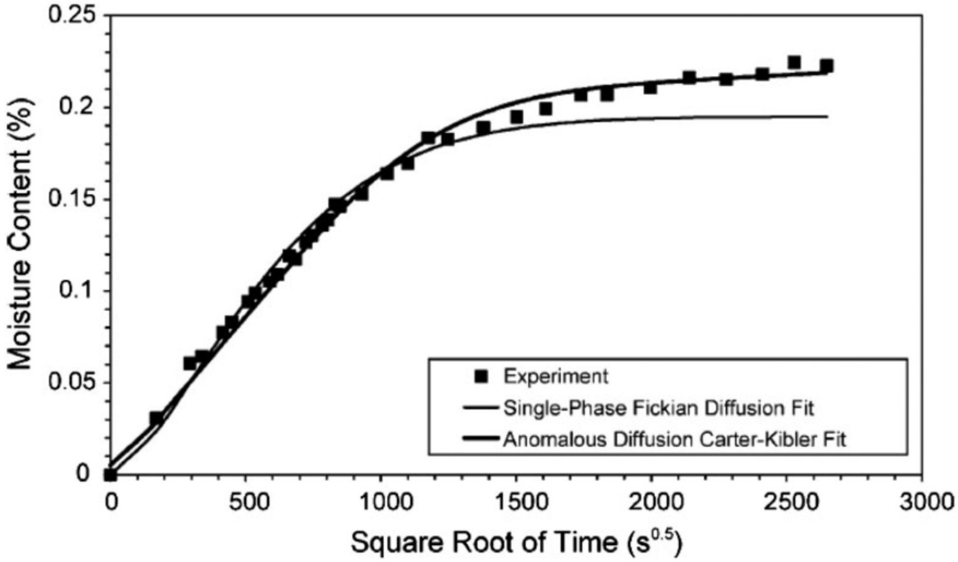

Figure 1.12. Comparison of Fickian and Langmuir absorption predictions with experimental data [32]

1.5.4 Effect of pH

Prolonged exposure to acidic and alkaline environments can cause severe damage to resins, fibers, and bonds of composite materials. Notably, this exposure can break down chemical bonds of both the fiber and matrix materials, resulting in cracking and strength reduction [33]. The susceptibility to alkaline or acidic environments is highly dependent on the constituent materials.

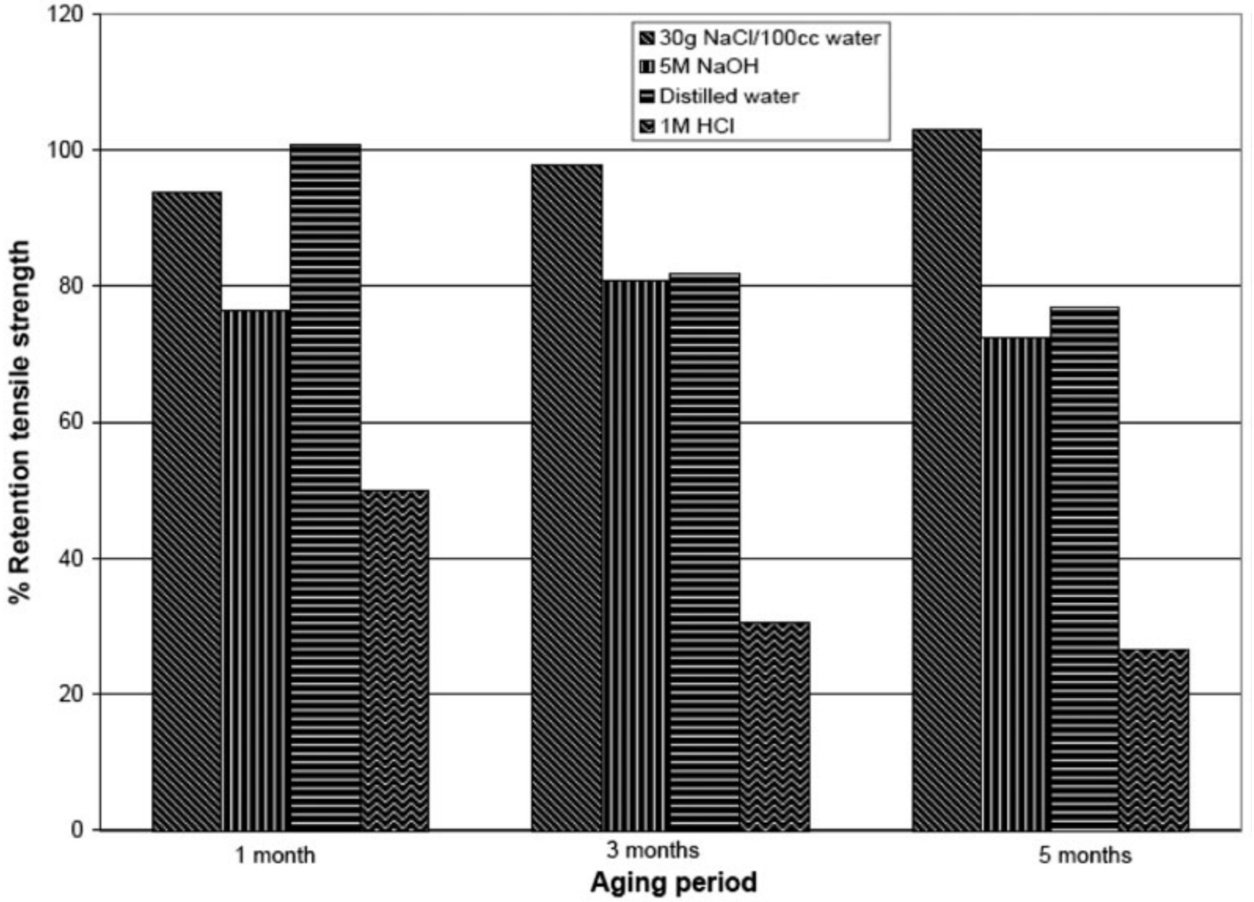

Figure 1.13. Effects of seawater, distilled water, alkaline solution, and acidic solution on glass fiber reinforced epoxy [34]

The effect of acidic and alkaline solutions on strength retention is usually modeled with an Arrhenius model, assuming that the dominant degradation mechanism does not change for the exposed time and temperature range.

If the Arrhenius time-concentration relationship can be assumed as valid for the full concentration range, a time shift factor (TSF) developed by Zhou et al. [35] can be used to account for changes in pH with time. This TSF is described in Equation 1.20, where 10^{-pH} is ion concentration, 10^{-pHr} is reference ion concentration.

$$TSF = e^{A\left(10^{-pH}-10^{-pH_r}\right)} \tag{1.20}$$

Wu et al. [36] developed a TSF between different temperatures to predict long-term performance of basalt fiber reinforced polymers in alkaline solutions with good results. This factor is shown in Equation 1.21.

$$TSF = \exp\left[\frac{E_a}{R}\left(\frac{1}{T_0} - \frac{1}{T_1}\right)\right] \tag{1.21}$$

1.5.5 *Thermal Aging*

Many polymers are highly susceptible to thermal degradation even at relatively low temperatures. This is especially true for thermoplastic matrix composites. Furthermore, differing thermal expansion between the fibers and matrix or between the composite and other connected parts may result in damage to the interface.

In general, composite materials should not operate at temperatures greater than 20 °C below their glass transition temperature. [33]

Changes in temperature and temperature gradients result in thermal stress which may cause cracking or breaking. Semicrystalline polymers may also undergo annealing at high temperatures, leading to changes in their mechanical behavior. At very cold temperatures, differential thermal expansion and freeze-thaw cycles can reduce durability. This can occur between fiber and matrix and composite and connected components such as metal joints.

1.5.5.1 *Hydrothermal*

Diffusivity is dependent on temperature, meaning that at higher temperatures moisture absorption occurs more quickly and can attain higher saturation levels. Additionally, water damage to the polymer matrix can cause plasticization which reduces the glass transition temperature, T_g.

Conversely, resins that are cured at low temperatures may undergo post-curing during hygrothermal exposure.

1.5.5.2 Low Temperatures and Freeze-Thaw cycles

At very low temperatures (below 0°C), polymers become more glassy. This has some advantages for stiffness, but also increases the likelihood of matrix cracking. This is especially problematic in freeze-thaw cycling, where frozen water causes crack growth and debonding which further enables more water to enter during warm cycles. These changes primarily impact transverse and shear properties of composites as fibers are resistant to temperature changes.

1.5.5.3 Temperature-Dependent Mechanical Properties

Most models use empirical data gathered over the application's temperature range to obtain temperature dependent properties. Data requirements can be reduced using a model developed by Bai et al. [37] for prediction of laminate properties from data obtained about the glassy (g), leathery (l), rubbery (r), and decomposed (d) states of the matrix. This relationship is shown for a given property P and conversion rate α in Equation 1.22.

$$P_m = P_g \cdot \left(1 - \alpha_g\right) + P_l \cdot \alpha_g \cdot (1 - \alpha_r) + P_r \cdot \alpha_g \cdot \alpha_r \cdot (1 - \alpha_d) + P_d \cdot \alpha_g \cdot \alpha_r \cdot \alpha_d \tag{1.21}$$

This equation can be further reduced for certain properties. For example, the Young's Modulus of the rubbery and leathery states are nearly equal, and decomposition of resin polymers has a minimal effect on stiffness. Therefore, the above is reduced in Equation 1.23.

$$E_m = E_g \cdot \left(1 - \alpha_g\right) + E_r \cdot \alpha_g \cdot (1 - \alpha_d) \tag{1.22}$$

For many thermoplastic polymers, melting occurs before decomposition. This would require modification of the above equations to account for this phase.

1.5.6 UV radiation

If the material is exposed to the sun, photochemical degradation will occur over time leading to discoloration and reduction of molecular weight of molecules on the surface. This damage can be easily seen in plastic components that are left outside, such as in Figure 1.14. These damaged areas act as stress concentrators which may initiate cracks and are more susceptible to wear and water absorption. The changes are almost entirely in the matrix dominated properties.

Figure 1.14. UV Degradation of a plastic part [38]

2 Existing Modeling Work

ASO and DNV standards for reinforced thermoplastic pipes (RTP) and thermoplastic composite pipes (TCP) have described failure modes as described in Section 1.4. Failure modes of composites have also been described by Jha et al. [39] in a failure modes and effects analysis. Some of these failure modes have been investigated through experimental work to identify the conditions under which they might occur, whereas others have not. Armed with these as well as expert opinion, models for some failure modes have been developed. The aim of this chapter is to describe these experimental investigations and modeling efforts. Accordingly, this synthesis of prior work will set the stage for the original contributions to the body of knowledge that are being developed in this research.

2.1 Experimental Work

This section describes prominent experimental studies that have been performed on thermoplastic composites and reinforced thermoplastic pipes. Much of this work is used to examine the performance of proposed designs for use in riser, line pipes, or jumper applications and is tested according to the specifications of the application.

Mazur et al. (2014, [41]) studied the aging of high-performance carbon fiber reinforced PEKK thermoplastic composites under a combination of UV radiation, elevated temperature, and moisture using dynamic mechanical analysis. This study found that the most significant changes to the material’s viscoelastic properties occurred under the UV radiation weathering conditions, with a decrease in storage modulus of 40GPa to 10GPa, and a reduction in the glass transition temperature from 147° C to 105 °C. Moisture absorption tests found good agreement with Fickian diffusion models, with saturation being reached in about two months.

Arhant et al. (2015, [42]) investigated the viability of less expensive thermoplastic polymers (polyamides, compared to PEEK) under seawater conditions typical of submersible vehicles and test equipment. The study analyzed the diffusion of seawater into a carbon fiber reinforced polyamide composite through degree of saturation. Compression and pressure vessel implosion tests were performed on dry and saturated samples. Although the implosion tests were inconclusive due to manufacturing defects, under the compression bend tests the saturated polyamide composite samples were only 60% as strong as the dry samples.

A study by Gabrion et al. (2016) examined the effects of combined thermal and mechanical loading and environmental factors on the behavior of thermoplastic-matrix composites. It was found that as the temperature increased from ambient to about 200C, tensile strength decreased by about 8%, fatigue strength at 40-million cycles decreased by about 40%, and interlaminar shear strength decreased by about 65%. When the temperature was increased close to the glass transition temperature, the tensile strength was reduced by about 33%. Most samples failed in a brush-like manner due to fiber-matrix debonding, but some of this was attributed to limitations in the experimental set-up. Thermal expansion was found to be highly anisotropic, and weight loss was found to be heavily impacted by the environment [43].

Eftekhari and Fatemi (2016) investigated the tensile behavior of thermoplastic composite sample bars under high temperatures and moisture exposure. This study investigated the hygrothermal effects on the elastic modulus, ultimate, and yield strength of talc-filled polypropylene, 30% short glass fiber-reinforced polypropylene, 30% short glass-fiber reinforced polyamide-6,6, and 20% short glass-fiber reinforced polyphenylene ether/polystyrene resin [44].

Bahtui et al. performed a combined pressure and bending analysis on thermoplastic composite riser designs. Qualification processes used for m-pipe, a Magma Global Ltd. TCP design, are described. [45]

Robert, Roy, and Benomokrane (2020) investigated the effects of tap water, salt solution, and freeze/thaw cycling on PP/glass samples at 23, 50 and 70 °C. Flexural strength of the specimens were measured before and after aging, and scanning electron microscopy (SEM) was used to characterize the effects of aging on the microstructure [46].

Bel Haj Frej et al. (2021) studied thermoplastic (TP) and thermosetting (TS) composites aged in deionized water at 70 °C. The diffusion behavior, microstructural changes, and permanent damages to the composites are measured until water absorption reaches a plateau. Tensile properties before and after aging were found to be similar, with only a 6% decrease in the tensile modulus of the TP composite. Shear properties were more significantly impacted, with the ultimate stress at failure being reduced around 17% after aging. Notably, the yield stress and strain level at yield were relatively unchanged, with the degradation occurring for the plastic behavior [47].

Bakar et al. (2021) assessed the performance of a 4-inch RTP exposed to lateral loading to assess the tolerance for accidental damage with regard to burst capacity. Two primary failure modes were observed: single unit and ply-by-ply failures. The former of these modes indicate that the indentation from lateral loads did not disturb the bonding between layers, while the latter failure mode indicates debonding [48].

Spencer (2021) evaluated the shear and interfacial failure modes in fiber-reinforced polypropylene and carbon fiber-reinforced polyamide. The effect of continuous water and oil exposure, compression failure and fiber density was studied. Stand-out results are that the

C/Polyamide solution was strengthened by the oil solution, and that the degradation of the matrix due to water is not homogeneous around the circumference of a fiber, leading to novel failure modes. Spencer also presents an extensive literature review and a novel method of testing the pushout failure mode in fiber-reinforced composites. [49]

Existing experimental work has achieved a wide coverage of loading types and aging mechanisms. However, there remains a lack of comprehensive data on large sample sizes of composites of a variety of matrix and fiber types under a spectrum of conditions that are expected for a given application.

2.2 Thermomechanical Modeling

Modeling mechanical behavior of thermoplastic composites poses a unique challenge due to the combined anisotropy of composite materials with the nonlinear mechanical response characteristic of thermoplastic polymers. Several studies have proposed methods of describing the response of TCP and RTP considering either the anisotropy, nonlinearity or both. A large number of these studies have focused on bending and internal pressure as they are the primary loads for flexible pipes on-shore. Others have focused on the effects of external pressure, which is a critical consideration for subsea applications [50], [51].

A summary of loading conditions which have been described via either analytical/theoretical equation (T) or numerical (N) methods is provided in Table 2.1.

Table 2.1. Loading Conditions Covered by Existing Models

	Axial T/C (AT, AC)	Torsion (M)	Pressure (P)	Shear (R)	Bending (B)	Impact & Lateral (L)	Fatigue (F)	Combined Loading
Room Temp.	T(AC)		T, N		T, N	N	T,N	T,N(P/AT) N(P/L) N(P/B)
Elevated Temp.	N(AT)	T	T,N	T	N			N(P/AT)

Major developments in modeling for bending, pressure, and combined loading conditions are described in sections 2.2.1, 2.2.2, and 2.2.3, respectively. Section 2.2.4 is a summary and interpretation of the state of existing work.

2.2.1 Bending

Bending behavior of RTP was investigated in 2015 by Bai et al. using the nonlinear ring theory originally developed by Kyriakides et al. This model investigated the effect of transverse deformation through the wall thickness and ovalization of the cross section. The results of the theoretical method for HDPE and a simplified reinforced layer were compared to FEA simulation results in ABAQUS with good agreement [52].

Wang, Yao, and Meng analyzed the bending response of HDPE and glass/PE RTP and TCP using a nonlinear solid element model. The aim of this work was to predict buckling, post-buckling, and collapse behavior considering the effects of initial ovality, fiber volume fraction, diameter-to-thickness ratio, and ply angle. The Riks algorithm is used to capture the instability of the problem as the tangent stiffness becomes close to null. Anisotropy of the material properties is captured using a separate procedure in UMAT which is called by the main process in ABAQUS [24].

Hastie et al. (2021) investigated the response of TCP under bending and thermal loads using a finite element model. The effect of elevated temperatures on the PEEK matrix are considered, and the maximum stress and Tsai-Hill failure criteria are compared. [26]

2.2.2 Internal Pressure

Xia et. al (2021) investigated the response of TCP under internal pressure using an analytical model and FEA (both 3D). The analytical model was based on the anisotropy elastic theory and accounted for nonuniform stress and strain distribution through the wall thickness. The maximum burst pressure was predicted using the 3D Tsai-Wu criterion. The effects of winding angle and number of plies on the burst pressure were studied. It was found that the analytical model and FEA simulation had good agreement, and it was found that burst pressure increases asymptotically as the number of plies increases, and that the optimal fiber winding angle varied as the thickness of the laminate increases. [53]

Shi, Xia, Wang, Bao, Li, and Fu developed a partially-plastic theoretical model to analyze TCPs subjected to internal pressures. An FEA model is used to validate the study, and both models show good agreement in predicting the final burst pressure of the pipe. Burst pressure experiments were performed to test the accuracy of the models. The theoretical model uses the same system as the MATLAB currently in use, and the FEA is performed using ABAQUS. Failure criteria are compared, and Tsai-Wu and Tsai-Hill methods are identified as the best, most conservative choices. [54]

2.2.3 Combined Loading

Hastie et al. developed a 3D finite element model to analyze the stress state in a TCP section under combined pressure, axial tension, and thermal gradient. Using the stresses obtained at each point through the wall thickness, a failure coefficient is evaluated for these points using and comparing the maximum stress and Tsai-Hill failure criteria. The effects of increasing thermal gradients considering temperature-dependent material properties are investigated as well as the influence of varying thickness [55].

Qiao, Zhang, Bai, et. al. developed an analytical model based on Knapp's optical cable model to study RTP under combined tension and internal pressure. The model accounts for nonlinearity, and implies that it accounts for the anisotropy of the reinforcement layer. The method uniquely accounts for radial contraction in the cross section in its analysis. The final analytical model is compared to an ABAQUS FEA model, showing good agreement within 10% elongation. [56]

Bai, Wang, Cheng, Yu, Badaruddin, and Ashri studied the collapse pressure and buckling of a multi-layered RTP using a mathematical model based on the isotropic flexural stiffness in the hoop direction. Simplified the model by considering only isotropic behavior and no relative slip between layers. The model is certified by a continuum shell Finite Element Analysis method and some experimental tests with good agreement. [50]

A study by Bai, Xu, Cheng, Wang, and Ruan developed a two-dimensional theoretical model to analyze failures of RTP under external pressure and tension. In this model, load-displacement responses are calculated using nonlinear ring theory. It is assumed that the loading and boundary conditions are uniform along the axis, allowing the pipe to be modeled as a ring. It is assumed that, given the winding angle of the fibers, only the PE-matrix contributes to axial strength and the composite can be modeled as a homogeneous material. The limit state function factors in a change in pipe radius and wall thickness that result from external pressure by incrementally updating those parameters at each time step. The Newton-Raphson method is used to solve the equation, and the results are compared to an elastic-plastic FE model with a short pipe length to better compare to the 2D theoretical model. A limit strain of 0.5 is used to parameterize the pressure and tension, and two scenarios are modelled, both using a constant tension with increasing pressure. With a 40kN of tension, it was found that failure was primarily due to buckling, but at 100kN of tension, material failure occurred before buckling. [51]

Wang, Lou, and Wang develop an RTP model studying the impact of random variable uncertainty introduced during the production process on the failure burst pressure of pipes under combined loading conditions. The pipes were modeled as thick-walled cylinders using the homogenization method. The Hashin-Yeh failure criterion was used to develop a progressive failure model in MATLAB. The model showed good agreement with experimental results. It was determined that the random variation of material parameters generated during production increased the probability of lower than average burst pressure. [57]

Wang et al. (2020) performed an investigation of the impact resistance of TCP in terms of the internal pressure capacity. A finite element model in ABAQUS was used to evaluate the capacity of the damaged pipe, and a theoretical model was proposed to calculate the impact energy from a rigid ball dropped in shallow water. The results of this work indicated that the post-impact pressure capacity was below the acceptable level. [58]

2.2.4 Conclusions

The research to date has covered bending, internal/external pressure, and axial loads as the primary loading conditions experienced by TCP and RTP, and several combinations of these loads have been modeled with good results. However, some key combinations of loading conditions such as internal pressure and flexure considering thermal strains have yet to be modeled with verification. Further, while some models have captured the combination of nonlinearity and anisotropy for individual loading mechanisms, such as axial loads, there remain loading conditions where the impact of this combination remains unmodeled. Finally, modeling of mechanical behavior following damage has been covered for the cases of burst capacity and post-buckling behavior, but further work is needed on this area, as delamination caused by impact damage can be fatal to composite materials in application. In the absence of specific knowledge of this effect, it must be approximated using expert opinion.

3 Research Objectives and Contributions

3.1 Problem Statement

Currently, there exists a modeling gap for the prediction of the performance of reinforced thermoplastic pipes (RTP) and thermoplastic composite pipes (TCP) over long periods of time exposed to a natural environment containing temperature fluctuations and mixtures of oil-based and water-based fluids. During exposure to these conditions, composite materials undergo some degree of degradation, but experimental data on these materials suggests a wide variety in responses to these conditions, which is to be expected given the anisotropy of the material and the large amount of variation in factors such as bond quality, fiber angle, fiber length, void fraction, and fillers.

Therefore, the goal of this work is to bridge some of the gaps in predicting the degradation and subsequent failure of these materials in a variety of environments with this level of uncertainty in mind.

3.2 Objectives

The broad aim of this research was to develop a reliability prediction model for the mechanical properties and performance of reinforced polymer pipeline materials with a focus on reinforced thermoplastic pipes (RTP) and thermoplastic composite pipes (TCP).

The following subtasks were included as a part of this process:

- Identify analytical models for the prediction of environmental degradation phenomena that are most common for RTP and TCP. The described mechanisms are:
  - Fluid uptake, including hydrocarbons, freshwater, and saltwater considering spatial and temporal variation of parameters which influence diffusion, such as temperature and material diffusivity parameters.

    - Thermal and hydrothermal degradation including softening of the polymer matrix in high temperatures.
- Build estimations, based on empirical data regarding the environment and component design, for material and environmental input parameters specific to the identified models.
- Develop the ability to predict changes to mechanical properties given the extent of fluid absorption, thermal degradation, and thermal softening, while taking into account uncertainty in the degree of degradation caused by each of these factors. This is achieved through comparisons to existing experimental data combined with knowledge of the physical processes to guide trends for the prediction of degradation rates in conditions where no data exists.
- Predict the likelihood of catastrophic laminate failure under the specified thermomechanical loading conditions for each time window.
- Verify predictions of mechanical property changes and failure likelihoods to available experimental data from both laboratory settings and field data.
- Build a curve of reliability with respect to time, based on design requirements and evolution of damage to the component.
- Integrate these modeling capabilities into the Pipeline System Integrity Management (PSIM) platform to allow for the prediction of real systems based on their locations and properties, and perform analyses to compare a variety of design options.

3.3 Research Contributions

This following contributions were made by this research:

- Development of a reliability prediction model with both thermomechanical loading and environmental degradation for TCP considering a variety of designs and environments

- Accounting for both epistemic (knowledge about exact material properties and variability in operating conditions over location and time) and aleatory (natural variability in environmental factors and material properties) uncertainty. These properties will be varied across time and space with reasonable ranges.
- Expansion of Pipeline System and Integrity Management (PSIM) capabilities to include thermoplastic composite pipes and offshore environments

4 Modeling Structure and Scope

4.1 Introduction

The broad aim of this research is to develop a comprehensive modeling framework for potential failures of TCP. Prior chapters in this thesis have described failure mechanisms for which good information is available to constrain models (e.g., single mechanical loading mechanisms and temperature-dependent material properties) and other failure mechanisms for which existing knowledge is relatively limited (e.g., complex loading combinations and growth of damaged regions by environmental degradation or cracking).

What makes this research unique is that it captures all viable mechanisms described in the scope (Section 1.3) and the correlations between them. These mechanisms are: fluid absorption resulting from exposure to water and oil on the inside and/or outside of the pipe, as well as the degradation of the pipe's mechanical properties that results from this absorption; thermal softening at elevated temperatures; thermal degradation resulting from prolonged exposure to high temperatures; and progressive failure resulting from thermomechanical loading.

For each component of the model, there is a quantified degree of epistemic uncertainty. This uncertainty is low when there exists specific data/knowledge. Where prior research is unavailable or very limited, substantial epistemic uncertainty exists due to modeling uncertainty and parametric uncertainty.

The models developed here account for both cases, allowing the tool to provide a comprehensive picture of TCP failure risk. The tool is adaptable as knowledge increases over time – such efforts will reduce modeling uncertainty and inevitably improve model performance.

This section describes how this model is being constructed and gives a brief introduction to its individual components, each of which will be explained in more detail in different sections. A summary of the proposed model is shown in Figure 4.1.

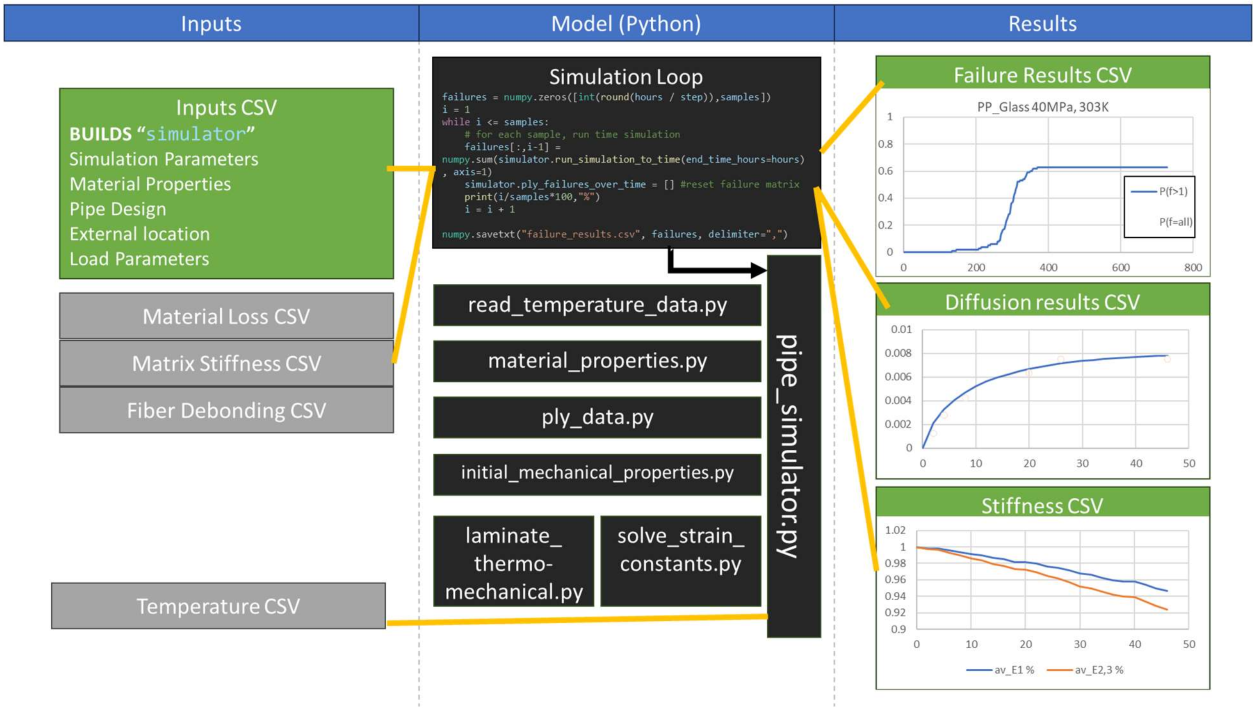

```
failures = numpy.zeros([int(round(hours / step)),samples])
i = 1
while i <= samples:
    # for each sample, run time simulation
    failures[:,i-1] =
numpy.sum(simulator.run_simulation_to_time(end_time_hours=hours)
, axis=1)
    simulator.ply_failures_over_time = [] #reset failure matrix
    print(i/samples*100,"%")
    i = i + 1

numpy.savetxt("failure_results.csv", failures, delimiter=",")
```

Figure 4.1. Model Structure showing how python components interact with external data (CSV) files

The basic components of this model are the python code, shown in black boxes in the figure; a simulation loop which reads the inputs, calls the python simulation, and writes the outputs; and input and output CSV files. More information on each of these components will be described in subsequent sections.

4.2 Model Parameters

Table 4.1 introduces the input parameters for the model that are unique to each simulation. These inputs are brought in with a CSV format to be read by the python code.

Table 4.1. Input parameters

Parameter Name	*Unit*	*Note*
Number of samples		Number of random samples to simulate
Simulation time	hours	Total number of hours to simulate
Time step (hours)	hours	Length of each simulation step
Start timestamp	Date	Year/Month/Day/Hour
Region		Name of the nearest major city
Pipe segment length	meters	
Internal Temperature mean	Kelvin	
Internal Temperature standard deviation		Between 0.0 and 1.0
External Temperature (if constant)	Kelvin	Set to -1 to use weather conditions for external temp.
Diffusion method		Set as “1” or “2”
Polymer D_0 (water)	$mm^2/hour$	
Polymer D_0 (oil)	$mm^2/hour$	
Composite D_0 (water)	$mm^2/hour$	Can leave blank if using method 2
Composite D_0 (oil)	$mm^2/hour$	Can leave blank if using method 2
Diffusion activation energy	J/mol	
Polymer water saturation at 80°C		Between 0.0 and 1.0
Composite water saturation at 80°C		Leave blank if using method 2
Polymer oil saturation at 80°C		Between 0.0 and 1.0
Composite oil saturation at 80°C		Leave blank if using method 2
Void Fraction		Between 0 and 1
Pipe depth	meters	Depth of pipe below the surface
Outer cover thickness	mm	Set to 0 if there is no cover
Inner liner thickness	mm	Set to 0 if there is no liner
Reinforcement ply thickness	mm	
Number of reinforcement plies		Integer greater than 0
Innermost radius	mm	Inner radius of the pipe
External water concentration		Between 0.0 (dry) and 1.0 (all water)
Internal water concentration		Between 0.0 (dry) and 1.0 (all water)
External oil concentration		Between 0.0 (dry) and 1.0 (all oil)
Internal oil concentration		Between 0.0 (dry) and 1.0 (all oil)
Matrix material		Must be “PA”, “PP”, or “PE”
Fiber material		Must be “Carbon” or “Glass”
Fiber volume fraction		Between 0.0 and 1.0
Fiber angles	degrees	Array of fiber angles for each ply. Liner and cover use 0
Internal pressure	MPa	
Axial Force	MPa	
Axial Moment	N*m	
Failure Criteria		“TSAI_WU”, “TSAI_HILL” or “MAX_STRESS”

The “diffusion method” shown in the table is an option used based upon whether or not fluid absorption data exists for this laminate. If no data exists, method 2 is used, and the model will estimate the impact of the fibers and void fraction on the absorption relative to that of the matrix polymer. More details on this method are provided in Section 5.

In addition to the changing inputs from Table 4.1, four additional sets of information are brought into the model from un-editable CSV files. These are the temperature data file for each region, and three conditional probability tables. The conditional probability tables will be described in Section 6.

4.2.1 Material Parameters

As this work investigates processes of diffusion, thermal degradation, and thermomechanical loading, the material parameters in the following list are considered for an individual ply within the composite laminate. Due to the anisotropy of a composite ply, many of these parameters must be defined separately for the longitudinal (1), transverse (2) and through-thickness (3) directions, visualized in Figure 4.2.

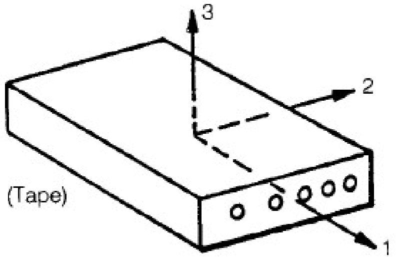

Figure 4.2. Axes of a composite ply

1. *Stiffness in the 1, 2 and 3 directions:* E_1, E_2, E_3

   From the constituent matrix (E_m) and fiber (E_f) stiffness, described in Section 7

2. Tensile strength in the 1, 2 and 3 directions: X_T, Y_T, Z_T

   From the constituent matrix (F_{Tm}) and fiber (F_{Tf}) tensile strength, described in Section 7

3. Compressive strength in the 1, 2 and 3 directions: X_C, Y_C, Z_C

   From the constituent matrix (F_{Cm}) and fiber (F_{Cf}) compressive strength, described in Section 7

4. Poisson ratio in the 12, 13, and 23 directions: $\nu_{12}, \nu_{13}, \nu_{23}$

   From the constituent matrix (ν_m) and fiber (ν_f) Poisson ratio, described in Section 7

5. Coefficient of thermal expansion in the longitudinal (1) and transverse/through thickness (2/3) directions: α_1, α_2

   From the matrix ($\alpha_{1m} = \alpha_{2m}$) and fiber ($\alpha_{1f}$, α_{2f}) coefficients, described in Section 7

6. Thermal conductivity: k

   From the constituent matrix (k_m) and fiber (k_f) conductivity, described in Section 7

7. Shear stiffness in the 12, 13, and 23 directions: G_{12}, G_{12}, G_{23}

   Matrix and fiber shear moduli are calculated from their respective Young's moduli and Poisson ratio using Eq. 4.1

$$G = \frac{E}{2(1+\nu)}$$

8. Shear strength in the 12, 13, and 23 directions: X_{12}, X_{13}, X_{23}

   From the constituent matrix and fiber shear strengths, described in Section 7

9. Inner and outer convective heat transfer coefficients: h_0, h_a

   Estimated to be about $50W/m^2{}^\circ C$ and $20W/m^2{}^\circ C$, respectively [59]

10. Glass transition and melting temperatures: T_g, T_m

    Uses the matrix T_g and T_m

The constituent properties are stored as either ranges or means and standard deviations in a library, sorted by the matrix or fiber material. All properties are assumed to be lognormally distributed except for the coefficient of thermal expansion, which is normally distributed, and the glass transition and melting temperatures, which are single data points. As of the completion of this work, data for high density polyethylene (HDPE), polypropylene (PP), and nylon (PA) matrices, as well as carbon and glass fibers have been added. The ranges used for the polymer materials are provided in Table 4.2, and fiber data is provided in Table 4.3. The data for this table comes from a textbook by Callister (2019) [11].

Table 4.2. Matrix Property Data

	E_m (GPa)	F_{Tm} (MPa)	F_{Cm} (MPa)	ν_m	α_m (°C^{-1})	k_m (W/mK)	$X_{shear.m}$ (MPa)	T_g (K)	T_m (K)
PE	0.75-1.8	18-40	80-90	0.3-0.51	μ=152E-6 σ=0.1E-6	0.46-0.5	10-21	173.2	403.2
PP	1.14-1.55	31-41.4	34.1-45.5	μ=0.4 σ=0.02	μ=163E-6 σ=0.1E-6	0.119-0.121	10-21	248.2	443.2
PA	2.5-3.8	65-85	85-120	μ=0.39 σ=0.02	μ=144E-6 σ=0.1E-6	0.239-0.241	10-21	322.2	523.2

Table 4.3. Fiber Property Data

	E_f (GPa)	F_{Tf} (MPa)	F_{Cf} (MPa)	ν_f	α_{1f} (°C^{-1})	α_{2f} (°C^{-1})	k_f (W/mK)	$X_{shear.f}$ (MPa)
Carbon	228-550	1500-5700	990-3762	μ=0.4 σ=0.2	μ=-0.6E-6 σ=0.01E-6	μ=10E-6 σ=0.01E-6	μ=11 σ=0.02	μ=100 σ=0.02
Glass	68.5-87	1834-4900	1210-3254	μ=0.22 σ=0.02	μ=4.9E-6 σ=0.01E-6	μ=5.1E-6 σ=0.01E-6	μ=1.3 σ=0.05	μ=85 σ=0.02

4.2.2 Environmental factors

Environmental degradation processes considered by this work are water and oil absorption and thermal softening and degradation. As a result, information on the temperature on the inside and outside of the pipe, as well as the concentration of oil-based and water-based fluids is needed.

Most environmental inputs are taken directly from the inputs CSV, shown in Table 4.1. Specifically, the internal temperature, external temperature (if controlled), and fluid concentration parameters are taken from this file.

In the case where the external temperature is not constant – in other words, it varies with weather to some extent – information on the local weather is used and, combined with the depth of the pipe in the ground, the external temperature is estimated by the model.

First, temperature data is brought in based on the region specified using historical records of hourly temperature [60]. This document used contains records for 50 cities within the US and Canada, and 6 cities in Israel from October 1st 2012 through Nov 29th 2017. This data is aggregated for use in predictions by taking the data for the same month, day and hour timestamp for each year, and determining the average and standard deviation for that time window. Additionally, leap year times are removed because they cannot be applied to every future year.

If the pipe is located at the surface or in open air, the external temperature is simply sampled from this average and standard deviation for each time step. In most cases, however, the pipe is buried and is not subject to the full degree of temperature fluctuations of the outside air. The depth input from Table 4.1 is then used to estimate the local external temperature, using Eq. 4.2, where T_d is the temperature at the current depth *(d)*, T_{soil} is a constant soil temperature sufficiently deep below the surface, equal to 293.15K, and T_{air} is the sampled temperature from weather data.

$$\begin{gathered}
T_d = T_{air} \quad d < 0.1m \\
T_d = 0.8 * T_{air} + 0.2 * T_{soil} \quad d < 0.2m \\
T_d = 0.67 * T_{air} + 0.33 * T_{soil} \quad d < 0.3m \\
T_d = 0.33 * T_{air} + 0.67 * T_{soil} \quad d < 0.4m \\
T_d = 0.2 * T_{air} + 0.8 * T_{soil} \quad d < 0.5m \\
T_d = T_{soil} \quad d \geq 0.5m
\end{gathered} \tag{4.2}$$

Using the average hourly temperatures in the Los Angeles region, the external temperature of a pipe buried at surface level and 0.1, 0.2, 0.3, and 0.4 meters below the surface are shown in Figure 4.3.

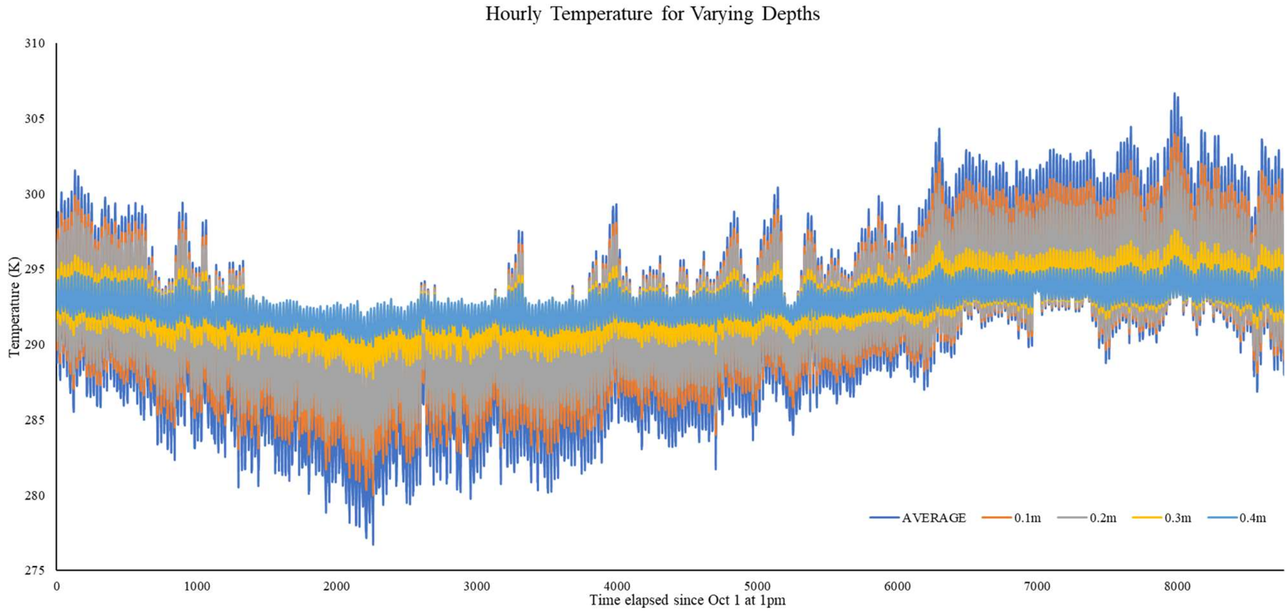

Figure 4.3. Hourly temperature at surface level (AVERAGE line) and at 0.1, 0.2, 0.3, and 0.4

The internal temperature is sampled from a normal distribution using the parameters provided in the inputs table. If the external temperature is set as controlled in the inputs table, it is modelled with the same standard deviation as the internal temperature.

The internal and external fluid concentrations are not treated as uncertain parameters, and are instead taken as the values provided in the inputs table.

4.2.3 Mechanical Loads

Mechanical loads used in this model are internal pressure from high pressure pipe contents, axial tension or compression, and axial torsion. These inputs are all brought in through the inputs table (Table 4.1).

4.3 Overview of Model Structure

This section briefly introduces the structure and components of the degradation and failure model developed for this research. Further detail on each of these components can be found in later sections of this thesis. This model was developed in python using Microsoft Visual Studio using a Jupyter notebook to run the simulations.

4.3.1 Structure

The simulation consists of two nested loops: Monte Carlo sampling of uncertain parameters (outer loop), and time simulation for single sample (inner loop).

The outer loop retrieves data from the inputs, and consists of the following functions:

1. Sampling of the initial (undamaged) matrix and fiber properties.
2. Calculation of initial (undamaged) composite properties. These are stored as a data class for each ply in the laminate. If the pipe has a liner or cover, the matrix properties are used instead of composite properties.
3. Iteration over each time step and calling of the time (inner) loop. This loop will end early if all plies fail.
4. Writing failure, absorption, and stiffness degradation data stored in a matrix of $N_{samples}$ by N_{times}, to be output by the simulation. If the time loop ended early due to failure of all plies, the rest of the matrix will be filled with the data obtained on the last completed time step

The inner loop retrieves its inputs from the outer loop's sampled data, and consists of the following functions:

1. Sampling of temperature data for the given time step

2. Calculation of diffusivities for use in the fluid absorption function based on the sampled temperatures
3. Estimation of water and oil absorption resulting from internal and external fluid exposure
4. Degradation of matrix stiffness and strength and debonding of fibers resulting from moisture absorption and thermal degradation
5. Recalculation of composite properties given the degradation
6. Calculation of stress at each ply using a thermomechanical model
7. Evaluation of ply stress against a failure criteria (defined in the inputs)
8. For failed plies, application of the failed status, which will sharply reduce those plies' mechanical stiffnesses in the next time step
9. Reporting of outputs: average stiffness of the laminate throughout the time step, average absorbed water and oil, and the number of failed plies during the time step

An overview of this structure is shown in Figure 4.4. Different types of model functions are highlighted in different colors (described in the figure caption).

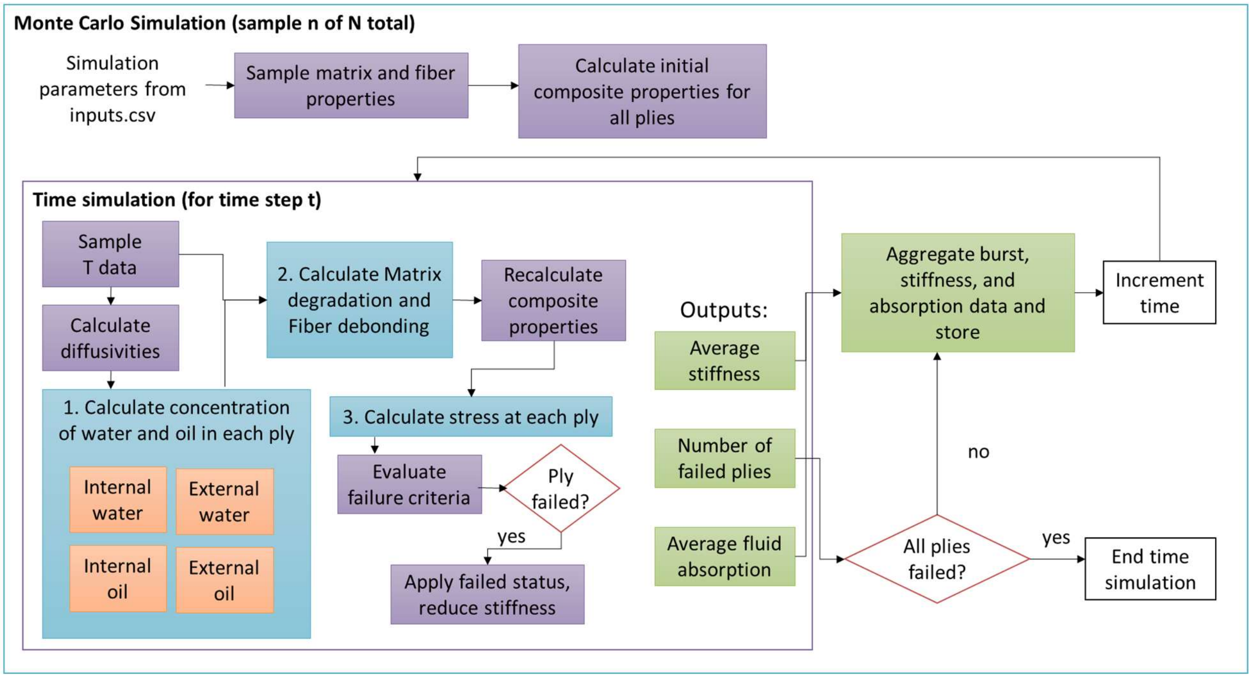

Figure 4.4. Interaction between model functions. Blue functions represent physical processes, purple functions represent calculation of properties and other smaller functions, and green boxes represent output values

The initial properties, calculated outside of the time simulation, are used as the properties for the thermomechanical stress calculations at the first time step (t = 0), as there has not been enough time for the degradation from the time-dependent absorption and degradation processes to occur. The sampled constituent properties also serve as the initial, undamaged values of these properties for the full-time simulation for that sample.

Within the time simulation, temperature is allowed to vary at each time step, leading to differences in thermal degradation and water and oil diffusivities as time progresses.

Water and oil absorption is run through a single function that estimates the additional water or oil absorbed in that time step, which is added to the already absorbed amount of fluid. This method, described further in Section 5, allows for variation in diffusivity with changing temperatures to be factored into the diffusion process.

Degradation of the material properties is carried out with a degradation process which uses the individual ply's temperature (see section 4.3.2) and the amount of absorbed water and oil to predict rates of matrix property loss and fiber debonding. This rate is multiplied by the length of a time step to determine the amount of additional degradation obtained during this time step, which is added to the existing amount of degradation built up in previous times. Using the accumulated degradation parameters, the composite properties are recalculated with the reduced matrix properties and fiber bonding. More information on how the degradation rates are calculated is available in Section 6, and the method used for applying these rates to the material properties is described in Section 7.

Finally, an axisymmetric thermomechanical model is used to determine the stress state at each ply given the current state of the ply stiffness and strength, as well as the input temperatures and loads. The stress state is then compared against the chosen failure criteria in the inputs to determine which, if any, plies failed in this time step.

4.3.2 Calculation of ply-specific temperature

In many of these physical processes, the temperature of an individual ply needs to be calculated. For an external temperature T_∞ and internal temperature T_0, the temperature at a given radius r between the inner radius r_0 and outer radius r_a can be calculated as shown in Eq. 4.3.

$$T = A + B \ln r \tag{4.3}$$

Where A and B are given in Eq. 8.2. The equation for A has been modified from the solution described by Bakaiyan et al. [59]. This modification was made due to issues with the original solution’s ability to model the temperature of a laminate with the same internal and external temperature.

$$A = T_0 - B \ln r_0 \qquad B = \frac{T_\infty - T_0}{k\left(\frac{1}{r_o h_a} - \frac{1}{r_0 h_0}\right) + \ln(r_a/r_0)} \tag{4.4}$$

4.4 Model Outputs

This section describes the failure and degradation parameters used by the model, and the method used to aggregate laminate data for the outputs. All outputs are printed as CSV files with the time elapsed attached as the first column.

4.4.1 Failure

This model uses burst as the failure metric, defining burst as occurring once all plies have failed. Individual ply failures are determined within a particular time step using the failure criteria given the stress state on the ply, and the number of plies failed are counted at each time step. If the number of failed plies reaches the total number of plies, the model counts this sample as failed, and it will remain in this state for the rest of the time simulation. The number of samples that record burst failure at each time step are added together at the end of the simulation and divided by the total number of samples to determine the probability of failure at each time step.

4.4.2 Aggregated Absorption and Stiffness Data

In addition to the failure metric, the average amount of absorbed water and oil in the laminate as well as the average stiffness in the longitudinal, transverse, and shear (23) directions are recorded for each time step and sample. These laminate values are calculated by taking a weighted average of each ply’s fluid concentration and stiffness, weighted to the ply’s thickness.

These outputs are printed in two forms: raw data recorded for each sample and time, and average and standard deviations across all samples. In the case of the stiffness outputs, the average and standard deviation outputs are reported as reduced values, between 0 and 100%, of the stiffness and standard deviation of the stiffness of the laminate in its initial condition.

4.5 Summary

This section introduces the basic structure and scope of the model developed for this research. This research has focused on degradation resulting from water and oil absorption and thermal degradation, and the resulting likelihood of ply and laminate failure under axisymmetric stresses considering that degradation. The input material properties, environmental factors, and mechanical stresses used by this model were introduced, as well as the failure and degradation metrics that are tracked and output by the model.

5 Fluid Absorption

5.1 Introduction

The aim of this section of the thesis is to present the model component that captures the diffusion of either the transport fluid or external fluids (mainly water or seawater) through the pipe wall. If this diffusion occurs only within the inner liner or outer cover, the effect on the pipes' mechanical properties is negligible, but this process can be damaging if either one of these protective layers is breached.

5.2 Fickian Diffusion Process

For the analysis of a pipe, it is assumed that fluid may diffuse only through the walls, and that the diffusion does not change in the radial direction or along the length of the pipe. This enables the problem to be reduced to a single (radial) dimension Fickian problem. Fick's differential equation for diffusion (also known as Fick's Law) is given by Eq. 5.1.

$$\frac{\partial c}{\partial t} = D\frac{\partial^2 c}{\partial x^2} \tag{5.1}$$

where c is concentration, x indicates the direction of fluid motion in diffusion, and D is the time-independent diffusivity.

The rate of fluid uptake (absorption) is determined in the present work by the diffusivity of the fluid in the polymer, designated as D_s. In principle, the rate of polymer dissolution into the fluid, designated as D_p, may also influence the problem, but this aspect is neglected in the present work, because preliminary studies suggest it is a minor effect, and information on D_p in the literature is lacking. Both D_s and D_p are temperature-dependent and can be calculated from experimentally determined parameters as shown in Eq. 5.2.

$$D(T) = D_0 \exp\left(-\frac{E_D}{kT}\right) \tag{5.2}$$

where $D(T)$ is temperature-dependent diffusion as described by a Fickian process (i.e., as given in Eq. 5.1), D_0 and E_D are diffusion parameters specific to the material and fluid combination, k is the Boltzmann constant ($1.38 \times 10^{-2}\ J/K$), and T is temperature in Kelvin.

Evaluation of the material constants in Eq. 5.2 (D_0 and E_D) requires measurements of the diffusivity parameter for at least two different temperatures. For two similar systems (e.g., systems having the same matrix material and the same diffusing fluid), I assume that values of D_0 and E_D derived in one time and place (i.e., in a particular study) can be applied generally (they do not require a separate measurement).

Next I turn to the problem of fibers contained within the pipe matrix. Eq. 5.2 is retained for this problem, but D_s is changed. For diffusion through a matrix with fibers, two methods have been considered:

1. **Empirical Modification of D_s:** This method assumes diffusion can be modeled through a single Fickian process (Eq. 5.1) if the differences between the diffusion parameters D_0 and E_D for a neat polymer (i.e., a polymer without fibers) and composite are known.
2. **Modeling of two simultaneous diffusion processes:** This methodology modifies Fick's model by assuming the fluid will diffuse in two separate processes. A generic form of this is shown in Eq. 5.3, and variations of this methodology are described in Section 1.5.3.1. This method has the potential to provide more accuracy than Method 1 but requires more information to determine both diffusivity values.

$$\frac{\partial c_1}{\partial t} + \frac{\partial c_2}{\partial t} = D_1 \frac{\partial^2 c_1}{\partial x^2} + D_2 \frac{\partial^2 c_2}{\partial x^2} \tag{5.3}$$

The solution of the differential equation in Eq. (5.3) introduces a parameter, c_∞, that represents the saturation concentration (concentration of the diffusing material) at infinite time.

Depending on the availability of data, either method may be used to account for the influence of fibers on the diffusion. Method 1 is generally more accurate but requires more empirical parameters to be used in the model to observe how c_∞ and D change when fibers are added. Method 2 requires less empirical data at the expense of generally overestimating the fluid uptake. If an estimate is available for gaps in the material, Eq. 5.4 is used for Method 2.

$$C_{total}(t) = \left(1 - V_f - V_g\right) * C_{matrix}(t) + V_f * C_{fiber}(t) + V_g * C_{gap}(t) \tag{5.4}$$

5.2.1 *Solution to Fick's Law for Time-invariant Diffusivity*

A solution to the Fickian diffusion problem presented in Eq. 5.1 was developed by Shen and Springer (1976) [61]. In this solution, shown in Eq. 5.5, *c(t)* is the concentration of the diffusing fluid present in the local region with thickness h of the pipe at an arbitrary time *t*.

$$c(t) = c_{source} * c_{\infty,\mathrm{T}} * \left(1 - e^{-7.3*\left(D*\frac{t}{h^2}\right)^{0.75}}\right) \tag{5.5}$$

where $c_{\infty,\mathrm{T}}$ is the saturation concentration (concentration at infinite time) for the current temperature, T, and c_{source} is the concentration of fluid in the adjacent layer available for diffusion. If the ply lies at the pipe's surface, c_{source} is the concentration of the diffusing fluid either inside of the pipe or in the outside environment; otherwise, this is the adjacent ply.

The saturation concentration at any given temperature, $c_{\infty,\mathrm{T}}$, is estimated from a single data point at roughly 80 °C (353K) using a sigmoidal function, shown in Eq. 5.6.

$$c_{\infty,\mathrm{T}} = 0.25c_{\infty,353} + \frac{c_{\infty,80} - 0.25c_{\infty,353}}{1 + e^{-0.15(T-335)}} \tag{5.6}$$

This method of estimating $c_{\infty,\mathrm{T}}$ assumes the minimum saturation concentration is 25% of that at 80°C, and that the mid-point of the change occurs at 335K. As will be seen later, this assumption works for some data sets, but is not well suited to others. Further work on this solution is necessary to improve its accuracy.

5.2.2 *Solution for Time-variable Diffusivity*

The solution in Eq. 5.5 is for the case of invariant diffusivity, *D*. As shown in Eq. 5.2, diffusivity varies with temperature, which in turn varies with time and thickness (diffusion depth) within the pipe section. In order to account for variations in diffusivity (*D)* over time and space, a modification of Eq. 5.5 is presented in Eq. 5.7. In this iterative equation, the concentration of the diffusing fluid at any time $c_j(t_{i+1})$ is computed from the concentration at the previous time $c_j(t_i)$ and the change as

$$c_j(t_{i+1}) = c_j(t_i) + c_{source,j} * c_{\infty,\mathrm{T,j}} * \left(-e^{-7.3*\left(D(t_{i+1})*\frac{t_{i+1}}{h^2}\right)^{0.75}} + e^{-7.3*\left(D(t_{i+1})*\frac{t_i}{h^2}\right)^{0.75}}\right) \quad (5.7)$$

where the term in brackets on the right side of Eq. 5.7 represents the change in concentration between time steps. The saturation concentration, $c_{\infty,\mathrm{T,j}}$, is also able to vary across plies to allow for differences in temperature and material. Similarly, the source concentration, $c_{source,j}$ will change with the border concentration of the j^{th} ply.

Four major diffusion processes can be modeled for each ply at each time step:

1. Oil from pipe interior
2. Oil from pipe exterior
3. Water from pipe interior
4. Water from pipe exterior

Whenever the fluid is coming from the inside of the pipe, the plies are iterated in a loop from the innermost to the outermost ply, and the concentration of oil/water in the pipe's interior is used as c_{ply-1} for the innermost ply. Conversely, in the cases for fluid on the pipe's exterior, the outermost ply is considered as the "first" ply and c_{ply-1} for that ply is the oil and/or water concentration in the external medium of the pipe.

Examples of the application of this approach for polypropylene/glass fiber composites in the form of sample bars suspended in water and oil using data from Spencer (2021) [49] are shown in Figures 5.1-5.3. The sample bars are manufactured as laminated composites with bonded plies. The samples were 5mm wide, 40mm long, and 0.25-0.5mm thick. During the experiment performed by Spencer (2021), the sample bars were fully suspended in the fluid medium for 25-50 days at a constant temperature. These results allow for investigation of the relative merits of Methods 1 and 2 using a dataset of diffusion through the composite of water at 50 °C and 80 °C, as well as oil at 25 °C. The empirical increase of D was 5%, and c_∞ increased by 93% for the composite (Method 1), while in the case of oil, D decreased by 77%, and c_∞ decreased by 1200% for the composite. Method 2 was investigated by using the diffusivity parameters of the neat polypropylene in water and oil, respectively, using the parameters in Table 5.1 as estimates for the matrix, fiber, and void diffusion coefficients.

Table 5.1. Diffusion parameters used for laminate components (matrix, fibers, and voids)

	VF	*Diffusivity*	*Saturation %*
Matrix (water)	44%	1.24E-7 mm^2/s	0.47%
Matrix (oil)		1.12E-7 mm^2/s	26%
Fiber	55%	1E-13 mm^2/s	0.01%
Voids	1%	0.02 mm^2/s	70%

Figure 5.1 shows results for water at 50 °C and indicates that c_∞ is overestimated somewhat by both methods while the rate of diffusion prior to saturation is better estimated by Method 1. Figure 5.2 shows results for water at 80 °C and indicates that c_∞ is well estimated by both methods while the rate of diffusion prior to saturation is again better estimated by Method 1. Figure 5.3 shows that c_∞ is accurately estimated by Method 1 but overestimated by Method 2 while the rate of diffusion prior to saturation is better estimated by Method 1 for oil at 25 °C.

Collectively, the results in Figures 5.1-5.3 suggest that Method 1 performs better than Method 2. However, some perspective on the application of these methods is needed here. Method 1 can be applied only when data on diffusion through a specific composite is available; in that case the applicable parameters can be fit to the data and then used in forward predictions. Such predictions are, not surprisingly, fairly accurate. Method 2 is more fundamental, modeling individual material components in the composite, but without the benefit of data on composite performance. As a result, while Method 2 may perform less well when compared to an experimental data set, it is also better suited to forward applications in which component properties are available but composite properties are not.

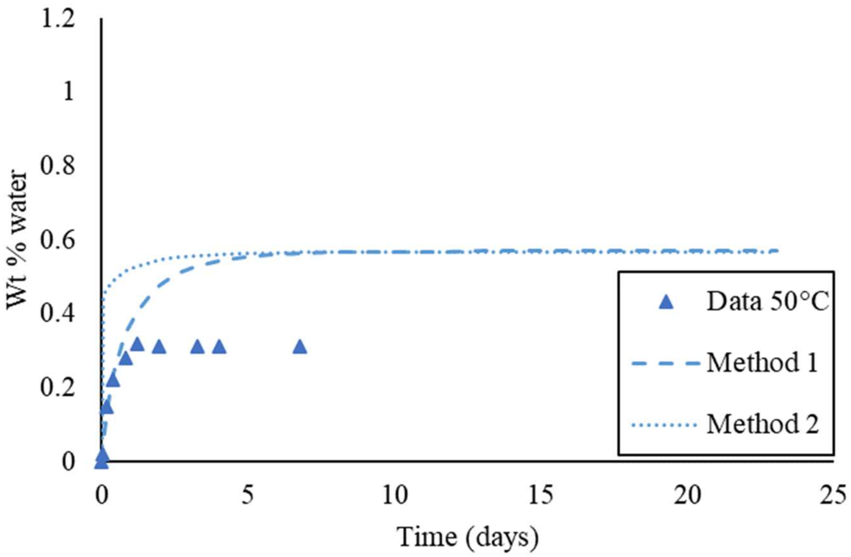

Figure 5.1. Comparison of methods 1 and 2 for PP-G in water at 50°C

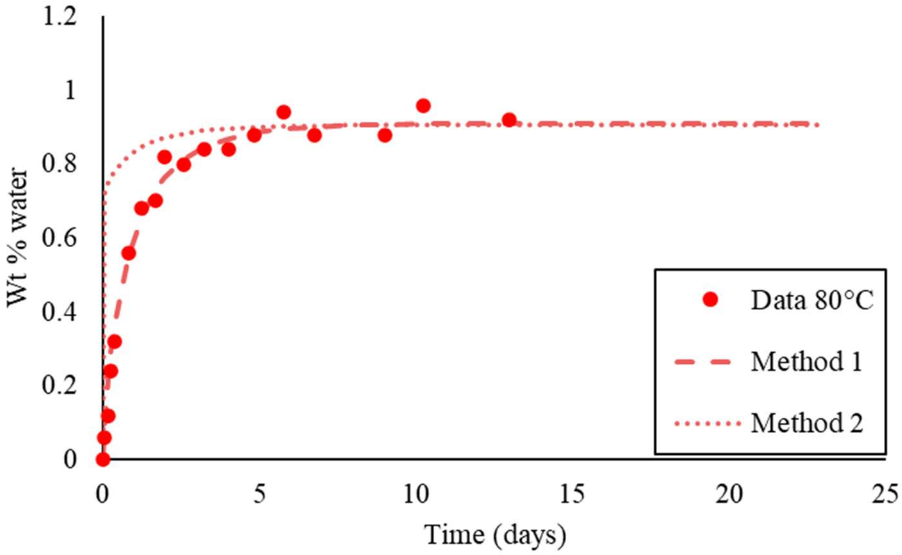

Figure 5.2. Comparison of methods 1 and 2 for PP-G in water at 80°C

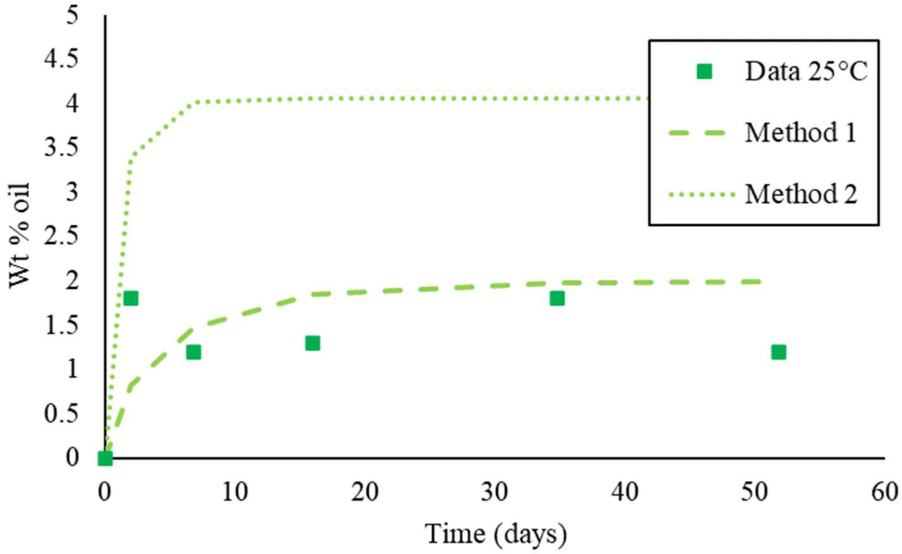

Figure 5.3. Comparison of methods 1 and 2 for PP-G in oil at 25°C

5.3 Diffusion Results

In this section, the method for obtaining diffusivity parameters from experimental data for use in testing the fluid absorption model and results of these tests are presented.

5.3.1 Determining Diffusivity Parameters from Experimental Data

To obtain parameters for the diffusion test cases, the reported water absorption values at each time were extracted into table form, and the times were converted to hours – the major time unit used in the present work. Experimental studies which presented results for multiple temperatures were preferred, such as the one shown in Figure 5.4, for the ability to determine the diffusivity parameters D_0 and E_D.

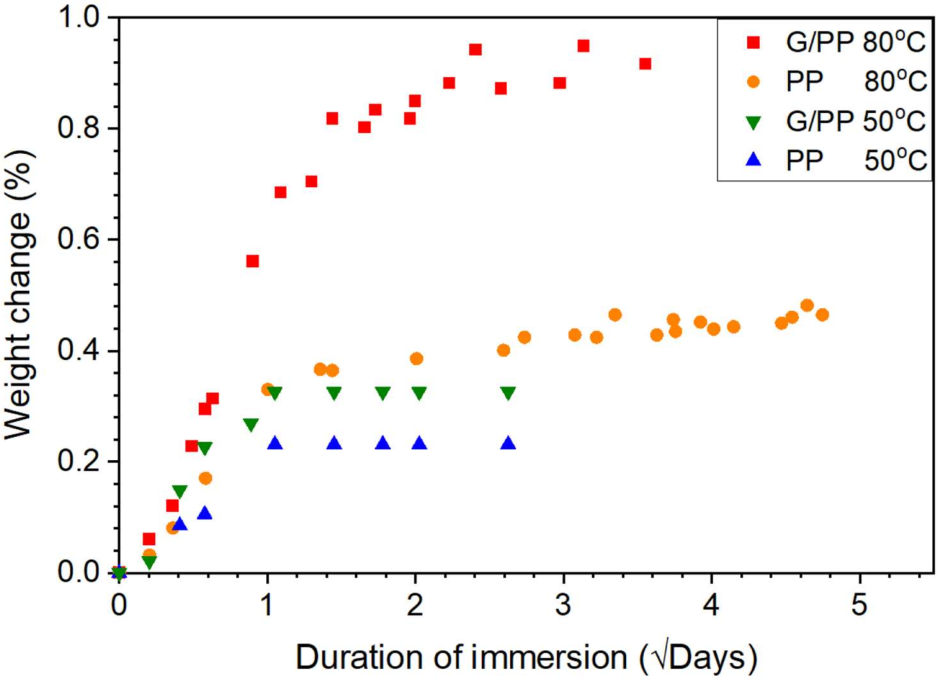

Figure 5.4. Water absorption results from Spencer (2021) for thin PP/G composite samples

The estimated diffusivity $D_{est,T}$ for a given temperature was calculated as the average of individual estimate $D_{est,T}(t)$ for the reported concentration $c(t)$ values over the early part of the absorption curve. The equation used for $D_{est,T}(t)$ is a rearrangement of the Fick's law solution presented in equation 4.3, and is shown in Eq. 5.8.

$$D_{est,T}(t) = \left(-\frac{\ln\left(1-c(t)/c_{\infty,est}\right)}{7.3}\right)^{1.5} \frac{h^2}{t} \tag{5.8}$$

Once $D_{est,T}$ has been calculated for each available temperature, the activation energy E_D is calculated using Eq. 5.9. If only two temperatures are available, the estimated activation energy $E_{D,est}$ is used for E_D. Otherwise, if three or more temperatures are available, all combinations are calculated and an average is used for E_D.

$$E_{D,est} = -\frac{k_b \ln\left(\frac{D_{est,T1}}{D_{est,T2}}\right)}{T_1^{-1} - T_2^{-1}} \quad \text{where } T_2 > T_1 \tag{5.9}$$

The corresponding initial diffusivity, $D_{0,est}$ is calculated from $E_{D,est}$ using equation 4.9. Similar to the activation energy case, if only two temperatures are present, $D_{0,est}$ is used for D_0, and an average is taken over three or more temperatures. In equation 5.10, T may be either T_1 or T_2 for the same result.

$$D_{0,est} = D_{est,T}\left(e^{-\frac{E_{D,est}}{k_b T}}\right)^{-1} \tag{5.10}$$

If only one temperature was presented in the data, $E_{D,est}$ could not be determined. For these cases, the value $E_{D,est}$ from a physically similar data set was used, and $D_{0,est}$ was calculated from this value.

5.3.2 Polyamide matrix

A range of model data was first compared against the range of experimental data from Arhant et al. [42], who submerged 2mm unidirectional cylindrical polyamide/carbon composite samples in water at 40 °C. The estimated diffusion parameters from the reported data are $D_0 = 27.17\, mm^2/hour$ and $E_D = 4.60 \times 10^{-20} J/mol$. The saturation concentration at 80 °C is estimated to be about 10%. Model results for this test case show generally good agreement with the data presented by Arhant et al., as seen in Figure 5.5.

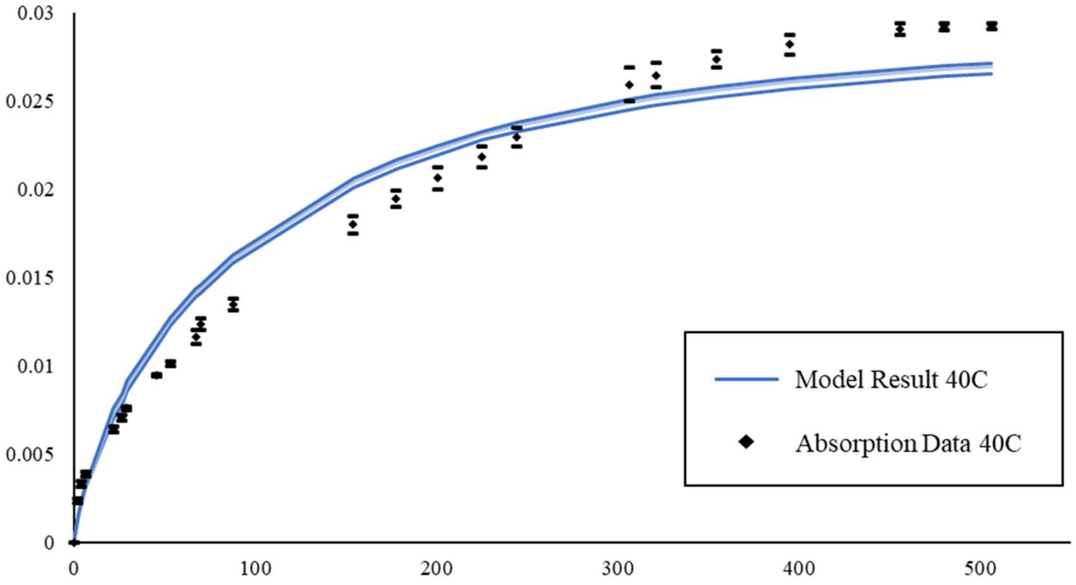

Figure 5.5. Comparison of model results for PA/C in seawater to experimental data from Arhant et al.

The next test case comes from Spencer (2021) [49], who presented the results of thin strips of polyamide composites suspended in water at a range of temperatures from 50-85 °C. The estimated diffusion parameters from the reported data are $D_0 = 3.40\, mm^2/hour$ and $E_D = 4.60 \times 10^{-20} J/mol$. The saturation concentration at 80 °C is estimated to be about 1.3%.

The results of this comparison are presented in Figure 5.6. The results match well with the experimental case, though some potential material loss is observed in the case at 85 °C which is not reported by the model.

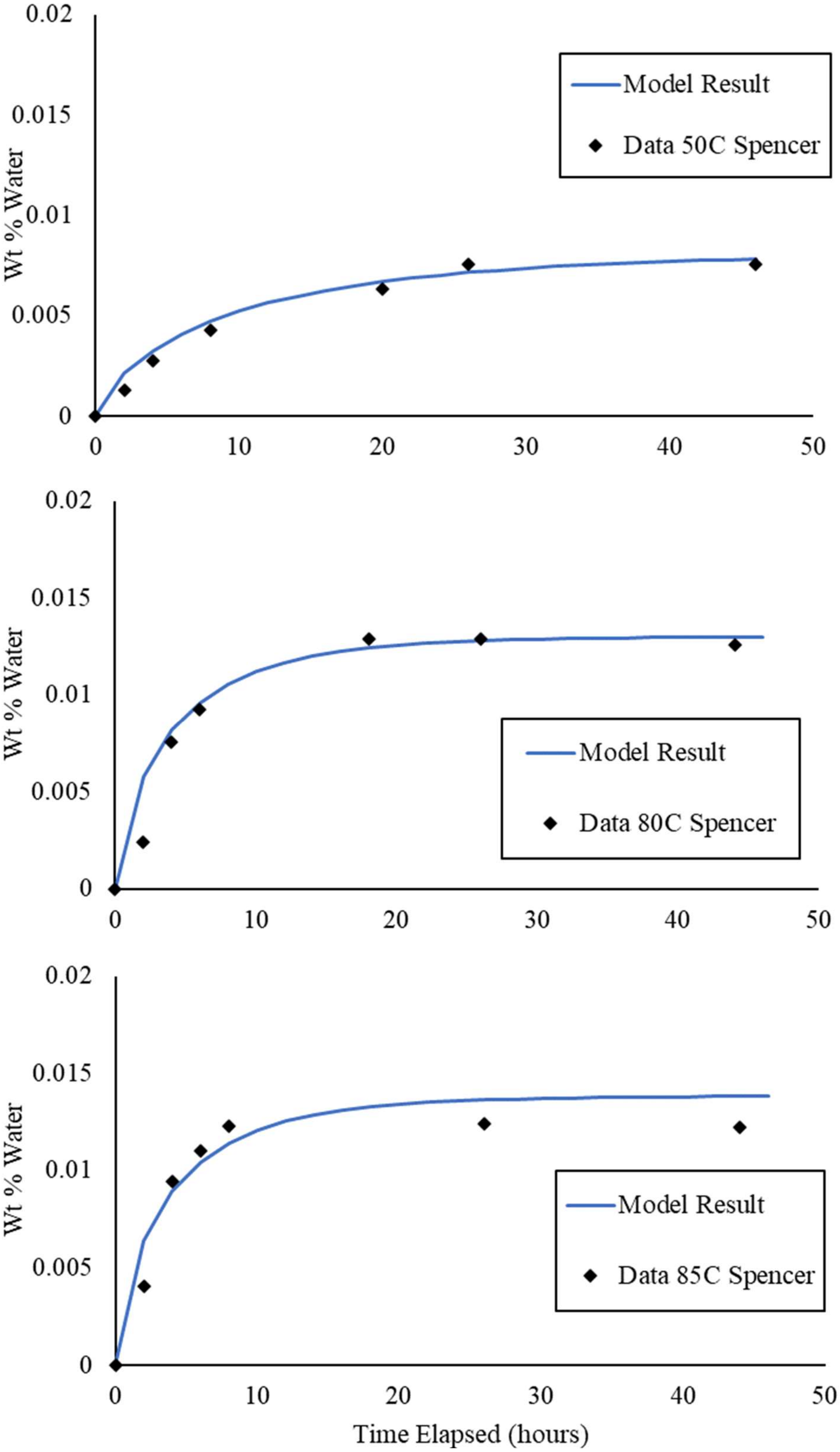

Figure 5.6. Comparison of absorption model results for a PA-based composite at 50-80 °C suspended in water to data from Spencer (2021)

Spencer (2021) also presented data on the absorption of a pentane/toluene oil mixture in PA composites at 100-130 °C. The estimated diffusion parameters from the reported data are $D_0 = 0.06\, mm^2/hour$ and $E_D = 2.72 \times 10^{-20} J/mol$. The saturation concentration at 80 °C is estimated to be about 8%.

The model results for this case, presented in Figure 5.7, show good agreement at early times, but the model becomes less accurate as mass loss begins to occur in the experimental samples.

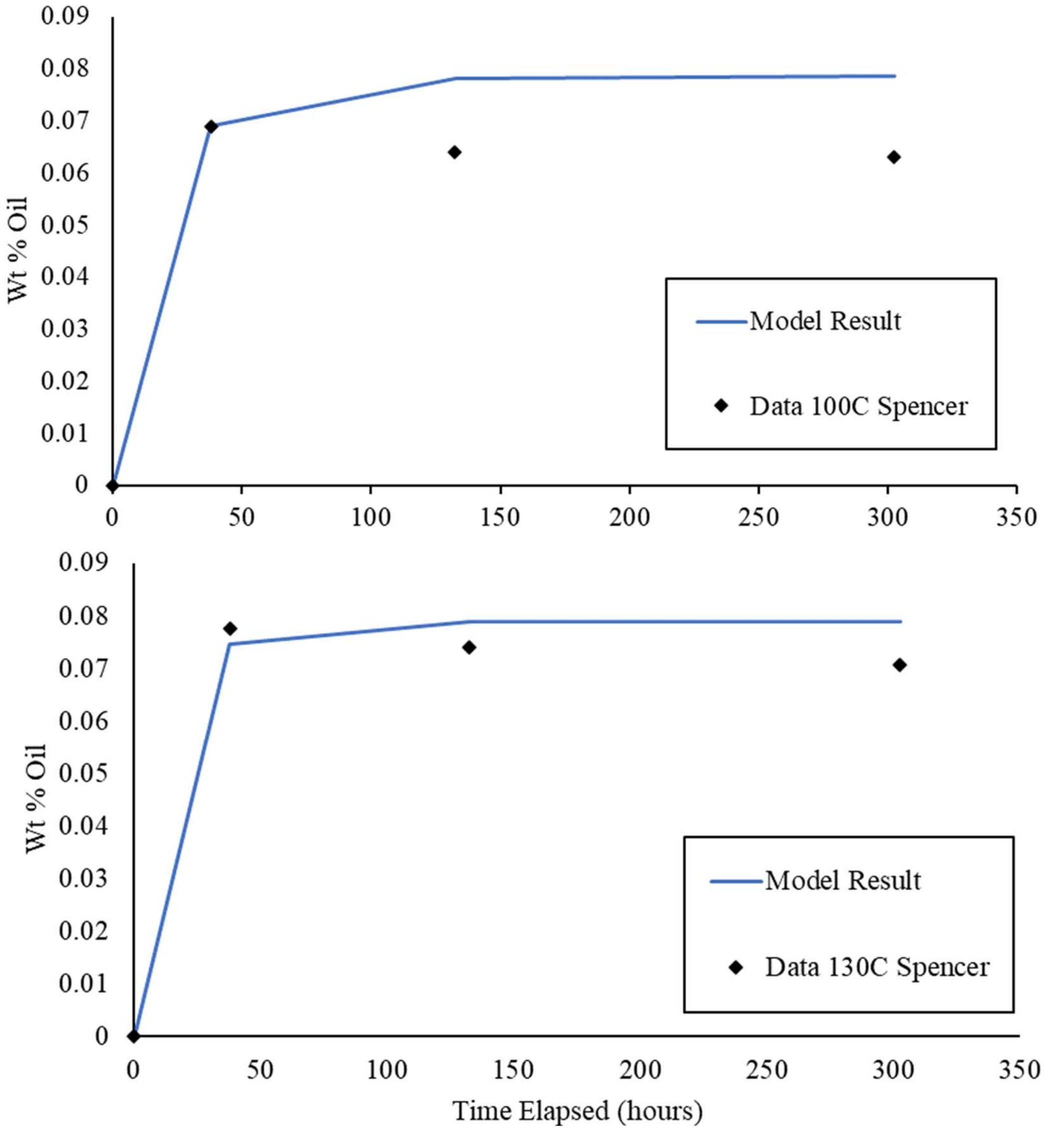

Figure 5.7. Comparison of absorption model results for a PA-based composite at 100-130 °C suspended in oil to data from Spencer (2021)

The last test case used for PA compares to data from Eftekhari and Fatemi [44], who tested PA-G in water at 23 °C and 85 °C. The estimated diffusion parameters from the reported data are $D_0 = 50600\ mm^2/hour$ and $E_D = 8.34 \times 10^{-20} J/mol$. The saturation concentration at 80 °C is estimated to be about 10%.

The results of these test cases – presented in Figure 5.8 – show poor agreement with the data, as a result of the saturation concentration not matching that of the data, highlighting the potential problems with the sigmoidal function described in Section 5.1.2.

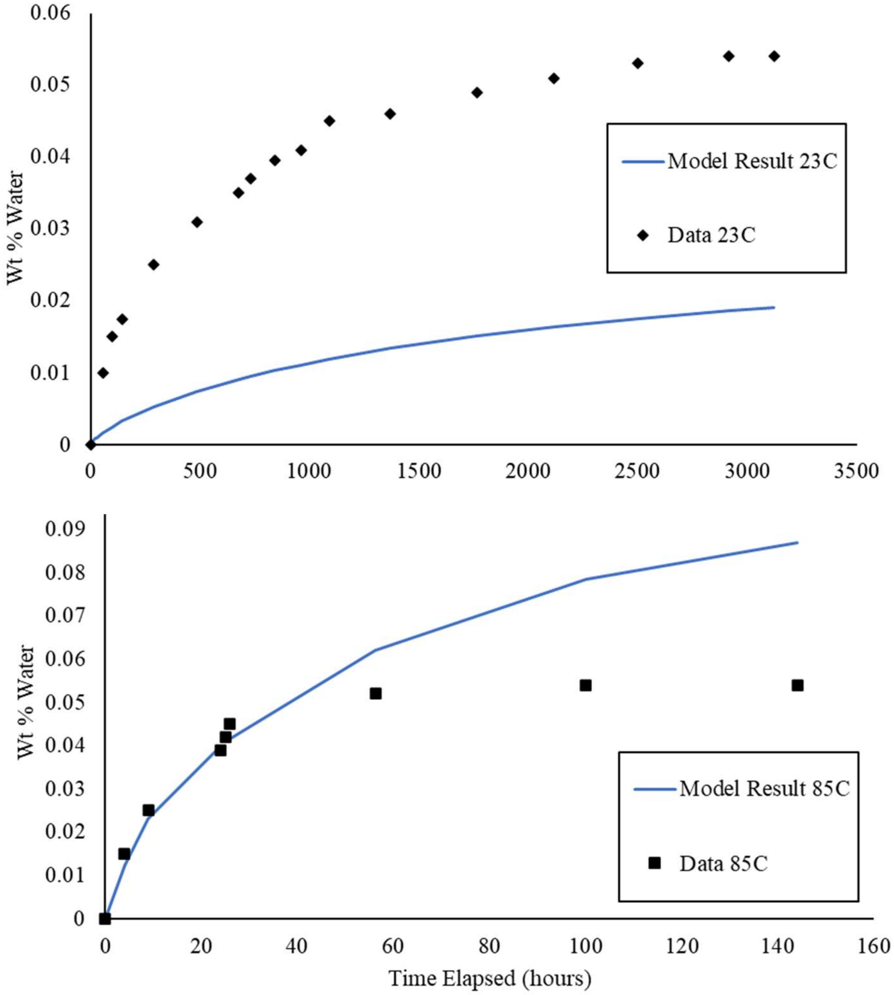

Figure 5.8. Comparison of absorption model results for a PA-based composite at 23-85 °C suspended in water to data from Eftekhari and Fatemi

5.3.3 Polypropylene Matrix

The first case presented for PP-matrix composites utilizes data from Robert et al. (2010) [46], who tested PP/G composite samples in tap water and saltwater for 196 days. In both cases, the saturation concentration was found to be roughly 3.75%. The first set of data shows the comparison to the saltwater samples, which were estimated to have $D_0 = 4.0\, mm^2/hour$ and $E_D = 2.10 \times 10^{-20} J/mol$.

The comparisons for the saltwater result at 23, 50, and 70 °C are shown in Figures 5.9 through 5.11, respectively. Good agreement is seen for the 23 °C and 70 °C case, but the saturation concentration seems to have been underestimated at 50 °C.

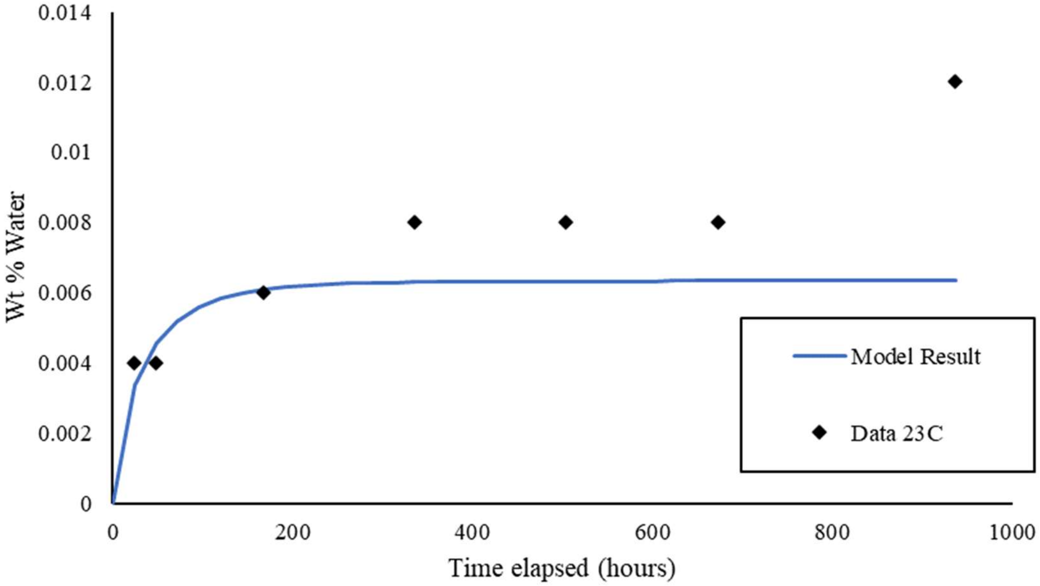

Figure 5.9. Moisture absorption of a PP-Glass composite model comparison to data at 23 °C from Robert et al.

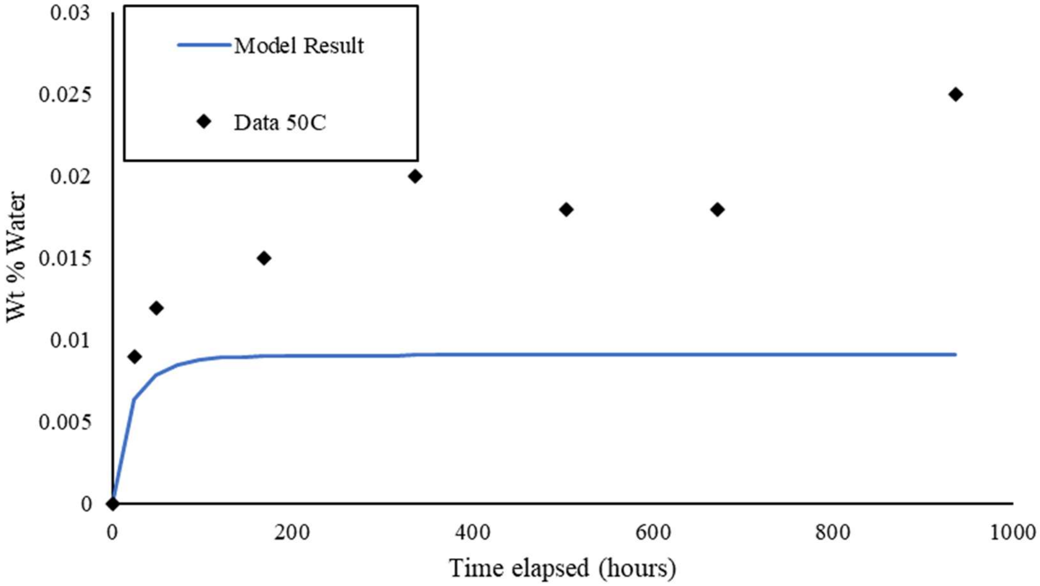

Figure 5.10. Moisture absorption of a PP-Glass composite model comparison to data at 50 °C from Robert et al.

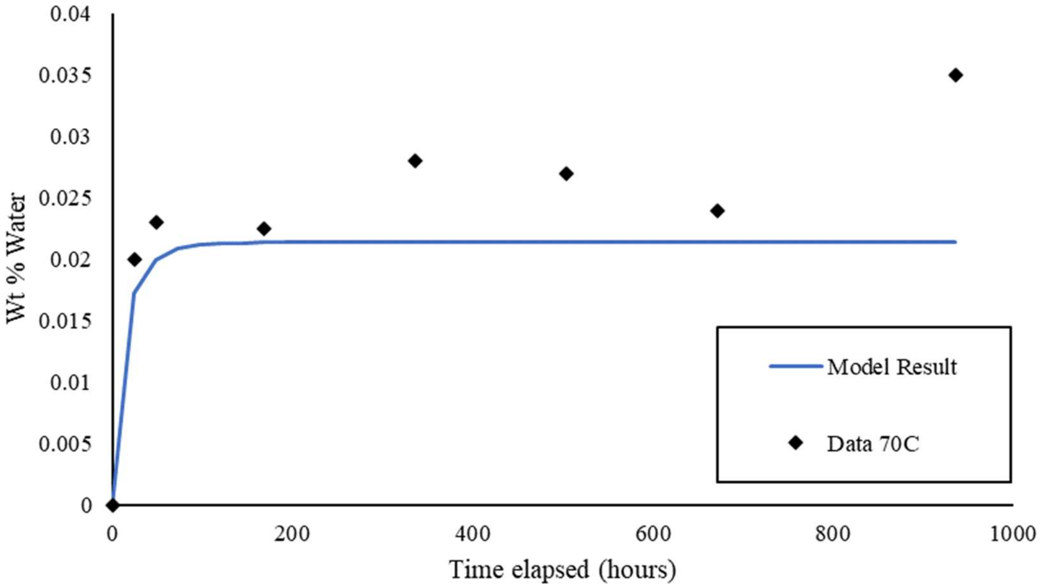

Figure 5.11. Water absorption of a PP-Glass composite exposed to salt water at 70 °C from Robert et al.

The next data set used to test the behavior of water absorption in PP-G materials came from Spencer (2021), who submerged thin samples in water at 50-80 °C for roughly one week. The estimated diffusion parameters from the reported data are $D_0 = 0.015\, mm^2/hour$ and $E_D = 2.22 \times 10^{-20} J/mol$. The saturation concentration at 80 °C is estimated to be about 0.95%.

The results of this test case are presented in Figure 5.12. Good agreement is seen for the 80°C case, but the model over-estimates the moisture absorption at 50 °C. It is noteworthy that the over-estimation of the saturation in this case is in contradiction to the under-estimation of the saturation concentration for the PA-G case shown in Figure 5.8. This implies that the function for estimating saturation concentration will need to be material-dependent to be accurate.

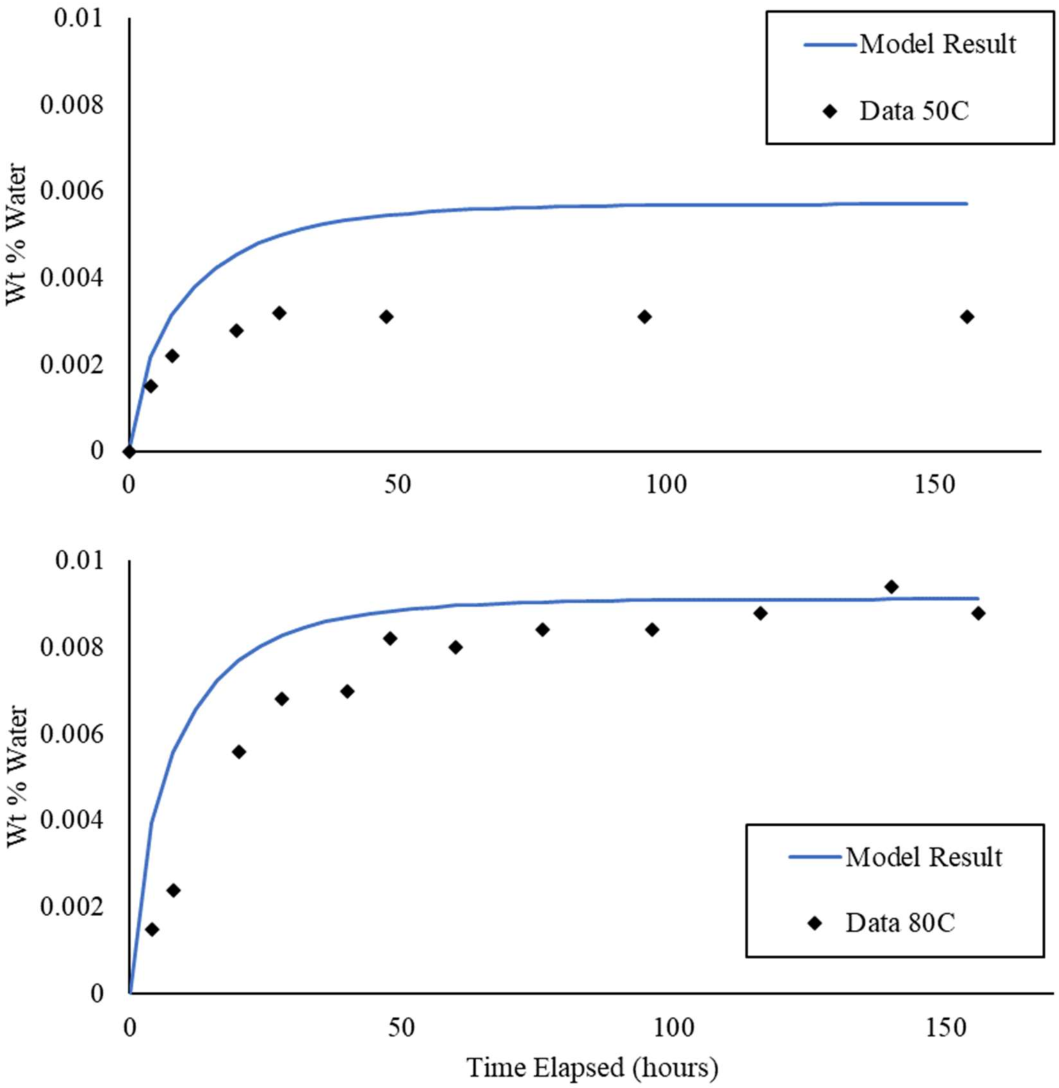

Figure 5.12. Comparison of absorption model results for a PP-G composite at 50-80 °C suspended in water to data from Spencer (2021)

The last test case also uses data from Spencer (2021) in which a PP-G sample was submerged in a pentane/toluene mixture at a range of temperatures from 25-100 °C. However, due to heavy dissolution of the samples at 85 °C and 100 °C, only the data from 25 °C was able to be used for comparison for fluid uptake. The estimated diffusion parameters from the reported data are $D_0 = 6.29\, mm^2/hour$ and $E_D = 2.86 \times 10^{-20} J/mol$. The saturation concentration at 80 °C is estimated to be about 2%.

The results of this model test are shown in Figure 5.13. The model underestimates the saturation concentration, but it is difficult to determine by what degree due to uncertainty in the data.

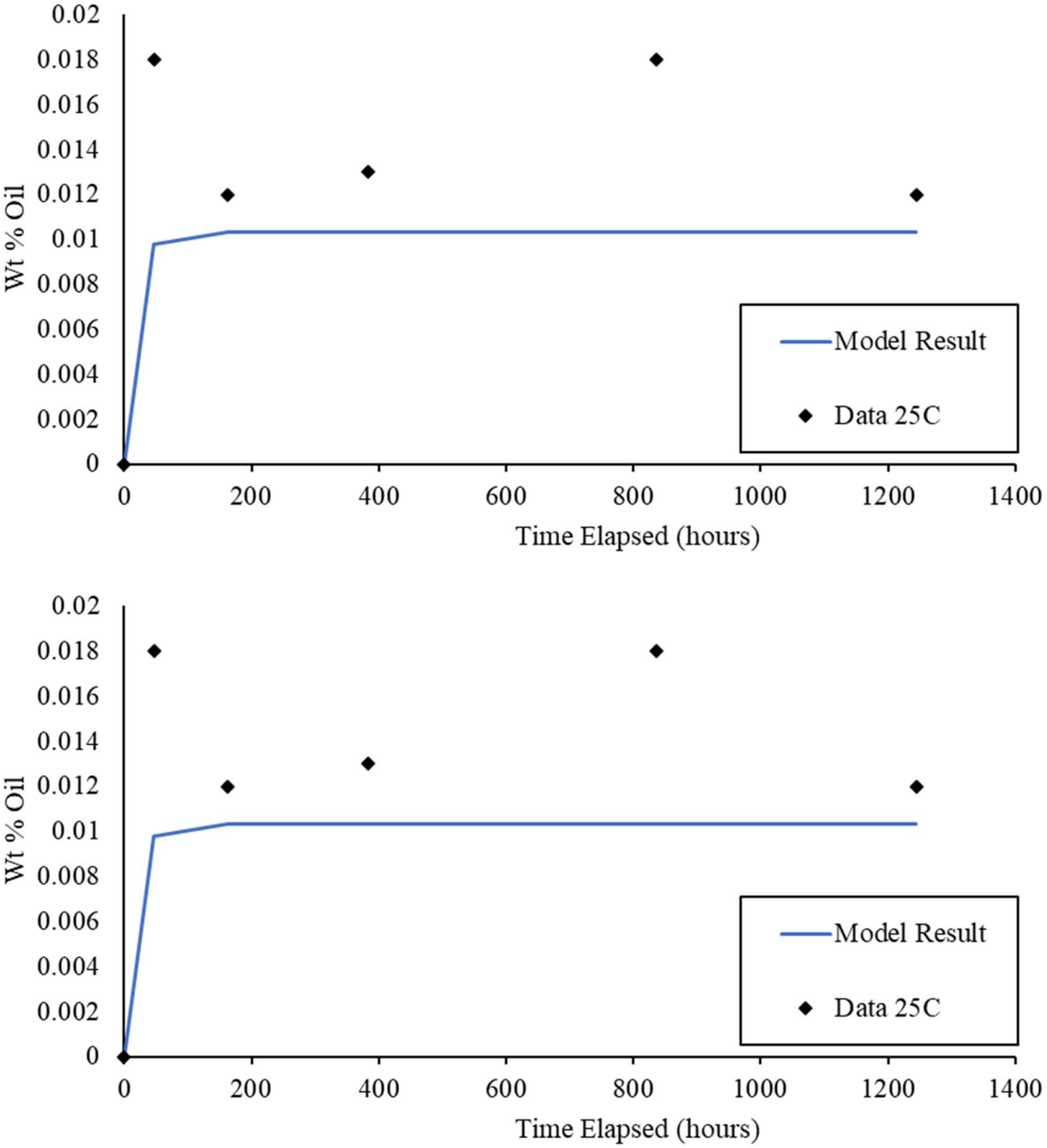

Figure 5.13. Comparison of absorption model results for a PP-G composite at 25 °C suspended in oil to data from Spencer (2021)

5.4 Summary

In this section, the methodology for determining the amount of absorption of water and/or oil-based fluids in the pipe wall over time considering the variability of diffusion parameters over time and space was described. A series of test cases were presented, and the model's results were compared to experimental data results from the research, for the same input data. Due to the case-specific data available for these data sets, agreement was generally good, but some issues remain with the estimation of the saturation concentration at lower temperatures.

6 Correlation of Fluid Uptake to Material Degradation

6.1 Introduction

Many factors – such as bonding quality, edge effects, dissolved salts, and pH, among others – influence the effects of fluid uptake and elevated temperatures on the degradation of laminate mechanical behavior. This introduces uncertainty into the prediction of degradation rates, even for the same input conditions.

To solve this problem, this work uses a Bayesian Network to correlate degradation rates with the local temperature and fluid absorption. This section describes Bayesian networks (BNs) as a modeling tool and the methods used to develop a BN for this application.

6.2 Bayesian Networks

A Bayesian Network, or BN, is a probabilistic model representing conditional dependencies of correlated events or conditions. This method can be used to approximate the relationship between two phenomena that are known to be related, but information to accurately quantify this relationship is lacking. As a modeling tool, BNs are highly versatile and have been used to describe correlated phenomena from a wide range of applications, from human reliability to physical material processes.

The basic formulation of a Bayesian network is that a "child" node with two or more possible states has the property of any one of its states being dependent on the states of a parent node. As a simple example, let's say there is a 75% chance of today being a cloudy day. If today is cloudy, there is a 15% chance of rain, but if it is not cloudy, there is only a 5% chance of rain. The BN representation of this example is shown in Figure 6.1. The final probability of rain, considering this uncertainty about cloudiness, would be calculated as shown in Eq. 6.1.

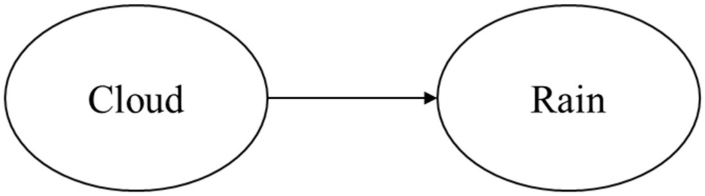

Not Cloudy	Cloudy
0.25	0.75

Cloud State	No Rain	Rain
Cloudy	0.85	0.15
Not Cloudy	0.95	0.05

Figure 6.1. A simple Bayesian Network example for clouds and rain

$$P(rain) = P(rain|clouds) * P(clouds) + P(rain|clear) * P(clear) = 0.15 * 0.75 + 0.05 * 0.25 = 0.125 \tag{6.1}$$

This basic method can be applied to more complex problems by using a mixture of existing data and informed opinion to fill out the table of conditional probabilities for the child node.

6.3 Model for Degradation Rates of Fiber Contribution and Matrix Properties

A BN is used here to approximate the effect of temperature, as well as the effects of absorbed hydrocarbons and water, on the degradation of matrix stiffness and debonding of fibers. The node at the middle layer in Figure 6.2, dissolution material loss, represents erosion and dissolution of outer layers of the pipe. Later developments of the model will add a dependence of this node on flow rate. This layer, as well as the X_{matrix} and X_{fiber} parameters, are conditionally dependent on the weight percentage of oil, weight percentage of water, and temperature of the individual ply.

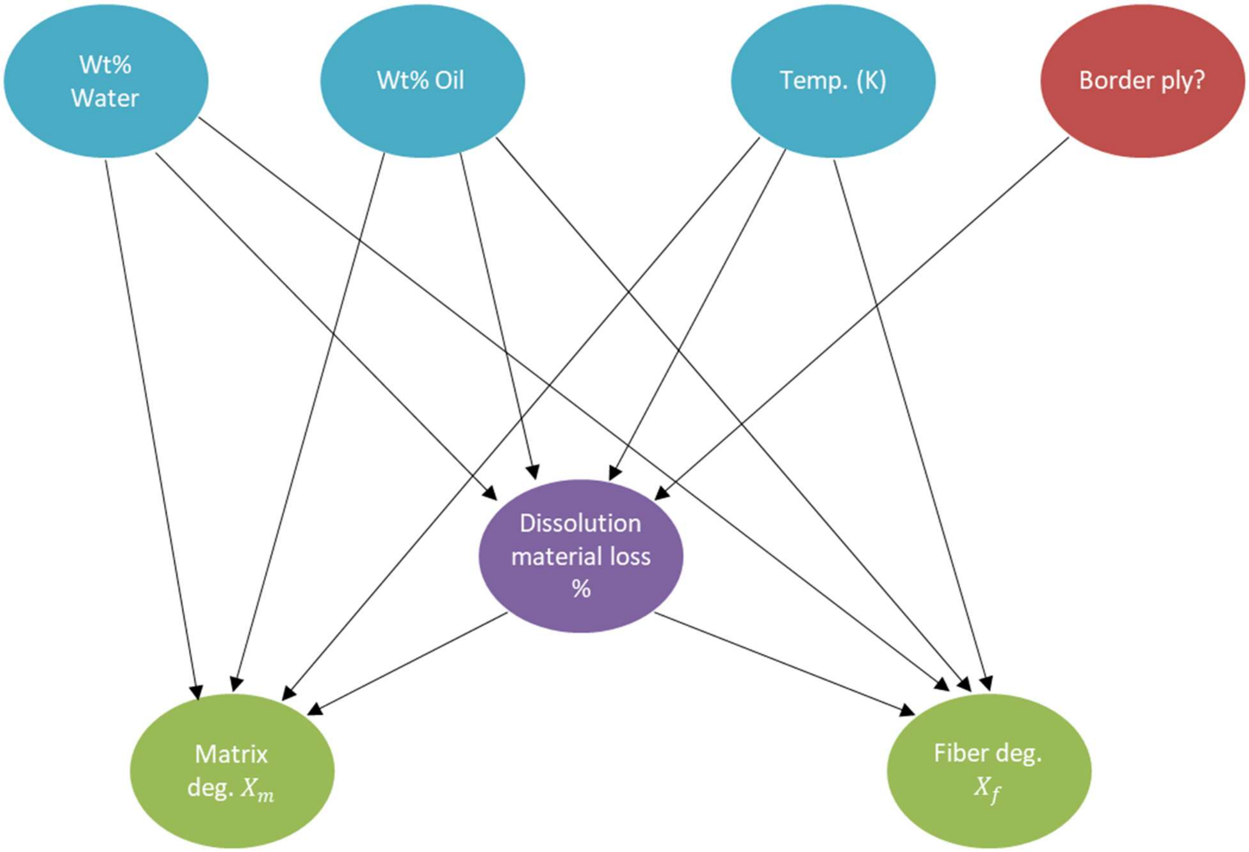

Figure 6.2. Bayesian Network used for this work

The outputs of the BN in Figure 6.2 are used to estimate the expected reduction in matrix stiffness and fiber bonding for a single time step within a defined region of the pipe. Four independent conditions are used as inputs in the BN: concentration of hydrocarbon/oil-based fluids, concentration of water-based fluids, temperature, and a binary node indicating if the region specified lies on the pipe's surface.

6.3.1 Input Nodes

Each input node's values are put into bins describing their states. The sizes of the bins were chosen based on a combination of availability of data for a range of conditions and how significantly changes to the inputs in a particular range affect the output nodes. These state bins are shown in Table 6.1.

Table 6.1. Input node states

Node name	Description	States
Wt % water	Weight percentage of water in the specified ply	<0.2% 0.2-1.0% 1.1-2.0% 2.1-3.0% 3.1-4.0% 4.1-5.0% >5%
Wt % oil	Weight percentage of oil in the specified ply	<1% 1.1-5.0% >5%
Temperature K	Temperature of the specified ply in Kelvins	<293 293-302 303-312 313-322 323-352 353-372 >373
Border ply	Simple check if ply is at the interior or exterior wall of the pipe	False True

Since these parameters are generated by the simulation, there are no fixed-state probabilities for these nodes.

For the ply temperature, the value determined by Eq. 4.4 is fit within one of the above bins. This is done by creating an array of 7 elements, matching the number of states. The array is filled using a set of binary logic statements checking if the local temperature is within that range. This is shown in Eq. 6.2.

$$\begin{bmatrix} T < 293 \\ 293 \leq T < 303 \\ 303 \leq T < 313 \\ 313 \leq T < 323 \\ 323 \leq T < 353 \\ 353 \leq T < 373 \end{bmatrix} \tag{6.2}$$

A small amount of variance is applied to the ply's water and oil concentration before the probability of these input's states are determined. This variance is applied to account for fluctuations in absorption data after saturation was reached that were not captured by the fluid absorption model. A normal distribution is used with the mean ($\mu_{C,water}, \mu_{C,oil}$) as the nominal concentration from the model, and the standard deviation as shown in Eq. 6.3.

$$\sigma_{C,water} = 0.02 * \mu_{C,water} + 0.0001 \tag{6.3}$$

$$\sigma_{C,oil} = 0.02 * \mu_{C,oil} + 0.0001$$

6.3.2 Material Loss

The intermediate degradation mechanism, material loss, has three output states which represent a percentage of the original material's weight that has been lost to dissolution:

- <0.1%
- 0.1-1%
- >1%

These states were chosen based on the available data on matrix dissolution. For samples of neat polymers, very large amounts of dissolution can occur, even up to the entire sample if it is thin enough. The presence of fibers inhibits dissolution. Additionally, it is assumed that layers that are not on the surface do not undergo dissolution, as there is no body of fluid to carry material away.

Data on polymer dissolution used in the model is shown in Table 6.2. These data points were obtained by averaging the reduction in mass following an initial rise due to fluid uptake.

Table 6.2. Data Used for Prediction of Polymer Dissolution

Source	Matrix	Fiber	Medium	Fluid conc.	T	Loss
Spencer (2021) [49]	PA	C	Water	0.013	403.2	0.24%
Spencer (2021) [49]	PP	G	Oil	0.017	298.2	0.5%
Spencer (2021) [49]	PP	G	Oil	?	373.2	1%
Spencer (2021) [49]	PP	G	Oil	0.009	358.2	1.1%
Spencer (2021) [49]	PP	N/A	Oil	0.26	358.2	5%
Spencer (2021) [49]	PA	N/A	Water	0.013	373.2	0.24%
Le Gac et al. [61]	PA	N/A	Water	0.1	353.2	0.7%

The above data points constitute only a small subset of the total number of 294 possible combinations of inputs. Luckily, since the border ply input is a binary one which, if false, prevents the dissolution of the ply, only 147 of these combinations actually require data-based inputs. Since there is insufficient raw data to complete the conditional probability table for each of these input combinations, however, additional methods need to be used to fill in the combinations for which there is no data.

By organizing the data points in Table 6.2 by their individual input state conditions – weight % water, weight % oil, and temperature, general trendlines can be formed. These trends are used to fill the gaps in combinations of conditions. From this point on, the data is split up depending on whether the matrix was a polyamide (PA) matrix or a polypropylene (PP) or polyethylene (PE) one. This is due to the effects of hydrolysis having a strong effect on PA matrix materials, while not causing as much degradation on PE and PP matrix materials.

Material Loss PA

water %	% loss	oil %	% loss	T	% loss
<0.2%		<1%		<293	
0.2-1.0%		1.1-5.0%		293-302	
1.1-2.0%	0.24%	>5%		303-312	
2.1-3.0%				313-322	
3.1-4.0%				323-352	
4.1-5.0%				353-372	0.70%
>5%	0.70%			>373	0.24%

Figure 6.3. Material loss trend calculation table for PA

Material Loss PP and PE

water %	% loss	oil %	% loss	T	% loss
<0.2%		<1%	1.10%	<293	
0.2-1.0%		1.1-5.0%	0.50%	293-302	0.50%
1.1-2.0%		>5%	5.00%	303-312	
2.1-3.0%				313-322	
3.1-4.0%				323-352	
4.1-5.0%				353-372	3.05%
>5%				>373	1.00%

Figure 6.4. Material loss trend calculation for PP and PE

The trend data above was used to fill in the 174 combination of input states. The probability of resulting in any given material loss state given an input state combination is calculated from a normal distribution with a mean estimated from data (where available), data trends, and judgement based on knowledge of the physical processes (for example, it is assumed that, if no fluid at all is present, the material cannot undergo dissolution, even at high temperatures). The standard deviation for this normal distribution was generally set between 0.1 and 0.2, depending on the availability of data and the amount of certainty around the judgements made.

6.3.3 Polymer Degradation Modifier

The polymer degradation modifier is a parameter which scales a nominal rate of degradation, more details on which will be provided in Section 7. This modifier's main range is between 0 (no degradation) and 1 (full nominal degradation), but a negative modifier can be used to represent cases of gradual recovery of mechanical properties, and modifiers greater than 1 may be used for cases with greater than nominal degradation.

As the main range for this modifier is between 0 (0%) and 1 (100%), the states of this parameter are organized into ten bins ranging from <1% loss to >80% loss, with 10% increments for all but the first and last bins. This parameter is considered to be dependent on the absorbed amount of both fluid types, the local temperature, and the extent of material loss, for a total of 441 input combinations.

Data on polymer mechanical property reductions is taken from roughly 50 experimental data points on either neat polymer samples or matrix-dominant properties (i.e. transverse or compressive) from Arhant et al. (2015) [42], Le Gac et al. (2017) [61], and Spencer (2021) [49]. Because of significant differences in the degradation behavior between PA and PP/PE based composites, the data was split between these two groups, then organized according the associated water/oil concentration, temperature, and degree of material mass loss from the original data. This allowed for trends based on a single parameter to be determined as shown in Figures 6.5 and 6.6 for PA and PP/PE respectively.

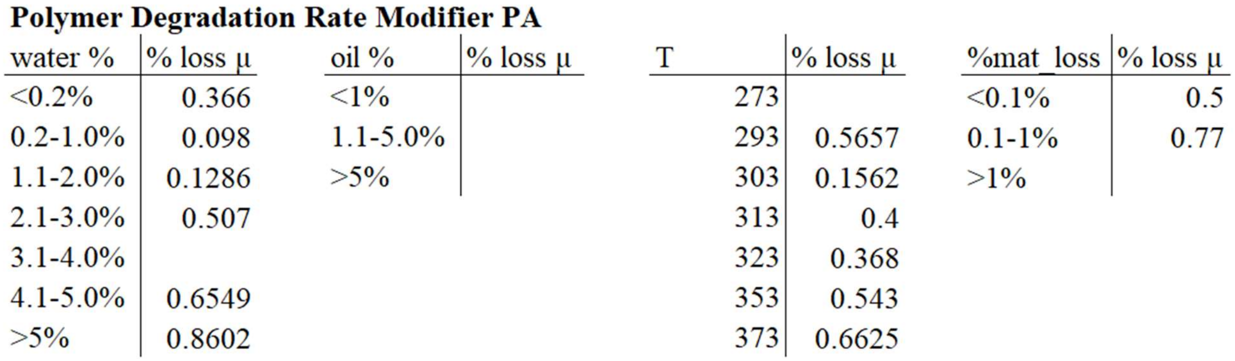

Polymer Degradation Rate Modifier PA

water %	% loss μ
<0.2%	0.366
0.2-1.0%	0.098
1.1-2.0%	0.1286
2.1-3.0%	0.507
3.1-4.0%	
4.1-5.0%	0.6549
>5%	0.8602

oil %	% loss μ
<1%	
1.1-5.0%	
>5%	

T	% loss μ
273	
293	0.5657
303	0.1562
313	0.4
323	0.368
353	0.543
373	0.6625

%mat_loss	% loss μ
<0.1%	0.5
0.1-1%	0.77
>1%	

Figure 6.5. Trend analysis for polymer degradation rate multiplier for PA-based composites

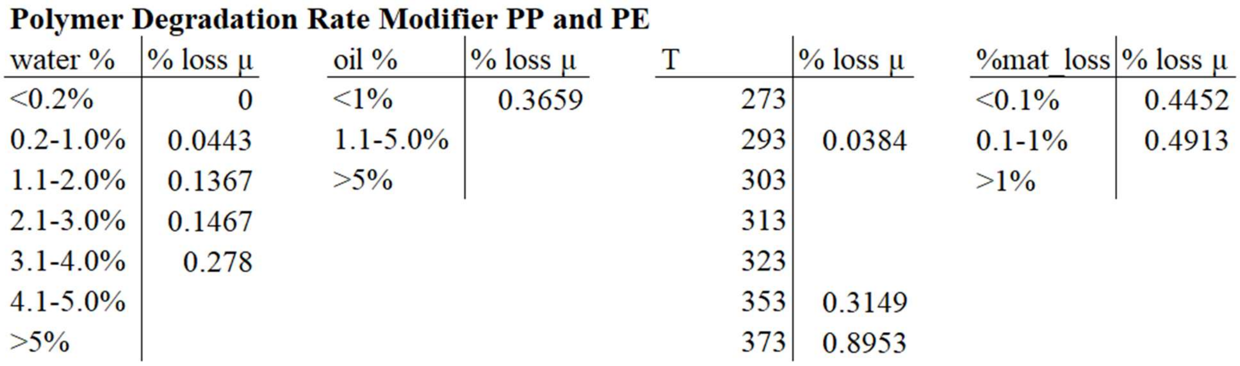

Polymer Degradation Rate Modifier PP and PE

water %	% loss μ
<0.2%	0
0.2-1.0%	0.0443
1.1-2.0%	0.1367
2.1-3.0%	0.1467
3.1-4.0%	0.278
4.1-5.0%	
>5%	

oil %	% loss μ
<1%	0.3659
1.1-5.0%	
>5%	

T	% loss μ
273	
293	0.0384
303	
313	
323	
353	0.3149
373	0.8953

%mat_loss	% loss μ
<0.1%	0.4452
0.1-1%	0.4913
>1%	

Figure 6.6. Trend analysis for polymer degradation rate multiplier for PE and PP-based composites

In addition to these trends, it was assumed that no significant degradation would occur below 273K. The conditional probability of each degradation state is calculated using a normal distribution with a mean determined by the experimental data trends, and a standard deviation between 0.1 and 0.2, depending on the availability of data for a particular combination of inputs.

As an example, Figure 6.7 shows data for polymer loss under the condition of no material dissolution, T between 293-302 K (these cells are hidden due to large numbers of merged rows), and less than 1% concentration of both oil and water. The mean and standard deviation are highlighted in pink where data was directly used to calculate these values, and highlighted in orange where the mean is estimated from the trends. The green highlighted values each represent the number of data points which fell into this range given the input conditions.

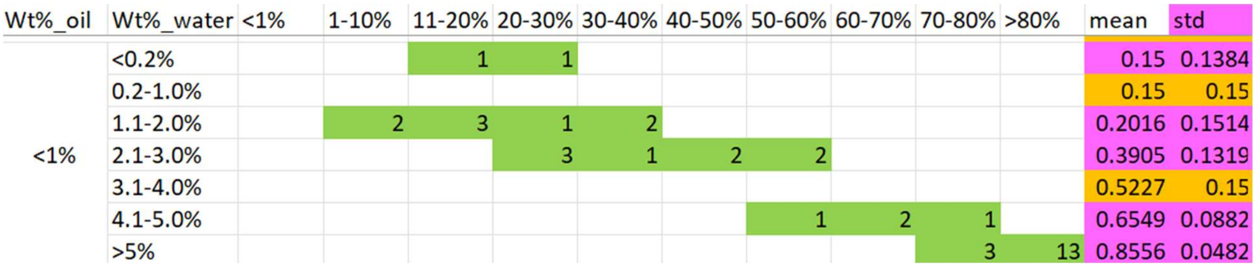

Wt%_oil	Wt%_water	<1%	1-10%	11-20%	20-30%	30-40%	40-50%	50-60%	60-70%	70-80%	>80%	mean	std
<1%	<0.2%			1	1							0.15	0.1384
	0.2-1.0%											0.15	0.15
	1.1-2.0%		2	3	1	2						0.2016	0.1514
	2.1-3.0%				3	1	2	2				0.3905	0.1319
	3.1-4.0%											0.5227	0.15
	4.1-5.0%							1	2	1		0.6549	0.0882
	>5%									3	13	0.8556	0.0482

Figure 6.7. A subset of the data used to generate the mean and standard deviations for the polymer degradation rate multiplier

6.3.4 Fiber Debonding Modifier

The fiber debonding or contribution loss rate modifier is a number between 0 and 1 which scales the nominal fiber debonding rate, which is explained in more detail in Section 7. Similar to the matrix degradation rate modifier, there are ten states for this parameter ranging from <1% to >80% of the nominal value, with 10% increments for all but the first and last bins. The trend analysis for this parameter uses experimental data from Arhant et al. (2015) [42], Le Gac et al. (2017) [61], Spencer (2021) [49], Robert et al. (2010) [46] and Eftekhari and Fatemi (2016) [44].

Fiber Contribution Loss Rate Modifier PA

water %	% loss μ
<0.2%	0.6
0.2-1.0%	
1.1-2.0%	0.376
2.1-3.0%	0.515
3.1-4.0%	0.512
4.1-5.0%	0.629
>5%	0.638

oil %	% loss μ
<1%	0.6146
1.1-5.0%	
>5%	

T	% loss μ
<293	
293-302	0.533
303-312	
313-322	
323-352	0.165
353-372	0.502
>373	0.641

%mat_loss	% loss μ
<0.1%	
0.1-1%	
>1%	

Figure 6.8. Trend analysis for fiber debonding rate multiplier for PA-based composites

Fiber Contribution Loss Rate Modifier PP and PE

water %	% loss μ
<0.2%	0
0.2-1.0%	0.1224
1.1-2.0%	0.16
2.1-3.0%	0.1327
3.1-4.0%	0.2783
4.1-5.0%	
>5%	

oil %	% loss μ
<1%	0.6146
1.1-5.0%	
>5%	

T	% loss μ
273	
293	0.0974
303	
313	
323	0.245
353	0.514
373	0.7329

%mat_loss	% loss μ
<0.1%	
0.1-1%	
>1%	

Figure 6.9. Trend analysis for fiber debonding rate multiplier for PE and PP-based composites

Notably, no data on the effects of material loss on the fiber contribution loss modifiers was available, so no trends could be determined quantitatively. It was assumed that partial dissolution of the matrix would have a significant effect on fiber bonding, with each progressive increase in the state of the mass loss increasing the average fiber debonding modifier by 10%.

6.4 Implementation of the Bayesian Network Method in the Model Code

Within the context of the model, the degradation rate modifiers are tracked as the variables X_{matrix} and X_{fiber}, which are calculated for each ply using the temperature and the concentration of water and oil as inputs.

The methods described in sections 6.2 and 6.3 are used to obtain conditional probability tables for the material dissolution, material degradation modifier, and fiber debonding modifier, which are stored in CSV files that are read by the model.

The probability of individual material dissolution states are first calculated by multiplying the probability of each combination of input states by the array of conditional probabilities for the material dissolution states. This intermediate result is then used as an input in the calculation of polymer degradation and fiber debonding rates.

The result of the above process results in an array of probabilities for the states of X_{matrix} and X_{fiber}. For example, the resulting probability arrays may look like the one shown in Table 6.3 and 6.4 for matrix and fiber, respectively.

Table 6.3. Example state probability for X_{matrix}

<1%	1-10%	10-20%	20-30%	30-40%	40-50%	50-60%	60-70%	70-80%	>80%
0.025	0.05	0.05	0.1	0.1	0.25	0.15	0.1	0.075	0.1

Table 6.4. Example state probability for X_{fiber}

<1%	1-10%	10-20%	20-30%	30-40%	40-50%	50-60%	60-70%	70-80%	>80%
0.05	0.075	0.125	0.15	0.18	0.125	0.11	0.09	0.075	0.02

The values of X_{matrix} and X_{fiber} that will be used by the model are generated by taking the above tables as a discrete distribution for a random variable, then randomizing the parameters within a range of 0 to 1 accordingly. The application of these parameters to the degradation of the materials will be described in Chapter 7.

6.5 Summary

In this chapter, I introduced the methods used for estimating the severity of degradation relative to nominal rates for matrix mechanical properties and fiber debonding. A probabilistic approach to was used to capture the uncertainty in the change of mechanical properties that can result from exposure to environmental factors. Specifically, a Bayesian network linking the absorption of water- and oil-based fluids in a composite ply or polymer cover/liner, as well as the temperature of that ply or cover/liner to the severity of matrix property degradation and fiber bonding was developed and quantified by analysing the trends in experimental data.

7 Degradation of Mechanical Properties

7.1 Introduction

This section describes how mechanical properties of individual laminate plies are calculated at each time step using the degradation parameters calculated as described in Section 6. A new rule of mixtures method is used with additional modifications developed in this work to account for the degradation, and correlation between material stiffness and strength is considered using a covariance matrix.

7.2 Reversible Thermal Softening

Matrix mechanical properties are reduced at elevated temperature, partially due to permanent damage, and partially due to reversible softening. These property changes occur along the glass transition and melting temperature boundaries. To model this effect, the Young's modulus, tensile strength, shear modulus, and shear strength are all reduced according to Eq. 7.1, in which P_T is one of the aforementioned mechanical properties at a given temperature, T, and P_0 is the nominal value.

$$P_T = P_0 - \frac{P_0 - 0.6P_0}{1+e^{-0.1(T-T_g)}} - \frac{0.6P_0}{1+e^{-0.1(T-T_m)}} \tag{7.1}$$

The glass transition (T_g) and melting (T_m) temperatures used for polypropylene (PP), polyamide-6,6 (PA), and high-density polyethylene (PE) are shown in Table 7.1. To test the effects on a sample mechanical property, a sample Young's modulus (E_0)for each of these polymers is also provided in the table.

Table 7.1. Transition Temperatures and Sample Modulus for PP, PA, and PE

	T_g (K)	T_m (K)	E_0 (MPa)
PP	248	443	1200
PA	322	523	2500
PE	173	403	950

The change in Young's Modulus (*E*) with temperature has been plotted in Figure 7.1 for each of the three polymers for a range of -100 °C (173K) to 150 °C (523K). Each of these polymers is assumed to be semi-crystalline, so two transitions are observed.

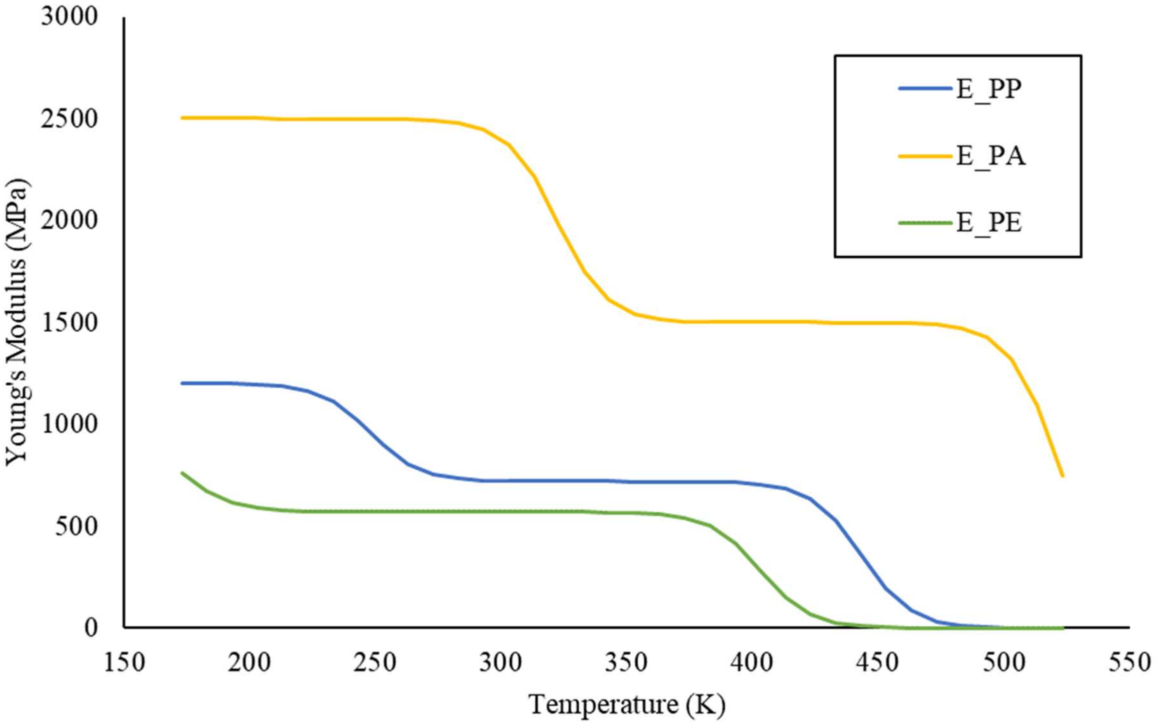

Figure 7.1. Sample Young's modulus as a function of temperature for PP, PA, and PE

7.3 Covariance of Component Stiffness and Strength

Material properties for the constituent matrix and fibers are determined from an input range, as described in Section 4. For the stiffness and strength, however, the random variables are considered to be covariant to each other. A covariance matrix was defined linking Young's modulus E, tensile strength F_T, and compressive strength F_C using available data on component and laminate properties.

To determine whether a covariance between two given parameters was appropriate, the properties in question were plotted against one another to test for correlation. To remove the effects of scale, each value was scaled to the maximum observed value for that property. The correlation between Young's modulus, tensile strength, and compressive strength are shown in figures 7.2 through 7.4.

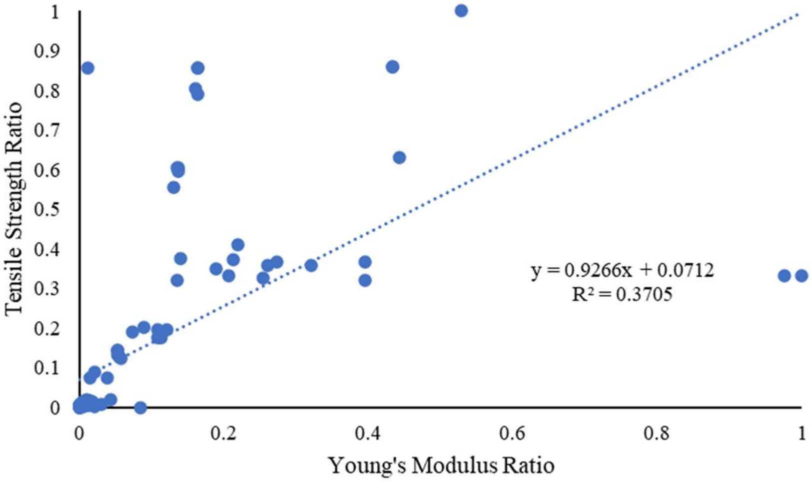

Figure 7.2. Graph of individual Young's modulus data points scaled to the maximum observed value versus scaled tensile strength points with correlation

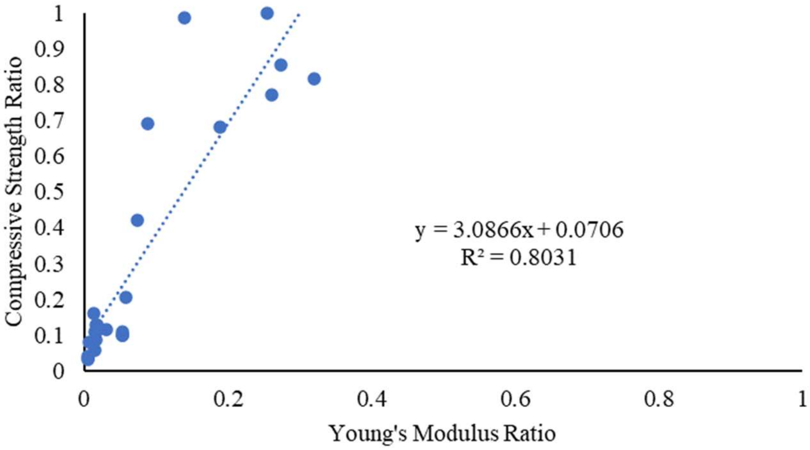

Figure 7.3. Graph of individual Young's modulus data points scaled to the maximum observed value versus scaled compressive strength points with correlation

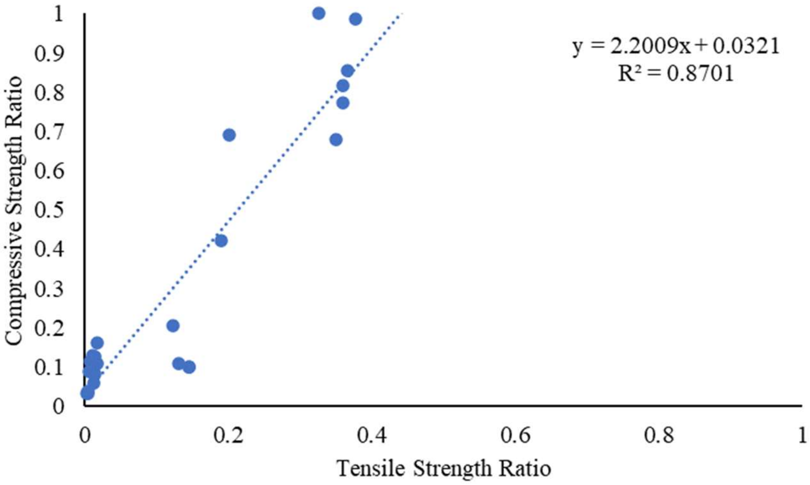

Figure 7.4. Graph of individual tensile strength data points scaled to the maximum observed value versus scaled compressive strength points with correlation

The Poisson ratio was also tested against the Young's modulus, tensile strength, and compressive strength, but no significant correlation was found so it was not considered to be covariant (Figure 7.5) with these parameters.

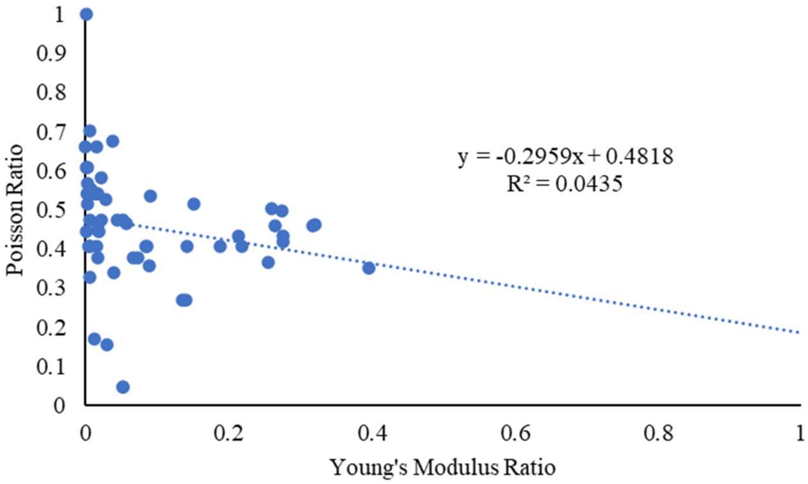

Figure 7.5. Graph of individual Poisson ratio data points versus scaled Young's modulus points. These parameters were found to not be correlated

For the correlated parameters, the covariance was calculated using Microsoft Excel's covariance function. The resulting covariance matrix for all data points is shown in Table 7.2.

Table 7.2. Covariance of All Data Points for Young's Modulus (YM), Tensile Strength (TS), and Compressive Strength (CS)

	YM	*TS*	*CS*
YM	0.52	0.727	0.629
TS	0.727	1.612	0.633
CS	0.629	0.633	0.868

When used in the model, this table is scaled to the desired material's observed variance by multiplying each row by the variance of that property (i.e. row one would be multiplied by the variance of the Young's modulus). This method was tested on a fiber with properties as shown in Table 7.3.

Table 7.3. Log-mean Young's Modulus (YM), Tensile Strength (TS), and Compressive Strength (CS) and their Respective Lognormal Variances

$ln(\mu_{YM})$	σ_{YM}	$ln(\mu_{TS})$	σ_{TS}	$ln(\mu_{CS})$	σ_{CS}
12.915	0.35	7.838	0.38	6.452	0.38

The resulting covariate properties, calculated using the exponent of a multivariate normal random number generator in Python, are shown in Figure 7.6.

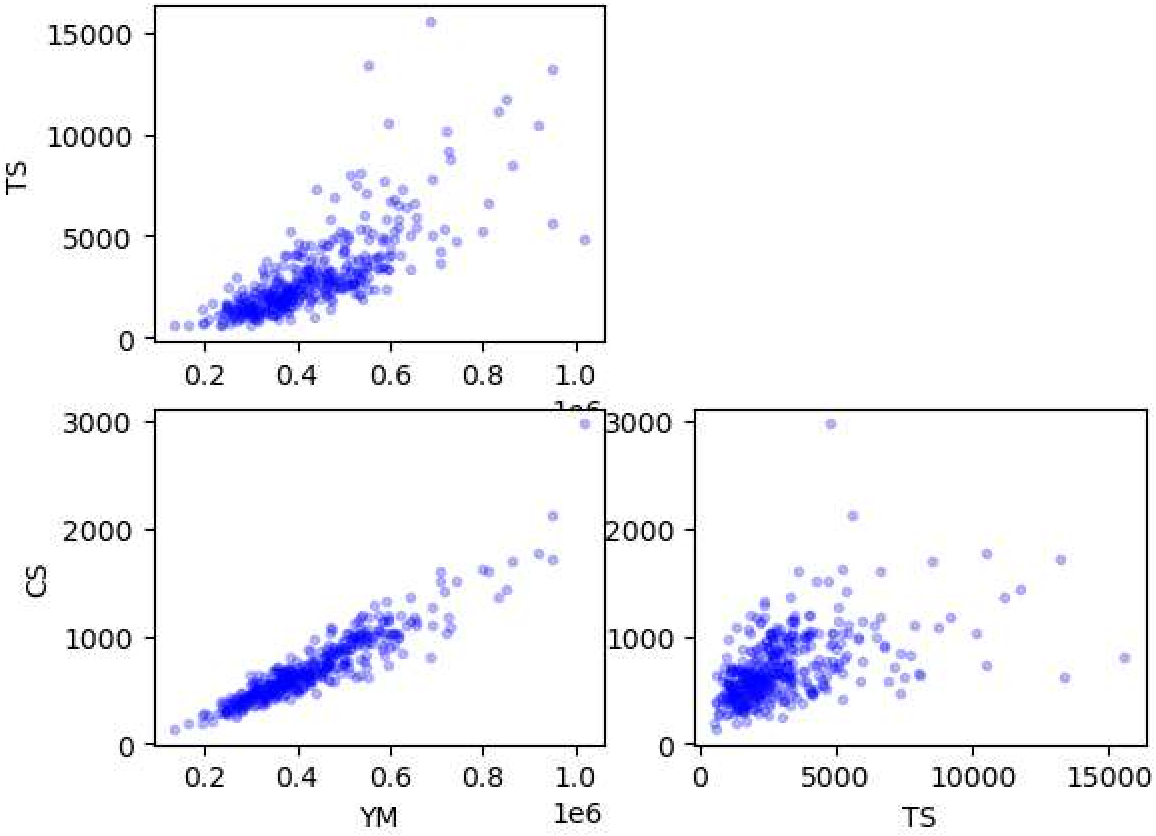

Figure 7.6. Covariance of Young's modulus, tensile strength, and compressive strength for a sample fiber

7.4 Determination of Undamaged Laminate Properties

This work calculates laminate properties from constituent (fiber and matrix) properties generally using the rule of mixtures, with some noteworthy exceptions which will be further explained in this section.

First, using the volume fraction of fibers V_f, and voids V_g, the matrix volume fraction V_m is calculated as shown in Eq. 7.2.

$$V_m = 1 - \left(V_f + V_g\right) \tag{7.2}$$

7.4.1 Mechanical Properties

Many mechanical properties have been calculated using modified equations from the New Rule of Mixtures developed by Xin et al. (2019) [62] and Shen et al. (2006) [63].

The laminate moduli in the longitudinal (1) and transverse (2,3) directions can be calculated from the fiber and matrix Young's moduli, E_f and E_m, according to equations 7.3 and 7.4, respectively.

$$E_1 = E_f V_f + E_m V_m \tag{7.3}$$

$$E_2 = E_3 = \frac{E_f E_m \left(V_f + \eta_1 V_m\right)}{E_m V_f + E_f \eta_1 V_m} \tag{7.4}$$

The η_1 parameter from Eq. 7.4 is calculated as shown in Eq. 7.5, where υ_m is the matrix Poisson ratio.

$$\eta_1 = \frac{0.2}{1-\upsilon_m}\left(1.1 - \left(\frac{E_m}{E_f}\right)^{0.5} + \frac{3.5E_m}{E_f}\right)\left(1 + 0.22V_f\right) \tag{7.5}$$

The shear moduli in the 12, 13, and 23 directions are calculated according to equations 7.6 and 7.7.

$$G_{12} = G_{13} = (1 - C){G^I}_{21} + C{G^{II}}_{21} \tag{7.6}$$

$$G_{23} = \frac{G_f G_m (V_f + \eta_2 V_m)}{G_m V_f + G_f \eta_2 V_m} \tag{7.7}$$

The η_2 parameter in Eq. 7.7 is calculated according to Eq. 7.8.

$$\eta_2 = 0.388 - 0.665 \left(\frac{E_m}{E_f}\right)^{0.5} + \frac{2.56 E_m}{E_f} \tag{7.8}$$

The parameters $G^I{}_{21}$ and $G^{II}{}_{21}$ were developed by Shen et al. [63] and Wang et al. (2021) [57] for the shear stiffness in the 12 and 13 directions because it was found that the rule of mixtures, which assumes properties can be calculated as entirely transverse (series) or longitudinal (parallel) – as seen in Figure 7.7 – was insufficient for accurate predictions of the shear modulus.

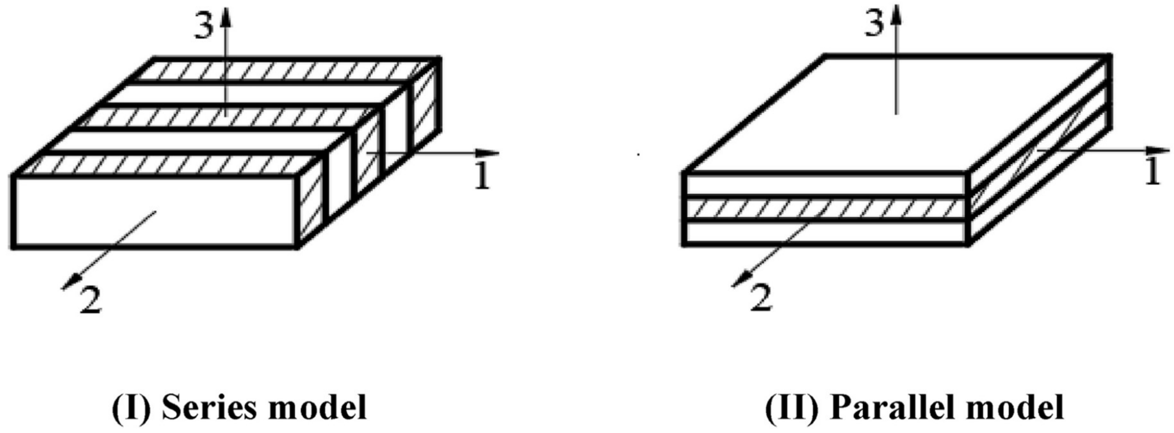

Figure 7.7. Simplified model of a laminate from Shen et al.

The modified G_{12} and G_{13} in this model is therefore a combination of the series (I) and parallel (II) models, which are shown individually in Eq. 7.9. The variable C used in Eq. 7.6 is the contact coefficient which was set as 0.2 according to Shen et al. [63].

$$G^I{}_{12} = \frac{G_f G_m}{G_m V_f + G_f V_m}$$

(7.9)

$$G^{II}{}_{12} = G_f V_f + G_m V_m$$

The Poisson ratio in the 12 and 13 directions are calculated with a similar method to the shear stiffness, as shown in Eq. 7.10. This method generally results in a lower Poisson ratio than either of the constituent materials.

$$\nu_{12} = \nu_{13} = \frac{E_2}{E_1}\left((1-C){\nu^I}_{21} + C{\nu^{II}}_{21}\right) \tag{7.10}$$

The series and parallel estimates of the Poisson ratio used for the combined equation are shown in Eq. 7.11.

$$\begin{aligned} {\nu^I}_{21} &= \nu_f V_f + \nu_m V_m \\ {\nu^{II}}_{21} &= \frac{\nu_f E_f V_f + \nu_m E_m V_m}{E_m V_f + E_f V_m} \end{aligned} \tag{7.11}$$

The tensile strength in the longitudinal direction, X_T, is calculated according to Eq. 7.12.

$$X_T = X_{fT}\left(V_f + \frac{E_m V_m}{E_f}\right) \tag{7.12}$$

The longitudinal compressive strength, X_C, is calculated according to Eq. 7.13, where β is about 0.28 for the fiber buckling mode according to Shen et al. [62].

$$X_c = 2V_f\sqrt{\frac{\beta E_f E_m V_f}{3V_m}} \tag{7.13}$$

The transverse tensile (Y_T, Z_T) and compressive (Y_C, Z_C) strength are calculated using equations 7.14 and 7.15. The compressive strength uses the compressive failure strain of the matrix (ε_{mC}).

$$Y_T = Z_T = X_{fT}\left[1 - \sqrt{\frac{4V_g}{\pi(1-V_f)}}\right]\left[1 + \left(V_f - \sqrt{V_f}\right)\left(1 - \frac{E_m}{E_f}\right)\right] \tag{7.14}$$

$$Y_C = Z_C = E_2\varepsilon_{mC}\left[1 - \sqrt{\frac{4V_f}{\pi}}\left(1 - \frac{E_m}{E_f}\right)\right] \tag{7.15}$$

The shear strengths in the 12, 13, and 23 directions are all calculated from the matrix and fiber shear stiffness using through the normal rule of mixtures, as shown in Eq. 7.16.

$$X_{12} = X_{12,f}V_f + X_{12,m}V_m \tag{7.16}$$

7.4.2 Thermal Properties

The coefficient of thermal expansion, α in the longitudinal and transverse directions are calculated using equations 7.17 and 7.18, respectively. The longitudinal coefficient is assumed to be dominated by the fiber properties, with the transverse property behaving as a mixture.

$$\alpha_1 \cong \alpha_{1,f} \tag{7.17}$$

$$\alpha_3 = \alpha_2 = \alpha_{2,f}V_f + \alpha_{2,m}V_m \tag{7.18}$$

The thermal conductivity and convective heat transfer coefficients are also assumed to behave as a mixture of the constituent properties and is defined using Eq. 7.19 and 7.20

$$k = k_fV_f + k_mV_m \tag{7.19}$$

$$h_0 = h_{0f}V_f + h_{0m}V_m \tag{7.20}$$

7.5 Modification for Degradation Parameters

As in the previous section, I assume the composite is manufactured as a series of bonded layers, or plys. Degradation of ply stiffness or strength can in principle be caused by three factors: (1) reduced matrix stiffness from diffusion or temperature change, (2) degradation of the fiber materials, and (3) fiber debonding from the matrix, which causes the fibers to not attract load from the matrix, thereby effectively introducing more "void" space within the matrix. Factor 2 is neglected here because the fibers have been shown to be highly resistant to degradation (Section 1.3.5). Factor 3 is parameterized by a dimensionless factor, R_{fiber}, that takes on values ≤ 1.0 that indicate the fraction of fiber volume that still participates in load transfer. This modifies Eqs. 7.3 through 7.16 such that the fiber volume fraction becomes the reduced fiber volume fraction, shown in Eq. 7.21.

$$V_f^* = V_fR_f \tag{7.21}$$

Additionally, the matrix Young's Modulus, E_m, shear modulus, G_m, and tensile strength X_{mT} are reduced. These reduced properties may be abstracted as $P_{matrix,R}$, where P_{matrix} is one of the aforementioned matrix properties.

The reduction of composite property P_{matrix} to $P_{matrix,R}$ is a time-dependent degradation process. This process is modelled using an hourly percentage loss rate, δ. For example, consider a polyamide polymer that has a reduction in Young's Modulus of 85% (i.e., $P_{matrix,R}/P_{matrix}$= 0.15; [61]) after 30 days. In this case, the maximum hourly loss from degradation can be computed for the matrix (δ_M) as shown in Eq. 7.22.

$$\delta_M = \frac{85\%}{30\ days * 24\ hours/day} \approx 0.11\%/hour \tag{7.22}$$

While direct observation of the degree of fiber disbanding is difficult, the effects may be estimated by using fiber-dominant properties such as longitudinal stiffness. A maximum loss of 75% of fiber bonds after 60 days is assumed, resulting in the fiber degradation rate δ_F as shown in Eq. 7.23.

$$\delta_F = \frac{75\%}{60\ days * 24\ hours/day} \approx 0.05\%/hour \tag{7.23}$$

The reduced matrix property at time *t*, $P_{matrix,R}(t)$, is computed from that property at the previous time step, $P_{matrix,R}(t - \Delta t)$, with application of a reduction factor,

$$P_{matrix,R}(t) = P_{matrix,R}(t - \Delta t) * (1 - \delta_M * \Delta t * X_{matrix}) \tag{7.24}$$

where X_{matrix} is a factor used to scale δ_M for conditions in the composite that may differ from those used to define δ_M. Fiber debonding is another form of degradation captured by factor R_{fiber}; the evolution of this factor with time is similarly described as,

$$R_{fiber}(t) = R_{fiber}(t - \Delta t) * (1 - \delta_F * \Delta t * X_{fiber}) \tag{7.25}$$

where X_{fiber} similarly scales the δ_F value for varying conditions.

X_{matrix} and X_{fiber} are ratios between zero and one. A value of zero indicates no degradation for that time step, while a value of one indicates the nominal degradation rates apply (δ_M or δ_F). X_{matrix} and X_{fiber} are statistically dependent on the local temperature, as well as the concentrations of oil- and water-based fluids, but there is not sufficient data to define a deterministic relationship for these parameters. Hence, the values of these ratios are derived from a Bayesian network, as described in Section 6.

7.5.1 Recovery Module

Under favorable conditions – namely when the temperature is low and there is no fluid absorbed in the material – a small amount of recovery may occur for the initial properties. A model process was introduced to capture this recovery, by stating that if X_{matrix} is equal to zero, there is a 25% chance of X_{matrix} being set to -0.1, which would lead to a small increase in the matrix mechanical properties for that time step.

7.6 Degradation Results

In this section, the results of the degradation model under a variety of fluid absorption and elevated temperature conditions are presented. For each of these cases, the input conditions and relevant diffusion parameters will be provided, and the relative loss of the mechanical property reported by the data will be compared to the model result.

The first data comparison is to flexural stiffness loss data from Jha et al. (2015) [64]. This work tested the flexural stiffness of an 8-inch (203mm) diameter PA-Carbon composite pipe aged for 180 days at 65 °C in a) dry air, b) a wet and acidic environment, and c) a mixture of 70% Heptane, 20% Cyclo-Hexane, and 10% Toluene. Additionally, a load of first 0.04% and then 10% of the nominal 40 MPa internal pressure was applied to the pipe during aging. As details on the ply layup and fiber angles were not provided, the following design values were used based on common designs from other sources: nine 0.25mm thick reinforcement plies with a fiber angle ±55° and fiber volume fraction 0.6. A 2mm liner and cover were used as well. Additionally, since the fluid absorption results were not presented, diffusivity parameters from similar systems were used under diffusion method 1. These parameters are: $D_0 = 3.4\, mm^2/hour$ and $E_D = 3.0 \times 10^{-20} J/mol$. The fluid saturation levels were assumed to be 5% for water and 7% for oil. The results of the simulation at 0.04% of the nominal load are shown in Figure 7.8. Except for the water environment, very little degradation was observed, and some initial stiffening was observed due to the pressure loading improving consolidation of the laminate [64].

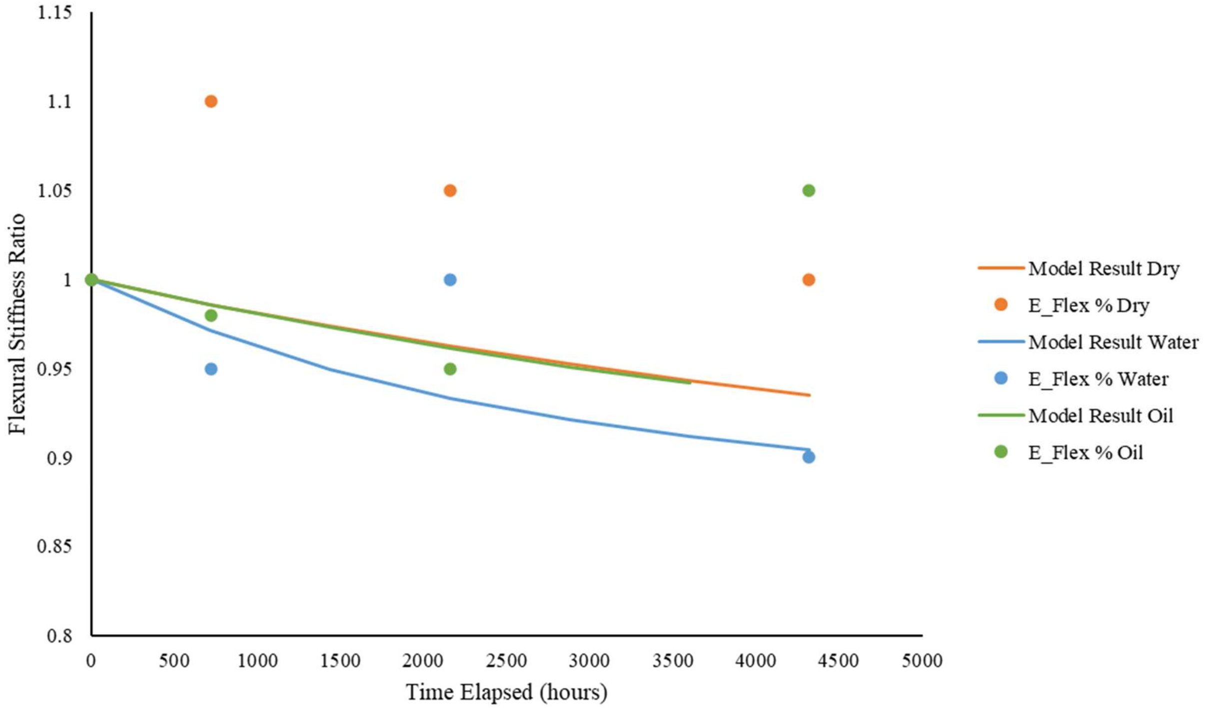

Figure 7.8. Simulation result comparison to experimental data from Jha et al. for flexural loss ratio under dry, wet, and oil aging conditions at 0.04% of nominal load

The same simulation was run for 10% of nominal pressure and compared to the experimental results. The model results were relatively unchanged by the different load condition as this load was not enough to cause ply failures. A greater degree of stiffness loss was observed with the experimental data, however, especially in the case of water exposure.

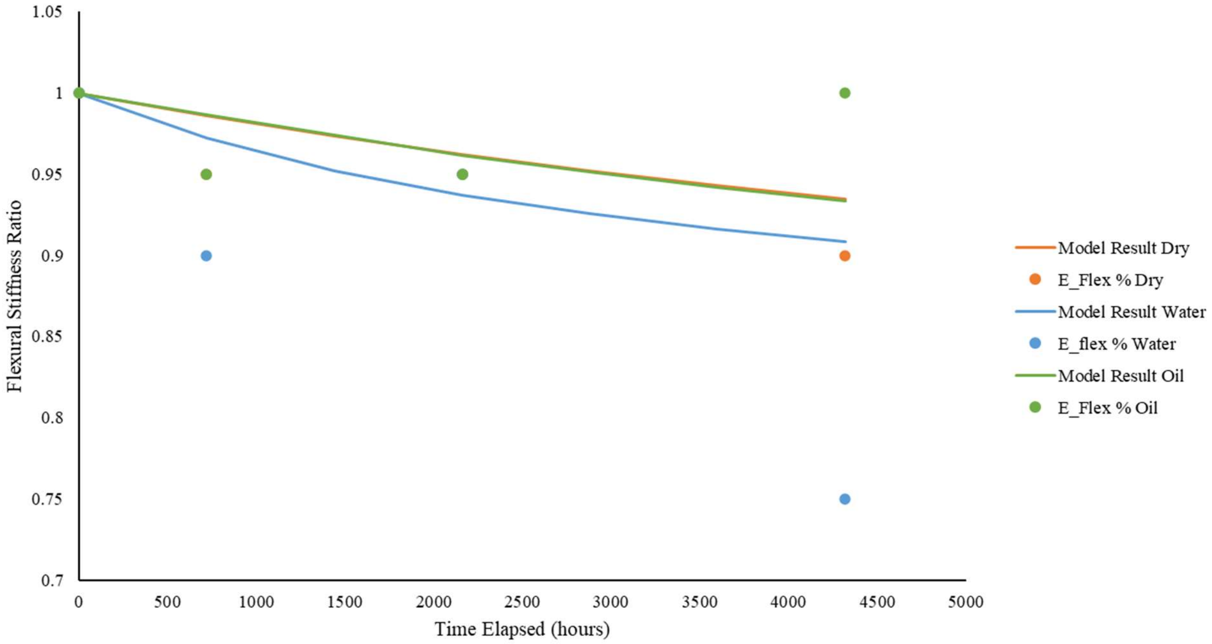

Figure 7.9. Simulation result for flexural loss ratio under dry, wet, and oil aging conditions at 10% of nominal load compared to experimental data from Jha et al.

The second data set used comes from Arhant et al., [42] who submerged 2mm, 50mm radius unidirectional PA-carbon composite pipes in water at 40 °C. The estimated diffusion parameters from the reported data are $D_0 = 27.17\, mm^2/hour$ and $E_D = 4.60 \times 10^{-20} J/mol$. The saturation concentration at 80 °C is estimated to be about 10%. Results of the diffusion test for this case are shown in Section 5.

Before and after aging, the axial compression strength of the pipe was tested. The results of the average and standard deviation before and after aging for 400 hours are shown in Table 7.4.

Table 7.4. Comparison of model compressive strength result after degradation to experimental data

	Model		***Data***	
	Average X_C *(MPa)*	*Standard dev.*	*Average* X_C *(MPa)*	*Standard dev.*
Unaged	1136.87	109.31	1385	101
Aged 40°C	966.55	94.22	571	37

The next data set used for comparison is from Robert et al. (2010) [46], who tested 20 PP/G composite samples in tap water and saltwater for 196 days. In both cases, the saturation concentration was found to be roughly 3.75%. The data used for this comparison is to the tap water samples, which were estimated to have $D_0 = 4.0\, mm^2/hour$ and $E_D = 2.10 \times 10^{-20} J/mol$.

The composite laminate consisted of four 0/90° plies with a fiber volume fraction of 0.6 and a void fraction of 0.08. The samples were 4mm thick, 20mm wide, and 96mm long.

The results for flexural strength degradation at 23, 50, and 70 °C are shown in Figures 7.10 through 7.12, respectively. The standard deviation around the model's average result and the data averages are shown on the plots. Good agreement was generally observed for the lower temperatures, but the model over-estimated the degradation at 70 °C.

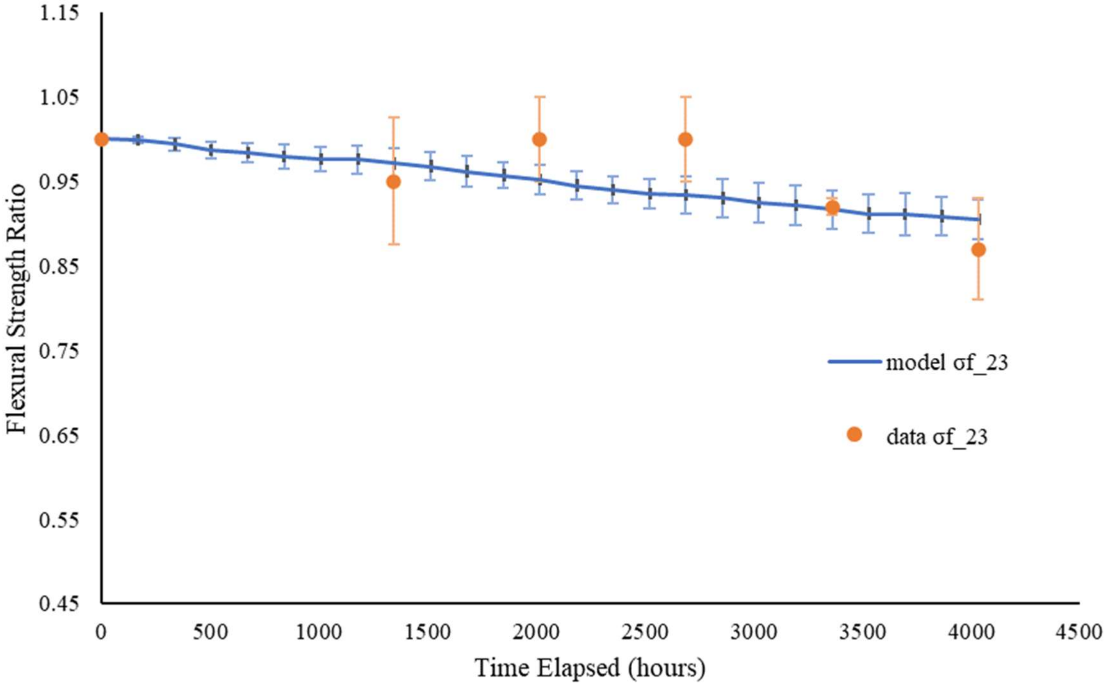

Figure 7.10. Flexural Strength loss at 23 °C compared to experimental data from Robert et al.

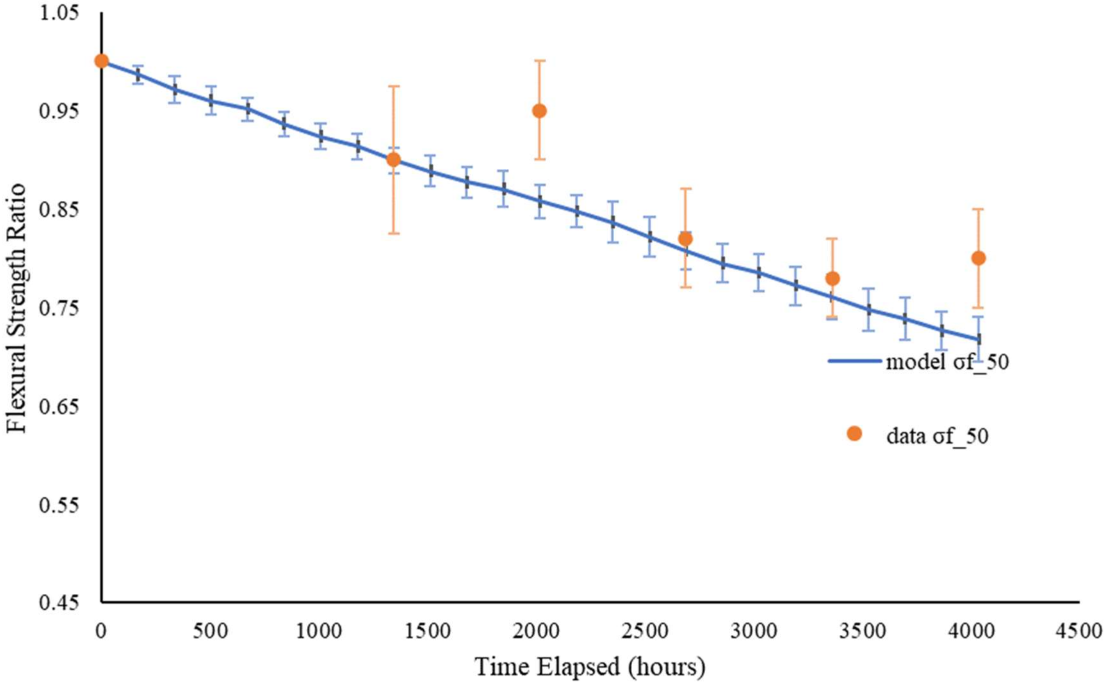

Figure 7.11. Flexural Strength loss at 50 °C compared to experimental data from Robert et al.

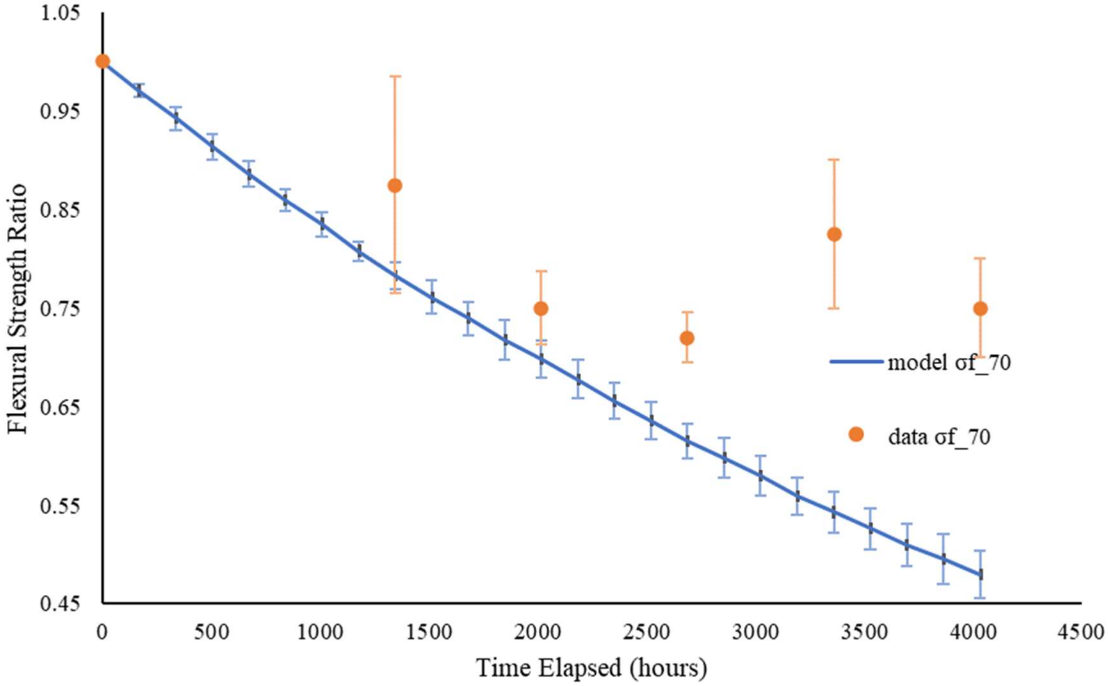

Figure 7.12. Flexural Strength loss at 70 °C compared to experimental data from Robert et al.

Results for the Young's modulus are shown in Figures 7.13 through 7.15 for 23, 50, and 70 °C. In the report by Robert et al., the Young's modulus was obtained from flexure data. Since the flexural modulus of an anisotropic material is not necessarily the same as the tensile modulus in either the longitudinal or transverse direction, the model results for both directions are plotted for comparison. The agreement for this case was generally good, with the longitudinal (E_1) modulus generally having better agreement than the transverse modulus (E_2).

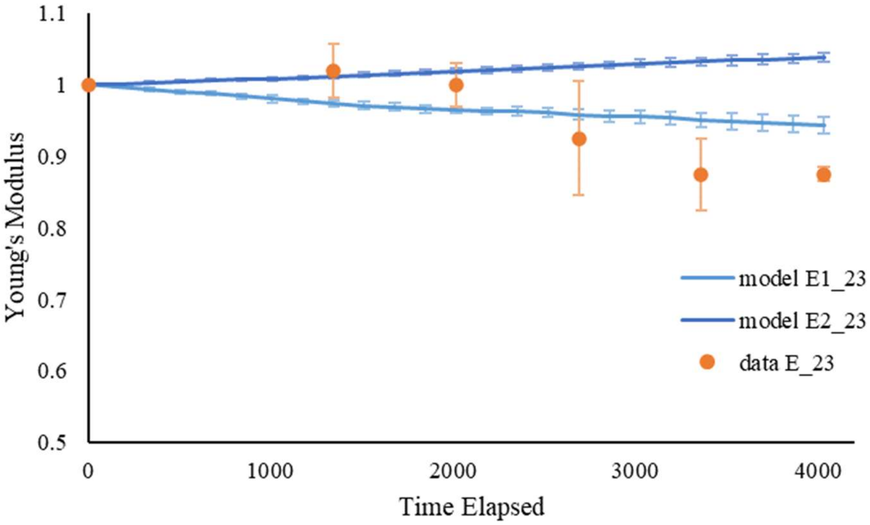

Figure 7.13. Young's modulus degradation model result comparison to experimental data from Robert et al. at 23 °C

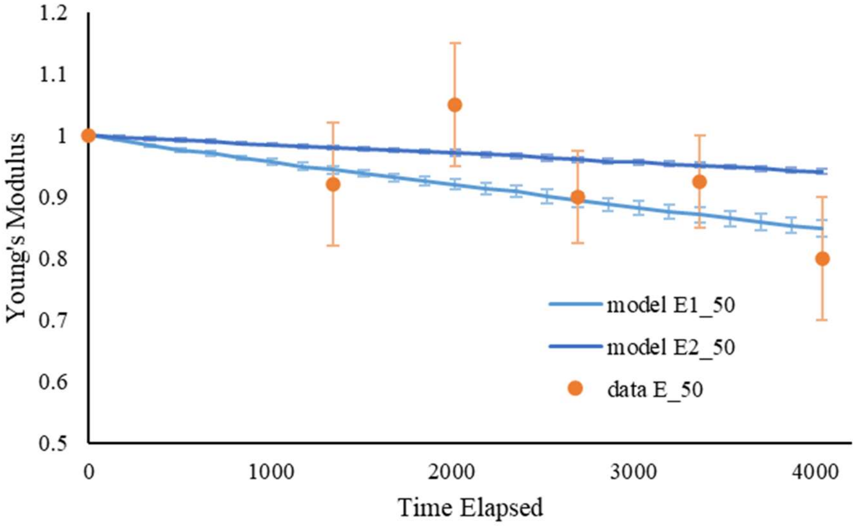

Figure 7.14. Young's modulus degradation model result comparison to experimental data from Robert et al. at 50 °C

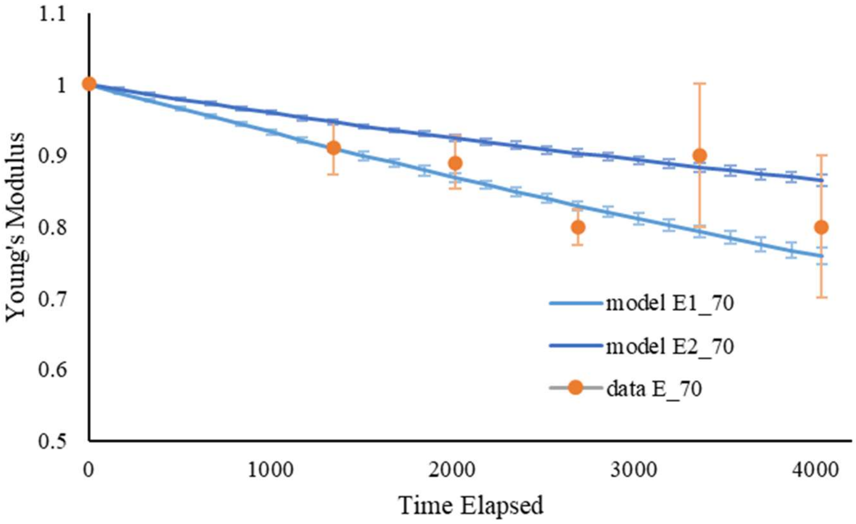

Figure 7.15. Young's modulus degradation model result comparison to experimental data from Robert et al. at 70 °C

The last data set used was from Spencer (2021) [49] who tested the interlaminar shear stiffness of PP-glass composite samples before and after aging in water and a pentane/toluene mixture at a range of temperatures. Dimensions of the samples were 5mm wide, 40mm long, and 0.25-0.5mm thick with a quasi-isotropic layup. The volume fraction of fibers was estimated to be about 0.55. The diffusivity parameters for water were estimated to be $D_0 = 0.015\,mm^2/hour$ and $E_D = 2.22 \times 10^{-20} J/mol$. The water absorption results for this case were described in Section 5. While this model does not determine interlaminar shear stiffness, the in-plane shear stiffness results from the model are compared to the experimental data in Table 7.5. In this case, the model underestimated the degradation from the water exposure.

Table 7.5. Comparison of model shear stiffness result after degradation to experimental data on interlaminar shear stiffness (ILSS) for two samples

	Model		***Data (Spencer)***	
	Average G_{23} *(MPa)*	*Standard dev.*	*ILSS 1 (MPa)*	*ILSS 2 (MPa)*
Unaged	10621.6	882.99	11851.9	10666.7
Aged 23°C	10498	876.34	6222.2	5600

The diffusivity parameters for oil were estimated to be $D_0 = 6.29\, mm^2/hour$ and $E_D = 2.86 \times 10^{-20} J/mol$. Similar to the water case, the results for the shear stiffness are shown after aging in oil at 25, 85, and 100 °C in Table 7.6. While more degradation was observed at the higher temperatures, the observed mechanical property loss is significantly lower than the experimental data. This is likely due to underestimating the degree of polymer dissolution which occurred in the experimental samples during exposure to the oil mixture.

Table 7.6. Comparison of model shear stiffness result after degradation to experimental data on interlaminar shear stiffness (ILSS) for two samples

	Model		***Data (Spencer)***	
	Average G_{23} *(MPa)*	*Standard dev.*	*ILSS 1 (MPa)*	*ILSS 2 (MPa)*
Unaged	10649.4	706.06	11428.6	10666.7
Aged 25°C	10192.7	673.32	8000	7000
Aged 85°C	7731.9	419.79	1185.2	923.08
Aged 100°C	7492	416.03	388.89	285.71

7.7 Summary

This chapter described how the mechanical and thermal properties of the laminate are determined from constituent matrix and fiber properties using a modified version of the rule of mixtures. Further modification is made to include the degradation rates, described in Chapter 6, which reduce the matrix stiffness and strength, and also to lower the effective fiber volume fraction using a reduction factor. These results were compared to experimental data to determine if the predictions are within an appropriate range. While some results showed good agreement, other cases underestimated the degradation.

8 Calculation of ply failures and estimation of burst probability

8.1 Introduction

This section describes how failure of thermoplastic components are defined in this work. Failure is defined in this work as the catastrophic burst or collapse of the laminate as described in Section 1.4.1, occurring when all plies have failed.

Once the laminate's current mechanical properties after degradation are calculated as described in Sections 6 and 7, the stress state is evaluated for the current combination of axisymmetric loads, as well as for thermal strains resulting from differences between the internal and external temperature.

Using knowledge of the stress state, a failure criterion such as maximum stress, Tsai-Hill, or Tsai-Wu is used to evaluate whether any of the laminate plies fail under the current stress state. Following the failure of one ply, a progressive failure approach will be used to assess the stress state of the remaining plies.

8.2 Calculation of Ply Stresses Under Axisymmetric Loading

An axisymmetric problem formulation assumes the loads, geometry, and material properties can be assumed as uniform around the circumference of the pipe. This assumption may be used in loading cases such as thermal gradients, axial tension or compression, torsion, or pressure, but it is not viable for lateral loads or flexure. This section will describe how the stress states of each ply can be determined for an axisymmetric case with a thermal gradient.

This problem formulation evaluates two-dimensional slice at an arbitrary coordinate on the length of the pipe with radial coordinates as shown in Figure 8.1.

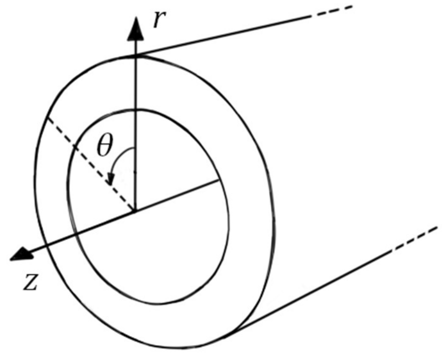

Figure 8.1. Radial axes for axisymmetric loading problem formulation

For an external temperature T_∞ and internal temperature T_0, the temperature at a given radius r between the inner radius r_0 and outer radius r_a can be calculated as shown in Eq. 8.1, reiterated from Section 4.

$$T = A + B\ln r \tag{8.1}$$

Where A and B are given in Eq. 8.2.

$$A = T_0 - B\ln r_0 \qquad B = \frac{T_\infty - T_0}{k\left(\frac{1}{r_a h_a} - \frac{1}{r_0 h_0}\right) + \ln(r_a/r_0)} \tag{8.2}$$

8.2.1 Determination of Ply Stress

The 3-D stress strain relationship for a given ply k is given by a modified Hooke's law as shown in Eq. 8.3, where k is the ply number counted from the innermost ply, σ_i and ε_i are the stress and strain in the i direction respectively, τ_{ij} and γ_{ij} are the shear stress and strain in the ij direction respectively, α_i is the thermal expansion coefficient in the i direction, and ΔT is the difference between the temperature at the minimum radius of the ply r_1 and maximum radius r_2 as obtained by Eq. 8.2.

$$\begin{bmatrix}\sigma_z\\ \sigma_\theta\\ \sigma_r\\ \tau_{\theta r}\\ \tau_{zr}\\ \tau_{z\theta}\end{bmatrix}^{(k)} = \begin{bmatrix}\bar{C}_{11} & \bar{C}_{12} & \bar{C}_{13} & 0 & 0 & \bar{C}_{16}\\ \bar{C}_{12} & \bar{C}_{22} & \bar{C}_{23} & 0 & 0 & \bar{C}_{26}\\ \bar{C}_{13} & \bar{C}_{23} & \bar{C}_{33} & 0 & 0 & \bar{C}_{36}\\ 0 & 0 & 0 & \bar{C}_{44} & \bar{C}_{45} & 0\\ 0 & 0 & 0 & \bar{C}_{45} & \bar{C}_{55} & 0\\ \bar{C}_{16} & \bar{C}_{26} & \bar{C}_{36} & 0 & 0 & \bar{C}_{66}\end{bmatrix}^{(k)} \begin{bmatrix}\varepsilon_z - \alpha_z \Delta T\\ \varepsilon_\theta - \alpha_\theta \Delta T\\ \varepsilon_r - \alpha_r \Delta T\\ \gamma_{\theta r}\\ \gamma_{zr}\\ \gamma_{z\theta} - 2\alpha_{z\theta}\Delta T\end{bmatrix}^{(k)} \tag{8.3}$$

The transformed stiffness matrix $\bar{C}^{(k)}$ in radial coordinates is obtained by multiplying the stiffness matrix by the transformation matrix as shown in Eq. 8.4.

$$\bar{C} = [T]^T [C][T] \tag{8.4}$$

The transformation matrix [*T*] is defined in Eq. 8.5, where *m* is the cosine of the fiber angle of ply *k*, and *n* is the sine of the fiber angle.

$$[T] = \begin{bmatrix} m^2 & n^2 & 0 & 0 & 0 & mn\\ n^2 & m^2 & 0 & 0 & 0 & -mn\\ 0 & 0 & 1 & 0 & 0 & 0\\ 0 & 0 & 0 & m & -n & 0\\ 0 & 0 & 0 & n & m & 0\\ -2mn & 2mn & 0 & 0 & 0 & m^2 - n^2\end{bmatrix} \tag{8.5}$$

Under axisymmetric loading conditions, strain is independent of *θ*, and the strain-displacement relationships can be written as described in Eq. 8.6 [65] [59].

$$\varepsilon_r^{(k)} = \frac{du_r^{(k)}}{dr}$$

$$\varepsilon_\theta^{(k)} = \frac{u_r^{(k)}}{r}$$

$$\varepsilon_r^{(k)} = \frac{du_z^{(k)}}{dr} = \varepsilon_0$$

$$\gamma_{zr}^{(k)} = 0 \tag{8.6}$$

$$\gamma_{\theta r}^{(k)} = \frac{du_\theta^{(k)}}{dr} - \frac{u_\theta^{(k)}}{r}$$

$$\gamma_{z\theta}^{(k)} = \frac{du_\theta^{(k)}}{dr} = \gamma_0 r$$

The term ε_0 is the constant axial strain experienced by all layers, and γ_0 is the twist of pipe per unit length. The radial deformation u_r can found by solving the second order differential equation in Eq. 8.7 [66].

$$\frac{d^2u_r^{(k)}}{dr^2} + \frac{1}{r}\frac{du_r^{(k)}}{dr} - \frac{\bar{C}_{22}^{(k)}/\bar{C}_{33}^{(k)}}{r^2}u_r^{(k)} = \frac{\bar{C}_{12}^{(k)} - \bar{C}_{13}^{(k)}}{\bar{C}_{33}^{(k)}}\frac{\varepsilon_0}{r} + \frac{\bar{C}_{26}^{(k)} - 2\bar{C}_{36}^{(k)}}{\bar{C}_{33}^{(k)}}\gamma_0 + \frac{\xi_r^{(k)}}{\bar{C}_{33}^{(k)}}\frac{\partial T}{\partial r} + \frac{\lambda^{(k)}\Delta T}{r} \tag{8.7}$$

For an isotropic ply, the solution for u_r is given in Eq. 8.8.

$$u_r^{(k)} = D^{(k)}r + \frac{E^{(k)}}{r} + \left(\left(\frac{\lambda^{(k)}\ln r}{2} - \frac{\lambda^{(k)}}{4}\right)(A - T_\infty) + \frac{\xi_r^{(k)}}{4\bar{C}_{33}^{(k)}}(2A + 2B\ln r - B) + \frac{\lambda^{(k)}B}{4}\left((\ln r)^2 - \ln r + \frac{1}{2}\right)\right)r \tag{8.8}$$

Where the term λ is given by Eq. 8.9.

$$\lambda^{(k)} = \frac{\xi_r^{(k)} - \xi_\theta^{(k)}}{\bar{C}_{33}^{(k)}} \tag{8.9}$$

For an orthotropic ply, the solution for u_r is given in Eq. 8.10.

$$u_r^{(k)} = D^{(k)}r^{\beta^{(k)}} + E^{(k)}r^{-\beta^{(k)}} + \alpha_1^{(k)}\varepsilon_0 r + \alpha_2^{(k)}\gamma_0 r^2 + \left(\eta^{(k)}(A - T_\infty) + \frac{\frac{B\xi_r^{(k)}}{\bar{C}_{33}^{(k)}} - 2\eta^{(k)}B}{1 - \beta^{(k)2}} + \eta^{(k)}B\ln r\right)r \tag{8.10}$$

The terms *α₁, α₂, β, and η* can be expressed are calculated from the transformed stiffness coefficients of the ply as shown in Eq. 8.11.

$$\alpha_1^{(k)} = \frac{\bar{C}_{12}^{(k)} - \bar{C}_{13}^{(k)}}{\bar{C}_{33}^{(k)} - \bar{C}_{22}^{(k)}}$$

$$\alpha_2^{(k)} = \frac{\bar{C}_{26}^{(k)} - 2\bar{C}_{36}^{(k)}}{4\bar{C}_{33}^{(k)} - \bar{C}_{22}^{(k)}}$$

$$\beta^{(k)} = \sqrt{\frac{\bar{C}_{22}^{(k)}}{\bar{C}_{33}^{(k)}}} \tag{8.11}$$

$$\eta^{(k)} = \frac{\lambda^{(k)}}{1 - \beta^{(k)2}}$$

For an example with an internal pressure P_0 and no external pressure, the boundary conditions needed to solve this problem are given in Eq. 8.12. This can be modified to include external pressure as well.

$$\sigma_r^{(1)}(r_1) = -P_0 \qquad \sigma_r^{(N)}(r_{N+1}) = 0 \tag{8.12}$$

Assuming perfect bonding between layers, interface continuities used in the solution are given in Eq. 8.13.

$$\sigma_r^{(k)}(r_k) = \sigma_r^{(k+1)}(r_k) \qquad u_r^{(k)}(r_k) = u_r^{(k+1)}(r_k) \tag{8.13}$$

Lastly, the axial tension and torque integrals under internal pressure, axial force *F* and moment *M* are given in Eq. 8.14.

$$2\pi \sum_{k=1}^{N} \int_{r_k}^{r_{k+1}} \sigma_z^{(k)}(r) r dr = \pi r_0^2 P_0 + F$$

$$(8.14)$$

$$2\pi \sum_{k=1}^{N} \int_{r_k}^{r_{k+1}} \tau_{z\theta}^{(k)}(r) r^2 dr = M$$

Once the unknown parameters are determined, the strains and stresses at each ply can be calculated. The solution for the strain equations is described in Appendix 1. After the strain matrix has been determined, the stress matrix can be calculated using Eq. 8.3.

8.2.2 Failure Criteria

As stated in Section 4, the model is able to handle three different types of failure criteria: maximum stress, Tsai-Hill, and Tsai-Wu. These criteria will be briefly introduced in this section.

The maximum stress criterion states that an object – in this case a ply – will fail when the stress in any direction exceeds the strength of the ply in that direction. More specifically, the stresses and strengths compared are:

- Compressive in direction 1
- Tensile in direction 1
- Compressive in direction 2
- Tensile in direction 2
- Compressive in direction 3
- Tensile in direction 3
- Shear in direction 1,2
- Shear in direction 1,3
- Shear in direction 2,3

The Tsai-Hill Criterion (Eq. 8.16) states that failure may occur from a combined effect of longitudinal tensile stress and shear stress, even if neither of these stresses alone exceed their respective strengths. This is evaluated using a factor "f" which indicates failure when $f \geq 1$.

$$f = \frac{{\sigma_1}^2}{{X_T}^2} + \frac{(\tau_{12}+\tau_{13})^2}{{X_{12}}^2} \tag{8.16}$$

The Tsai-Wu Criterion (8.17) expands on the Tsai-Hill criterion to include all six stress and strength elements.

$$f = \sigma_1\left[\frac{1}{X_T} - \frac{1}{X_C}\right] + \sigma_2\left[\frac{1}{Y_T} - \frac{1}{Y_C}\right] + \sigma_3\left[\frac{1}{Z_T} - \frac{1}{Z_C}\right] + \frac{{\sigma_1}^2}{X_T X_C} + \frac{{\sigma_2}^2}{Y_T Y_C} + \frac{{\sigma_3}^2}{Z_T Z_C} + \frac{{\tau_{12}}^2}{{X_{12}}^2} + \frac{{\tau_{13}}^2}{{X_{13}}^2} + \frac{{\tau_{23}}^2}{{X_{23}}^2} - \cdots \quad (8.17)$$

$$\cdots - \frac{\sigma_1\sigma_2}{\sqrt{\left[\frac{1}{X_T}-\frac{1}{X_C}\right]\left[\frac{1}{Y_T}-\frac{1}{Y_C}\right]}} - \frac{\sigma_1\sigma_3}{\sqrt{\left[\frac{1}{X_T}-\frac{1}{X_C}\right]\left[\frac{1}{Z_T}-\frac{1}{Z_C}\right]}} - \frac{\sigma_2\sigma_3}{\sqrt{\left[\frac{1}{Y_T}-\frac{1}{Y_C}\right]\left[\frac{1}{Z_T}-\frac{1}{Z_C}\right]}}$$

8.2.3 Progressive Failure

The methods above describe how the failure of a single ply can be determined. In a laminate, however, performance under the design loads can be maintained even after the failure of one or more of these plies. This model assumes laminate failure occurs when all plies have failed, and that until this point, the combination of undamaged plies and damaged plies with reduced performance will continue to support the applied loads. Therefore, a progressive failure approach is used to update the properties of the failed plies so that they will contribute less to the mechanical performance in future time steps. To accomplish this, a "failure factor" is multiplied by the longitudinal, transverse, and shear stiffness of the laminate for each time step the ply is considered to be in the "failed" state.

The failure factor, D_1, is a time-dependent value between 1 and 0. For a ply that has not failed, ρ_F is equal to 1, and it decreases according to Eq. 8.18 (longitudinal stiffness damage, D_1) or 8.19 (transverse or shear stiffness damage, D_2 and D_6). D_6 uses the same formula as D_2, but due to the random variable generated by this method, the two parameters may not be equal.

$$D_1(t) = D_1(t - \Delta t) + \big(1 - rand.lognorm(mean = -4.402, std = 1.523)\big) * \big(e^{-0.01t} - e^{-0.01(t-\Delta t)}\big) \quad (8.18)$$

$$D_2(t) = D_2(t - \Delta t) + \big(1 - rand.lognorm(mean = -2.905, std = 1.034)\big) * \big(e^{-0.01t} - e^{-0.01(t-\Delta t)}\big) \quad (8.19)$$

where $rand.lognorm()$ is a lognormally distributed random variable with the log-mean and standard deviation specified. The mean and standard deviation are obtained from the ranges for

D_1, D_2, and D_6 determined by Tan and Perez (1993) [67]. The ranges for these parameters are shown in Table 8.1.

Table 8.1. Ranges for damage variables (Tan and Perez)

Variable	Range
D_1	0.001-0.15
D_2	0.01-0.30
D_6	0.01-0.30

Figure 8.2 shows one outcome for the change in D_1, D_2, and D_6 over 1000 hours after a ply failure.

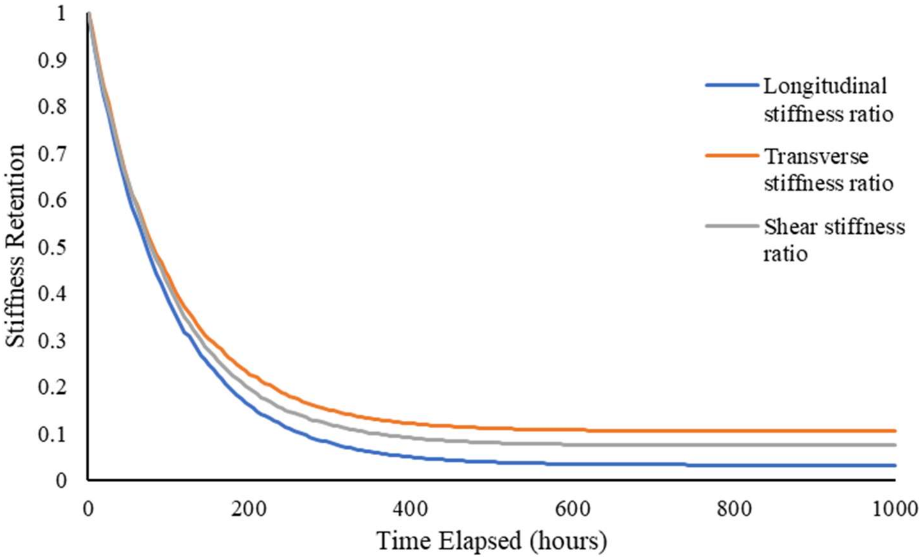

Figure 8.2. Reduction in stiffness after ply failure

8.3 Thermomechanical results

In this section, the performance of the model used by this work will be compared against other thermomechanical models and experimental failure data. Since the basic thermomechanical formulation is very similar to those of other models, it is expected that the model agreement for exact mechanical property inputs will have very good agreement. The primary aim of these tests, then, is to determine if the range of material property inputs used and the methods used to sample them provide good results.

The first case is to a stochastic model and experimental data from Wang et al. (2021) [57] who predicted the failure pressure of HDPE-glass composite pipe under combinations of axial loading and external pressure.

The pipes tested for this case had an inner radius of 24mm, a 4mm thick liner and 2mm thick cover, and four to eight 0.25mm reinforcement plies with ±55 unidirectional fibers. A fiber volume fraction of 0.4 was observed in the experimental samples.

A future modification to the thermomechanical model will enable the entry of external pressure, but for the time being the results of an internal pressure test are compared for this model. The results of the experimental test and the model by Wang et al are shown in Table 8.2.

Table 8.2. Comparison of Average Failure Pressure from Stochastic Progressive Failure Model by Wang et al. versus Experimental Data

# Plies	***Experimental Data*** *Failure Pressure*	***Wang et al. Model*** *Failure Pressure (average)*
4	25.2 MPa	21.8 MPa
6	35.3 MPa	31.5 MPa
8	45.1 MPa	40.9 MPa

The effect of ply number on failure pressure from this model is shown in Figure 8.3. For this simulation, the pipe was in a dry environment at a low temperature to minimize the effects of degradation on the mechanical performance, and 100 samples were run for each case to reduce the impact of random sample bias.

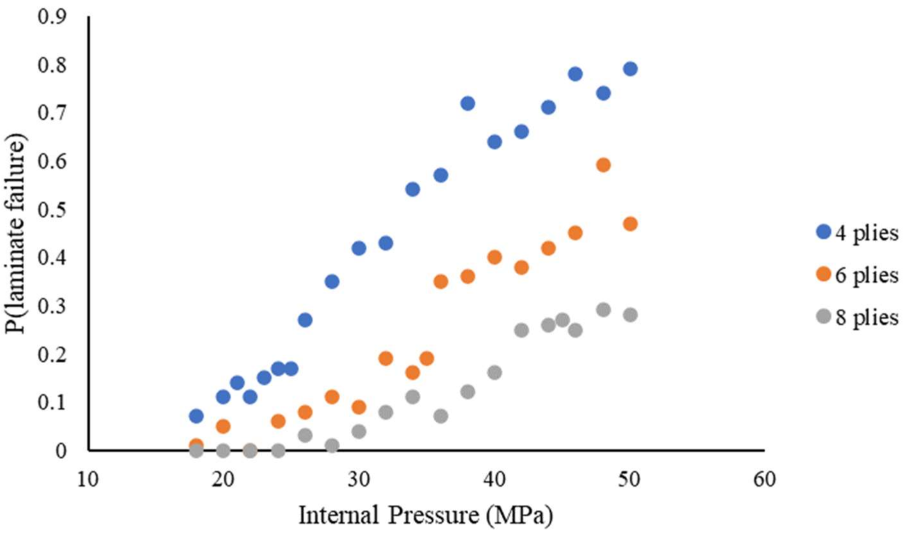

Figure 8.3. Laminate failure pressure as a function of ply number

The next model test compared to experimental data gathered by Arhant et al. (2015) [42], who tested the implosion pressure of a PA-carbon composite pipe after aging in water. The pipe from the experimental data had a diameter of 120 mm, a liner and cover each 2 mm thick, and twenty four 0.25 mm plies at 0/90° angles.

A failure pressure of 200 bar (20 MPa) was observed in the experimental result, but failure probabilities in this model remained at 0% until roughly 50 MPa, where only 3% failure probability was observed. This could be due to in part to the differences between internal and external pressure loading, but could also be due to the underestimation of the material performance, shown in Table 7.4.

8.4 Summary

In this chapter, the model used for estimating the axial and shear stresses at each ply was described. This work uses an axisymmetric thermomechanical model presented by Herakovich [65] and modified by Bakaiyan et al. [59]. The resulting stresses are evaluated against a failure criterion for individual ply failure, and a progressive failure model is used which reduces the stiffness of the failed plies over time, reducing the performance of the laminate and increasing the stress on the undamaged plies. Laminate failure is defined in this work to occur when all plies have failed.

9 Combined behavior for hypothetical pipeline

9.1 Introduction

Currently, there is no data set which provides quantitative results for the combination of all of the modeled factors, so the individual model components were verified individually against different sets of data.

To observe the performance of the entire model under a variety of conditions, however, some tests were performed using reasonable input conditions to determine if the overall behavior matches the expected performance.

9.2 Effect of Different Load combinations

In this section, the effect of varying loading conditions on the failure rate of a PA-Carbon composite pipe transporting oil while buried in slightly damp soil 0.2m below surface level is simulated over ten years. The inputs used for this simulation are shown in Table 9.1.

Table 9.1. Inputs for Simulation 1

Parameter Name	***Value***	***Unit***
Number of samples	100	
Simulation time	87600	hours
Time step (hours)	24	hours
Start timestamp	1/1/2023 10:00am	Date
Region	Los Angeles	
Pipe segment length	1.0	meters
Internal Temperature mean	313.15	Kelvin
Internal Temperature standard deviation	0.1	
External Temperature (if constant)	-1	Kelvin
Diffusion method	1	
Polymer D_0 (water)	27.2	mm^2/hour
Polymer D_0 (oil)	0.062	mm^2/hour
Composite D_0 (water)	27.2	mm^2/hour
Composite D_0 (oil)	0.062	mm^2/hour
Diffusion activation energy	4.6E-20	J/mol
Polymer water saturation at 80°C	0.1	
Composite water saturation at 80°C	0.1	
Polymer oil saturation at 80°C	0.07	
Composite oil saturation at 80°C	0.07	
Void Fraction	0.005	
Pipe depth	0.2	meters
Outer cover thickness	3	mm
Inner liner thickness	3	mm
Reinforcement ply thickness	1	mm
Number of reinforcement plies	9	
Innermost radius	30	mm
External water concentration	0.05	
Internal water concentration	0.01	
External oil concentration	0	
Internal oil concentration	0.99	
Matrix material	PA	
Fiber material	Carbon	
Fiber volume fraction	0.6	
Fiber angles	[0,-55,55,-55,55,-55,55,-55,55,-55,0]	degrees
Internal pressure	10	MPa
Axial Force	0	MPa
Axial Moment	0	N*m
Failure Criteria	MAX_STRESS	

The fluid absorption results over 10 years are shown in Figure 9.1. It was observed that for this material, while water has a higher diffusivity coefficient and saturation concentration than oil, little water was absorbed overall, due to the low concentration of water on the pipe's exterior.

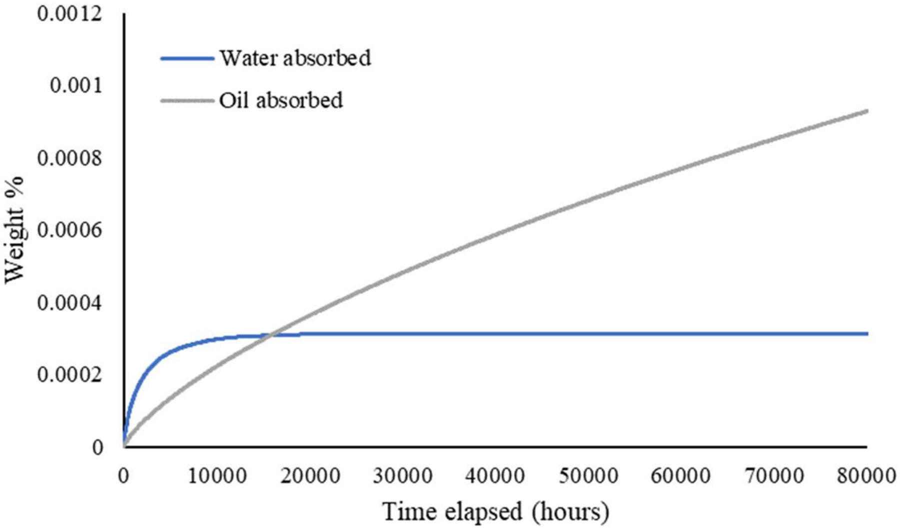

Figure 9.1. Fluid absorption of water and oil simulated for a buried pipe over 10 years

Stiffness retention in the longitudinal, transverse, and shear (23) directions over the first 15,000 hours are shown in Figure 9.2. After about 12,000 hours, the stiffness reduction for all three directions flattened out at about 20%. The reason for this is due to the failure of individual plies which are counted for each sample and reported at the simulation end time in Figure 9.3. As described by the progressive failure modeling methods in Chapter 8, the stiffness of the failed plies will gradually decrease over time. The relative loss of stiffness from this phenomenon is much greater than the effects of degradation due to the oil exposure and water exposure, since relatively little water was absorbed and oil has a minimal effect on the mechanical properties of PA. Therefore, once the mechanical properties have reached their asymptote for mechanical property loss due to failure, the relative loss of stiffness in all directions will also flatten out significantly.

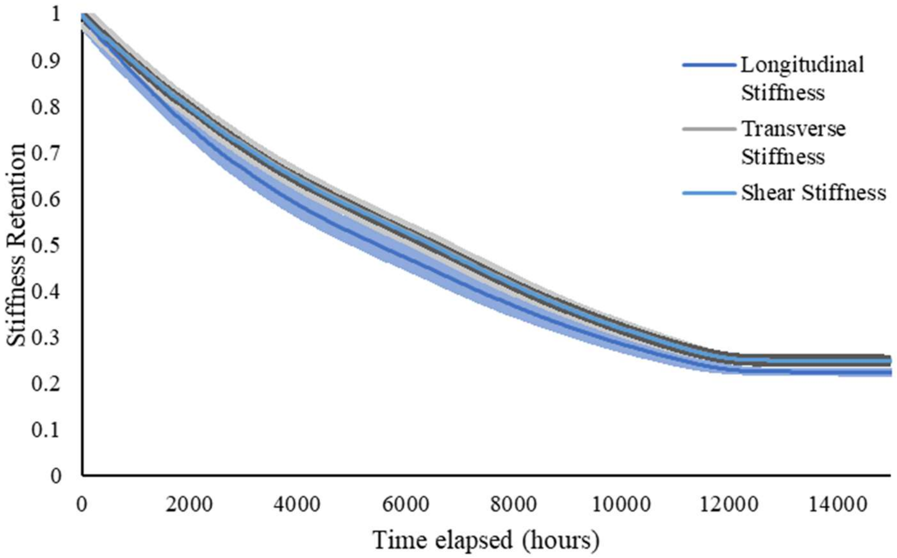

Figure 9.2. Retention of longitudinal, transverse, and shear (23) stiffness scaled to the initial average value for these parameters. The transverse and shear stiffness loss overlap making them difficult to distinguish in the plot

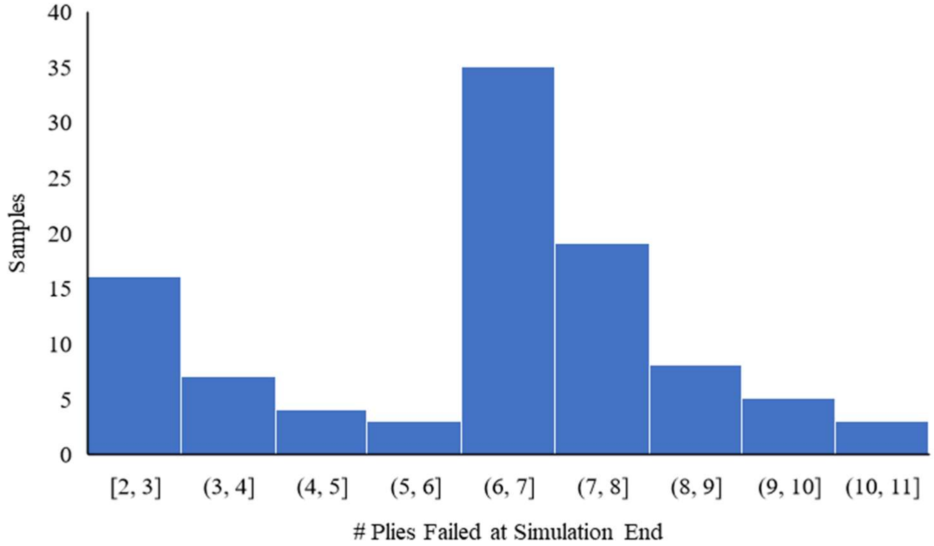

Figure 9.3. Histogram of the number of plies failed at the end of each sample's time simulation at 10 MPa

Figures 9.4 and 9.5 (zoomed in) shows the failure probability of the laminate over time. In total, 3% of samples failed during this simulation, with all of these failures occurring at roughly 11,000 hours. Due to the small number of samples that failed during this simulation, it is difficult to draw conclusions about the effects of external conditions over time on failure rates.

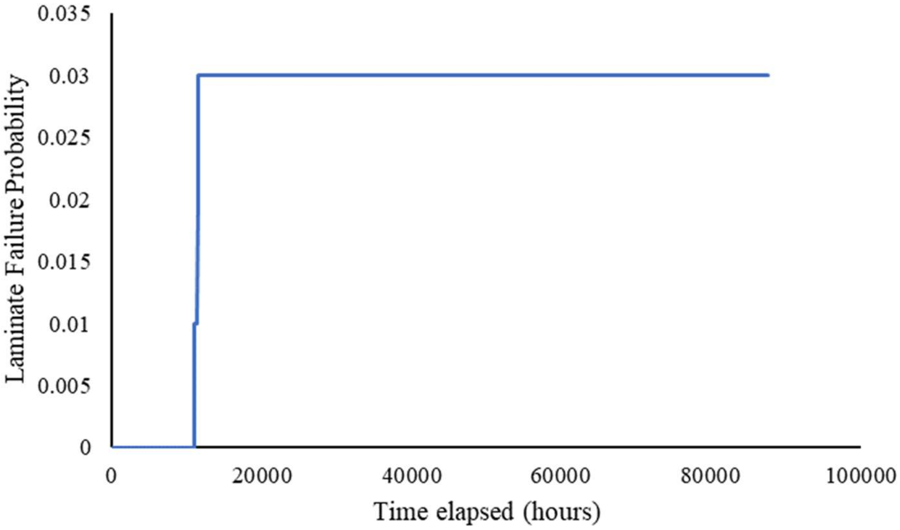

Figure 9.4. Laminate failure results over 10 years (88000 hours) at 10 MPa

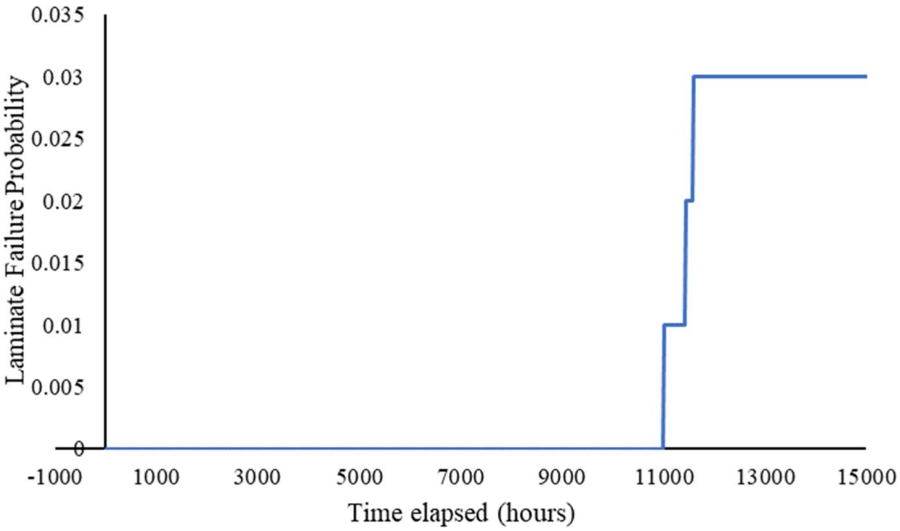

Figure 9.5. Laminate failure results from figure 9.4 zoomed in to the first 15,000 hours to show the evolution of failed samples

Next, the same simulation from above was repeated with the internal pressure increased to 15 MPa. As expected, more ply failures – shown in Figure 9.6 – were observed under the increased load.

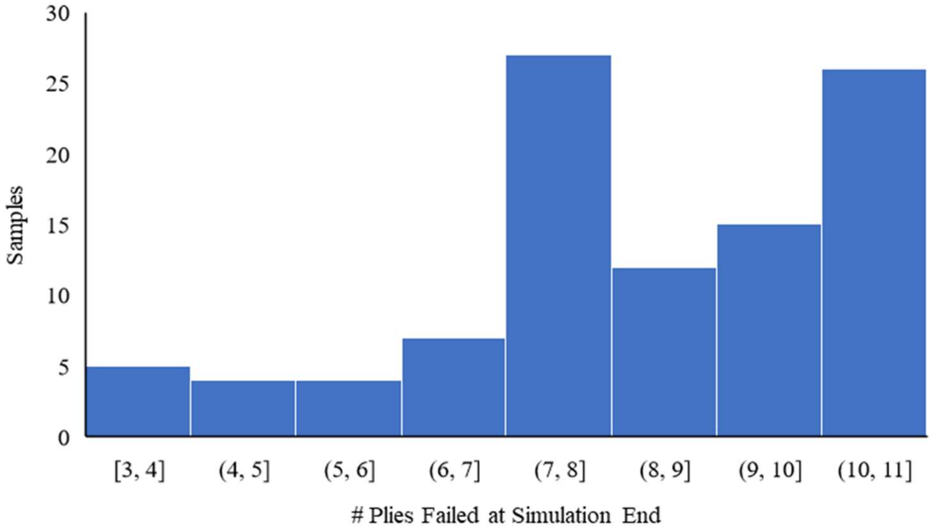

Figure 9.6. Histogram of the number of ply failures observed at the end of each sample's time simulation at 15 MPa

The degradation in stiffness resulting from the fluid absorption (same as the 10 MPa case) and ply failures is shown in Figure 9.7 with standard deviation around the average values. The averages observed are similar to that of the 10 MPa case, but a much wider standard deviation is observed for this case. This is likely due to the increased number of both ply and laminate failures.

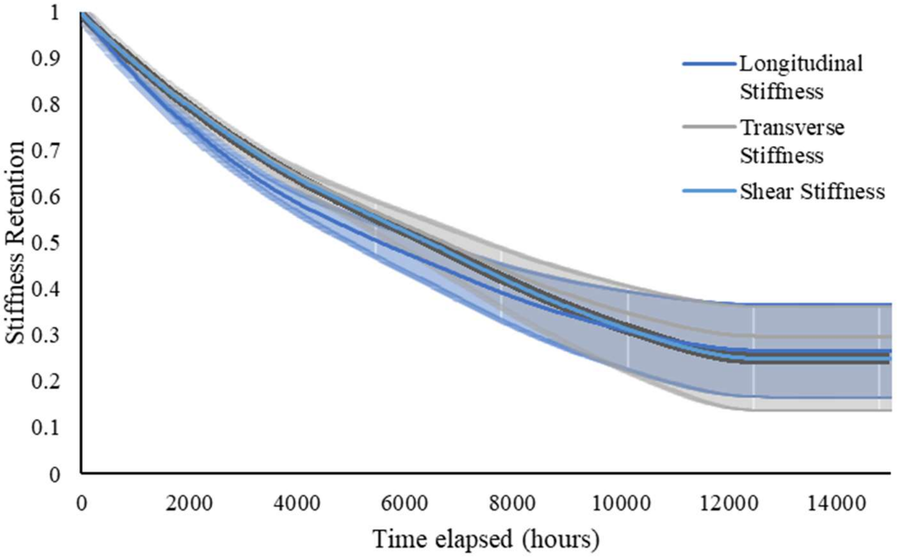

Figure 9.7. Retention of stiffness over the first 15,000 hours at 15 MPa

The laminate failures in the 15 MPa simulation are shown in Figure 9.8. As there are more failures in this case, some trends for the behavior of the laminate failure may be observed. The initial rise in failures can most likely be attributed to the degradation of the broken plies in samples that had plies fail at the very beginning of the simulation becoming low enough that the laminate can no longer support the internal pressure. Following this, the number of new laminate failures slows, likely due to: 1) the samples with early failures having already failed, and 2) the reduced external temperatures over the winter months resulting in higher matrix stiffnesses. Effect 2 is generally minimal in this simulation, though, partly because of the chosen region's relatively warm winters and partly due to the pipe being buried beneath the surface where it will not undergo as much temperature variation. Regardless, after the slowdown, there is another rise in laminate failures until just before 20,000 hours. This may be attributed at least in part to increasing external temperatures leading to more stiffness degradation, combined with laminate failure of samples that encountered first ply failures during the first 10,000 hours.

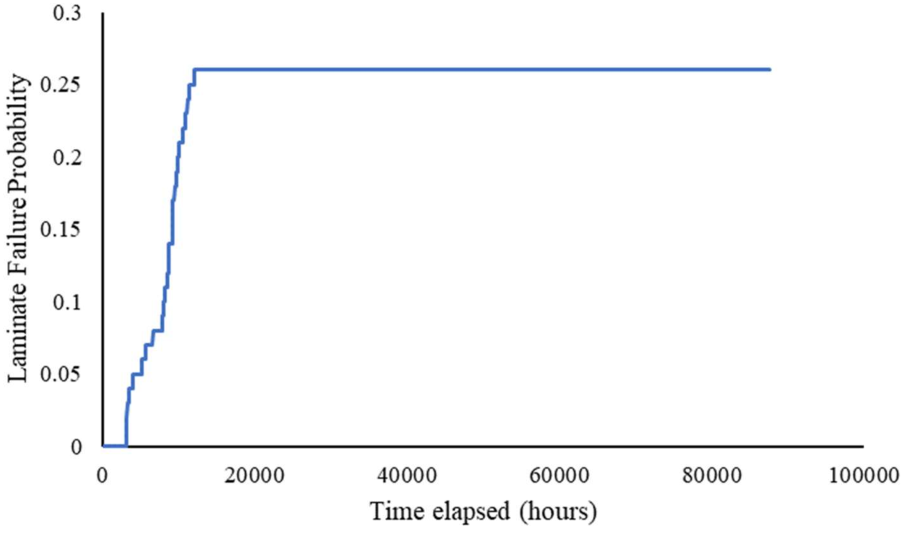

Figure 9.8. Laminate failure probability over 10 years at 15 MPa internal pressure

The next test reduced the internal pressure back to 10 MPa, but added 1 MPa of axial tension. Under these conditions, all samples failed within the first 10,000 hours, as can be seen in Figure 9.9.

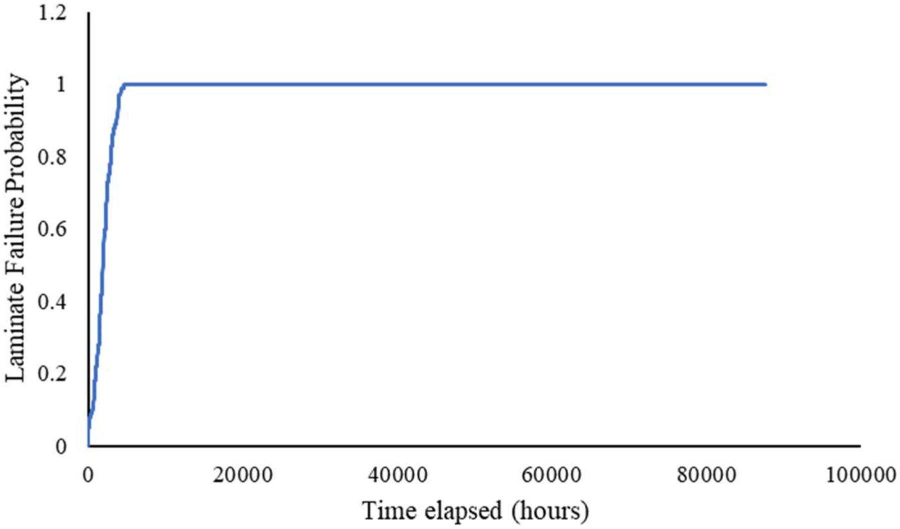

Figure 9.9. Laminate failure probability over 10 years at 10 MPa internal pressure and 1 MPa axial tension

The early failure of all samples leads to a particular phenomenon with the degradation results, seen in Figure 9.10. Here, a sharp drop is seen immediately due to several laminates failing in the first time step, followed by a gradual decrease which flattens out at about 60% of the initial strength. Using this result alone would seem to imply that less degradation is observed here, but this is somewhat misleading. The logic of the model is to stop stimulating time after all plies in the laminate have failed, which means that degradation will not continue past that point.

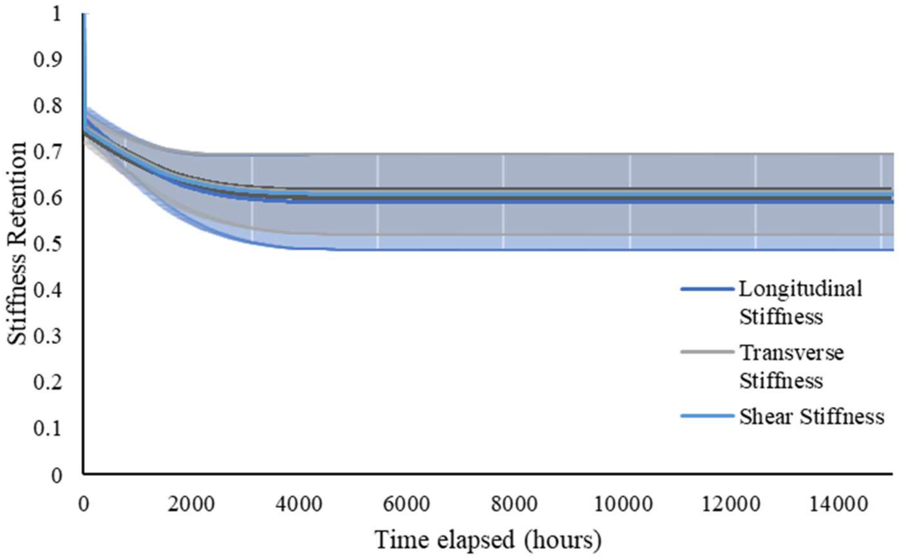

Figure 9.10. Stiffness degradation results from the 10 MPa pressure with 1 MPa tension samples, highlighting the effects of early laminate failure on the degradation model

The next simulation maintained the 10 MPa internal pressure and applied 0.5 MPa of compressive axial force. This increased the number of laminate failures, but not so much as to have all laminates fail early. The laminate failure probabilities can be seen in Figure 9.11. This simulation was run for only 15,000 hours, due to the fact that many of the past simulations stabilized after roughly that amount of time.

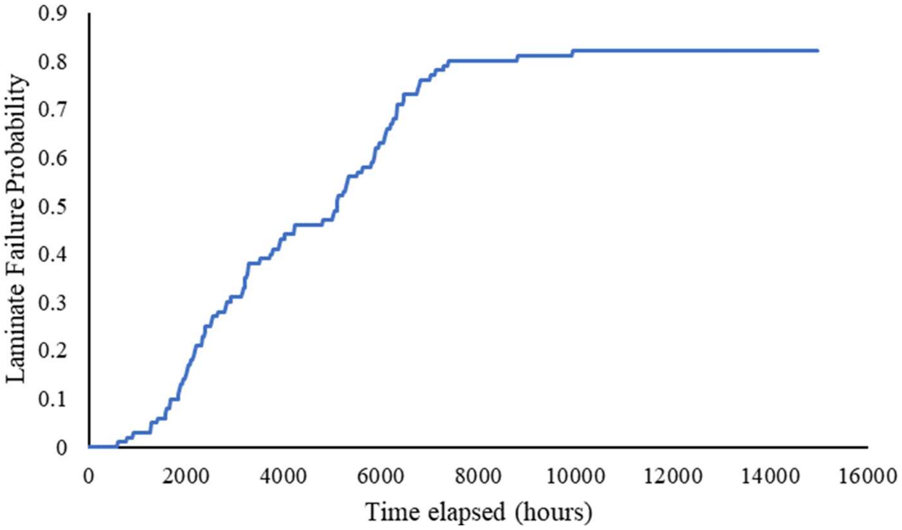

Figure 9.11. Laminate failure probability under 10 MPa internal pressure and 0.5 MPa axial compression

The stiffness degradation – shown in Figure 9.12 – appears as a mixture of the results from the first simulation and those of the simulation with 1 MPa axial tension. Enough samples survived to experience severe degradation from ply failures, while others failed early leaving the effect described for Figure 9.10. The combination of these factors results in a large standard deviation.

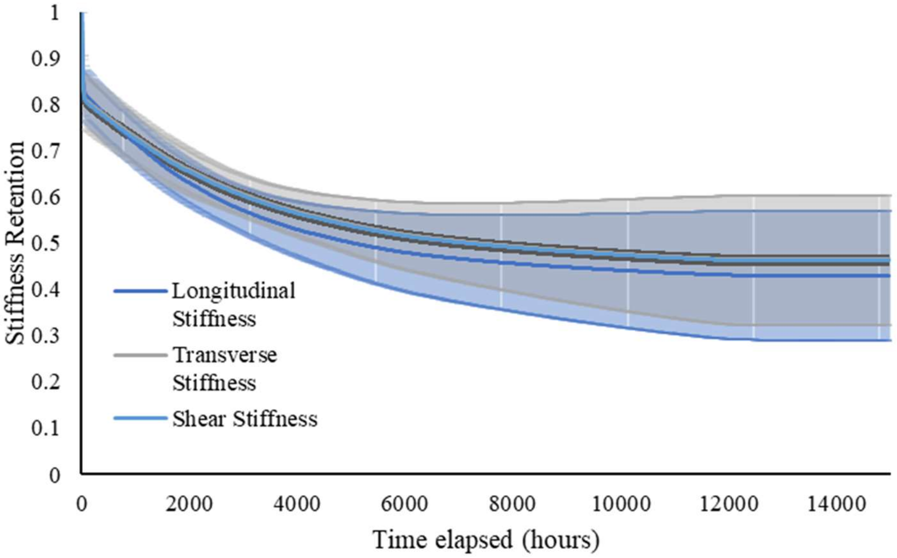

Figure 9.12. Stiffness degradation with 10 MPa internal pressure and 0.5 MPa axial compression

9.3 Effect of temperature

In this section, the effect of increasing temperature on a PP-glass composite pipe carrying an oil mixture and exposed to some water on its exterior. An internal pressure of 10 MPa was maintained for all simulations, while the internal temperature was increased from 296 K to 353 K. The inputs used for the baseline simulation are shown in Table 9.2. In each case, the exterior temperature was allowed to vary as normal.

Table 9.2. Inputs for Simulation 2

Parameter Name	***Value***	***Unit***
Number of samples	50	
Simulation time	15000	hours
Time step (hours)	24	hours
Start timestamp	1/1/2023 10:00am	Date
Region	Los Angeles	
Pipe segment length	1.0	meters
Internal Temperature mean	296.15	Kelvin
Internal Temperature standard deviation	0.1	
External Temperature (if constant)	-1	Kelvin
Diffusion method	1	
Polymer D_0 (water)	6.29	mm^2/hour
Polymer D_0 (oil)	4	mm^2/hour
Composite D_0 (water)	6.29	mm^2/hour
Composite D_0 (oil)	4	mm^2/hour
Diffusion activation energy	2.5E-20	J/mol
Polymer water saturation at 80°C	0.012	
Composite water saturation at 80°C	0.012	
Polymer oil saturation at 80°C	0.02	
Composite oil saturation at 80°C	0.02	
Void Fraction	0.005	
Pipe depth	0.2	meters
Outer cover thickness	3	mm
Inner liner thickness	3	mm
Reinforcement ply thickness	1	mm
Number of reinforcement plies	9	
Innermost radius	30	mm
External water concentration	0.05	
Internal water concentration	0.01	
External oil concentration	0	
Internal oil concentration	0.99	
Matrix material	PP	
Fiber material	Glass	
Fiber volume fraction	0.6	
Fiber angles	[0,-55,55,-55,55,-55,55,-55,55,-55,0]	degrees
Internal pressure	10	MPa
Axial Force	0	MPa
Axial Moment	0	N*m
Failure Criteria	MAX_STRESS	

At 296 K, the fluid absorption for both water and oil are slowed, and a lower saturation concentration is observed, as seen in Figure 9.13. Still, similar to the case with PA, the oil absorption is significantly higher than that of water due to the higher availability of oil for absorption.

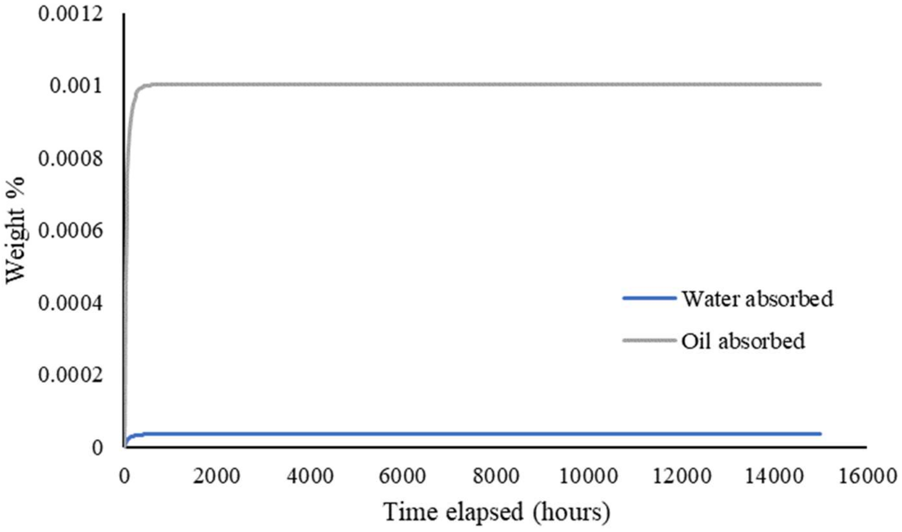

Figure 9.13. Water and oil absorption in a PP-Glass pipe at 296K

Degradation results at 296 K under 10 MPa internal pressure are shown in Figure 9.14. While a similar degree of degradation is observed long-term in the PA samples, due to the failed plies, the shape of this curve stands out from other simulations. A noticeable reduction in degradation over time is observed between about 4,000 and 7,000 hours. The reason for this is that the lower temperature of the pipe interior results in potentially worse thermal degradation coming from the outside, rather than the inside, whereas at higher temperatures the degradation caused by the interior temperature tends to dominate. The lower degradation rates during this time window can then be explained by lower outside temperatures during the late fall through early spring. Additionally, it can be noted that no laminate samples failed during this simulation, allowing for the effects of degradation in this model from both ply failures and environmental degradation to be observed independently throughout the full simulation time.

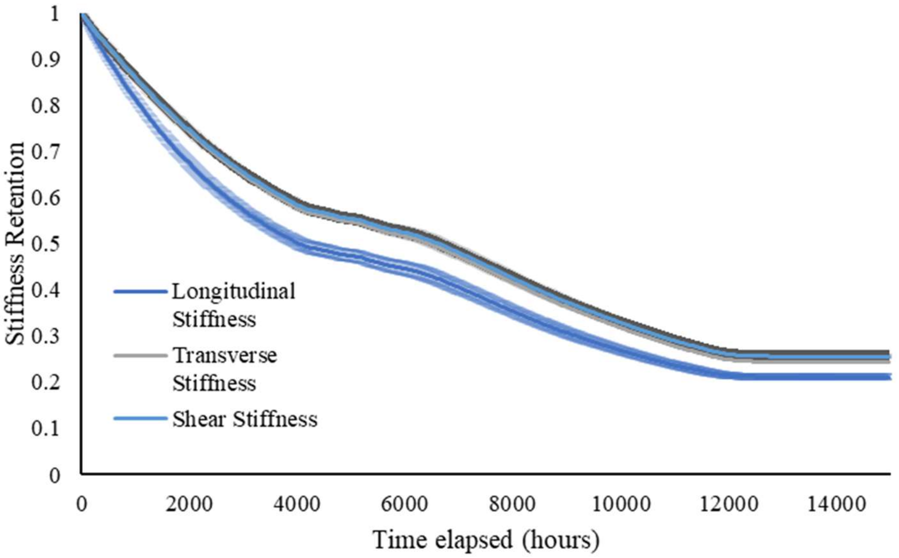

Figure 9.14. Stiffness degradation results in a PP-Glass pipe at 296 K under 10 MPa internal pressure

At 313 K, there is relatively little impact on the diffusion behavior of oil and water, shown in Figure 9.15. As observed in Section 5, the sigmoidal function currently used for determining the saturation concentration at a given temperature tends to underestimate saturation concentrations in this temperature range. Future work will improve this method to allow for better predictions of fluid absorption.

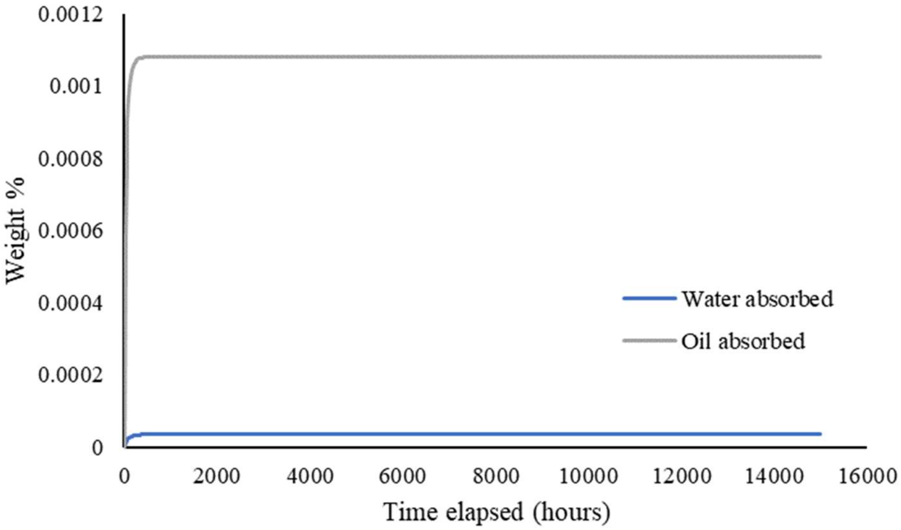

Figure 9.15. Water and oil absorption in a PP-Glass composite pipe at 313 K

The degradation of longitudinal, transverse, and shear stiffness over the simulation time at an internal temperature of 313 K and 10 MPa internal pressure are shown in Figure 9.16, with the laminate failure probability shown in Figure 9.17. The results in this case are similar to those from the first test on the PA-Carbon samples.

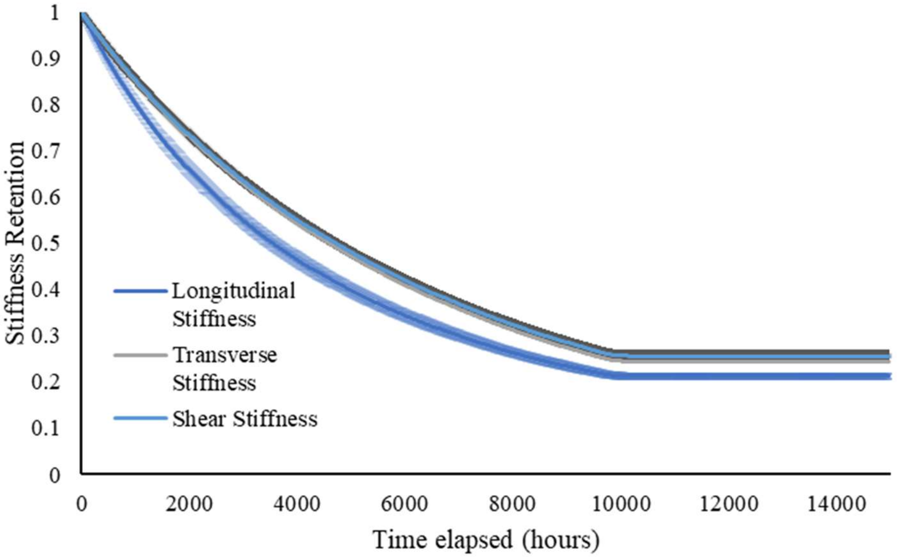

Figure 9.16. Stiffness loss at 313 K under 10 MPa internal pressure

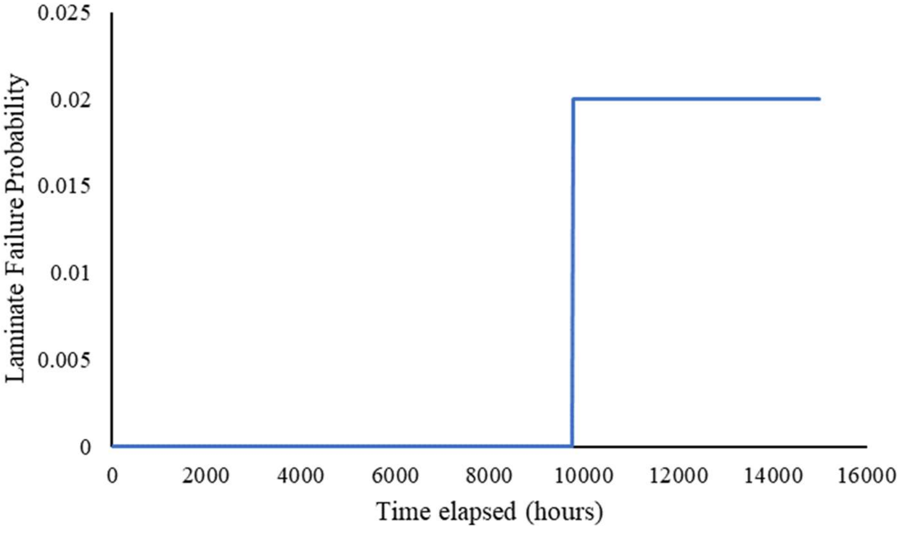

Figure 9.17. Laminate failure probability at 313 K internal temperature and 10 MPa internal pressure

At 353 K, a noticeable difference in diffusion behavior, degradation levels, and failure rates is observed. In the fluid absorption curve, shown in Figure 9.18, it can be seen that, while water absorption increases slightly, is largely controlled by the low concentration, whereas oil absorption increases roughly three-fold with time.

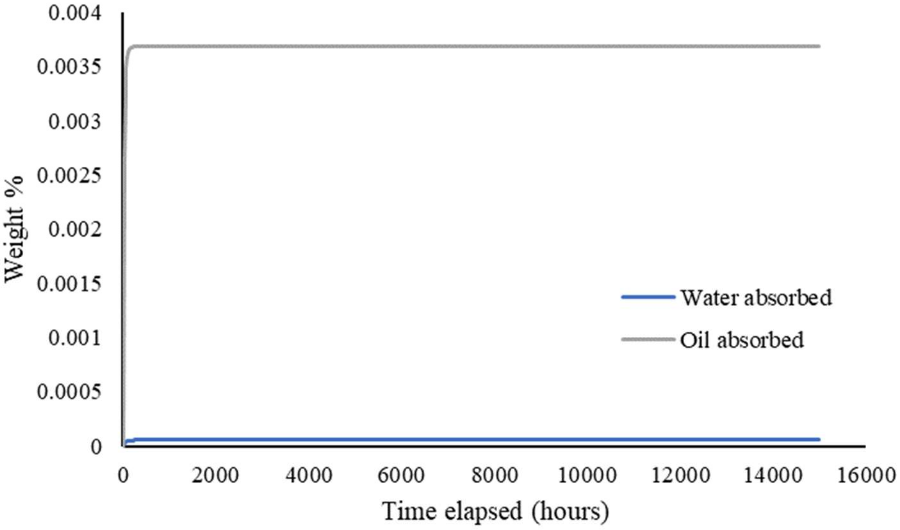

Figure 9.18. Water and oil absorption in a PP-Glass pipe at 353 K

The higher temperatures also lead to a higher degree of thermal softening and degradation, leading to more failures, as shown in Figure 9.20, and higher levels of stiffness loss, shown in Figure 9.19.

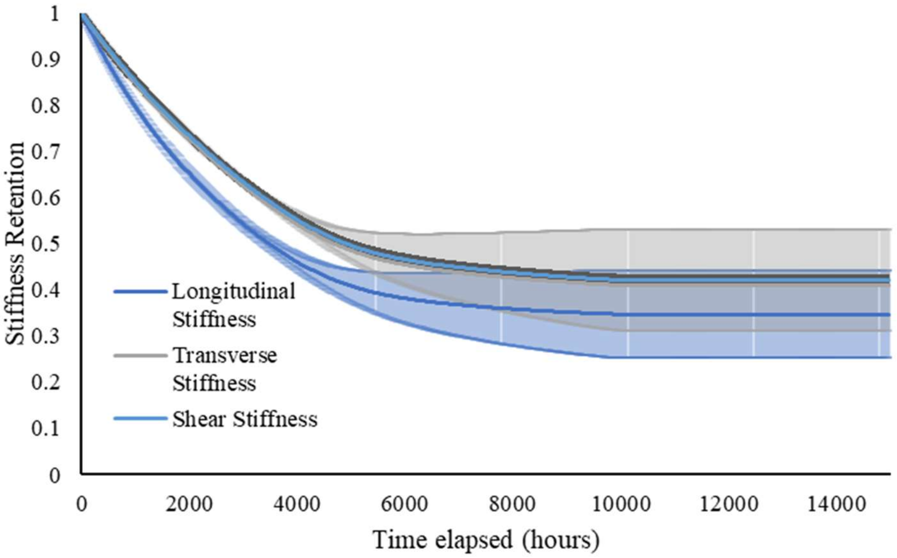

Figure 9.19. Longitudinal, Transverse, and Shear stiffness retention after 15,000 hours at 353 K

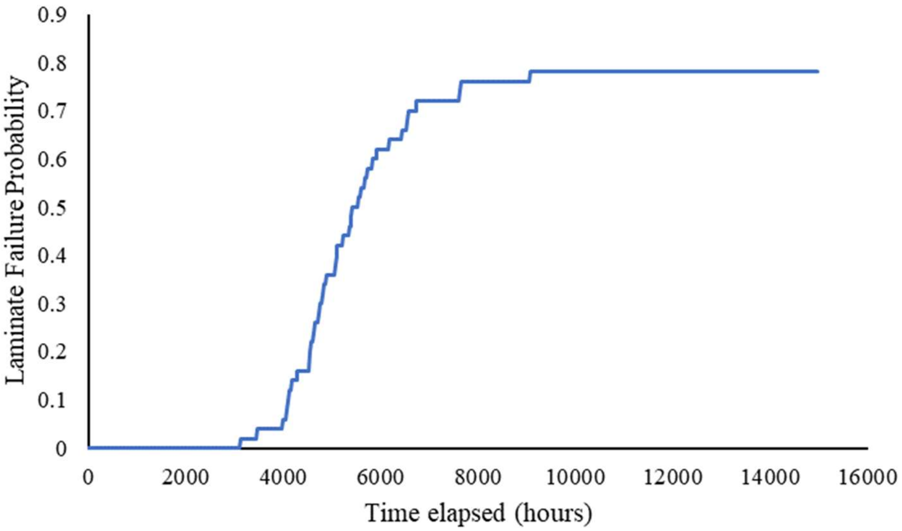

Figure 9.20. Failure probability of a PP-Glass laminate exposed to 10 MPa internal pressure and 353 K internal temperature for 15,000 hours

9.4 Summary

In this chapter, the results of full simulations considering exposure to fluids and elevated temperatures under a variety of loading conditions were presented. In many of the simulations, significant damage could be incurred to a pipe without causing laminate failure.

10 Probabilistic System Integrity Management for Non-Metallic Pipes (PSIM-NM)

10.1 Introduction

The Pipeline System Integrity Management (PSIM) software tool was initially developed in 2020 featuring the work of Wu [68] and Chalgham [69]. This tool features pipeline health monitoring, corrosion prognosis, system-level failure analysis, sensor placement optimization, and inspection/maintenance optimization for steel natural gas pipelines. This tool applies the Hybrid Causal Logic (HCL) method, composed of event sequence diagrams, fault trees, and Bayesian networks to capture the reliability of a complex system, It is implemented in an online software available at [apps.risksciences.ucla.edu/psim].

During the course of this research, a module was added to PSIM for non-metallic pipes called PSIM-NM. This module serves a similar function as the corrosion simulation by using the python code containing the modeling methods described in Chapters 4 through 8 to predict the likelihood of a pipe segment failing under a set of input conditions over time. Sensor placement optimization and inspection/maintenance optimization are not a part of this current work, but are planned to be completed in future projects.

10.2 Application

This platform allows a user to analyze the reliability of a custom pipe using real-world coordinates and estimates for environmental conditions. Future plans for this program include the ability to link metallic and non-metallic segments and provide insights into best practices for repair and sensor placement.

10.3 Implementation

Implementation of the non-metallic failure predictions into this modeling software was completed with the aid of Wadie Chalgham and Uzias Rivera in the B. John Garrick Institute for the Risk Sciences.

The module can be accessed at [apps.risksciences.ucla.edu/psim]. The homepage for PSIM-NM is shown in Figure 10.1. It contains a map and navigation links to the simulation modules, and a library of existing built pipes as well as an option to add a new pipe using the + icon.

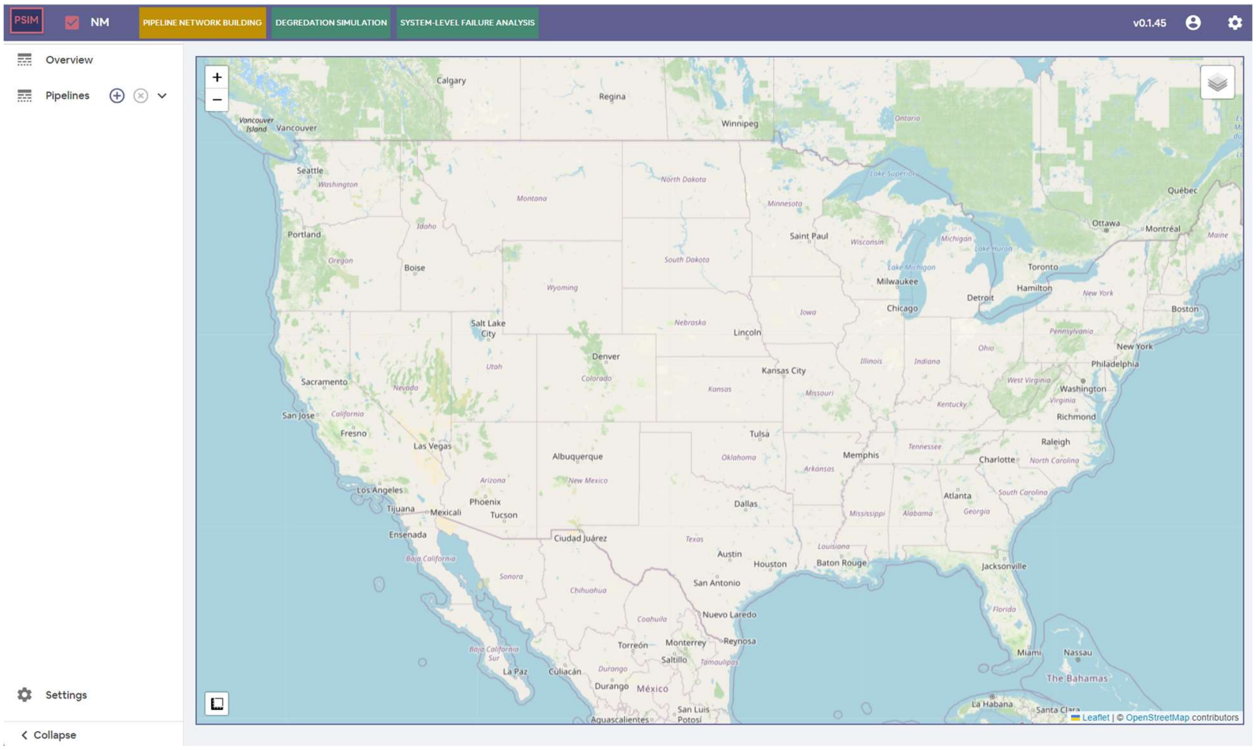

Figure 10.1 Homepage for PSIM-NM

Upon creating a new pipeline, the user is given the prompt in Figure 10.2, where they can provide the inputs described in Section 4 in the form of a CSV file, as well as a shape file which provides the coordinates of all of the pipe segments. A future update to this module will use these coordinates to automatically link the pipe to the nearest region for temperature data.

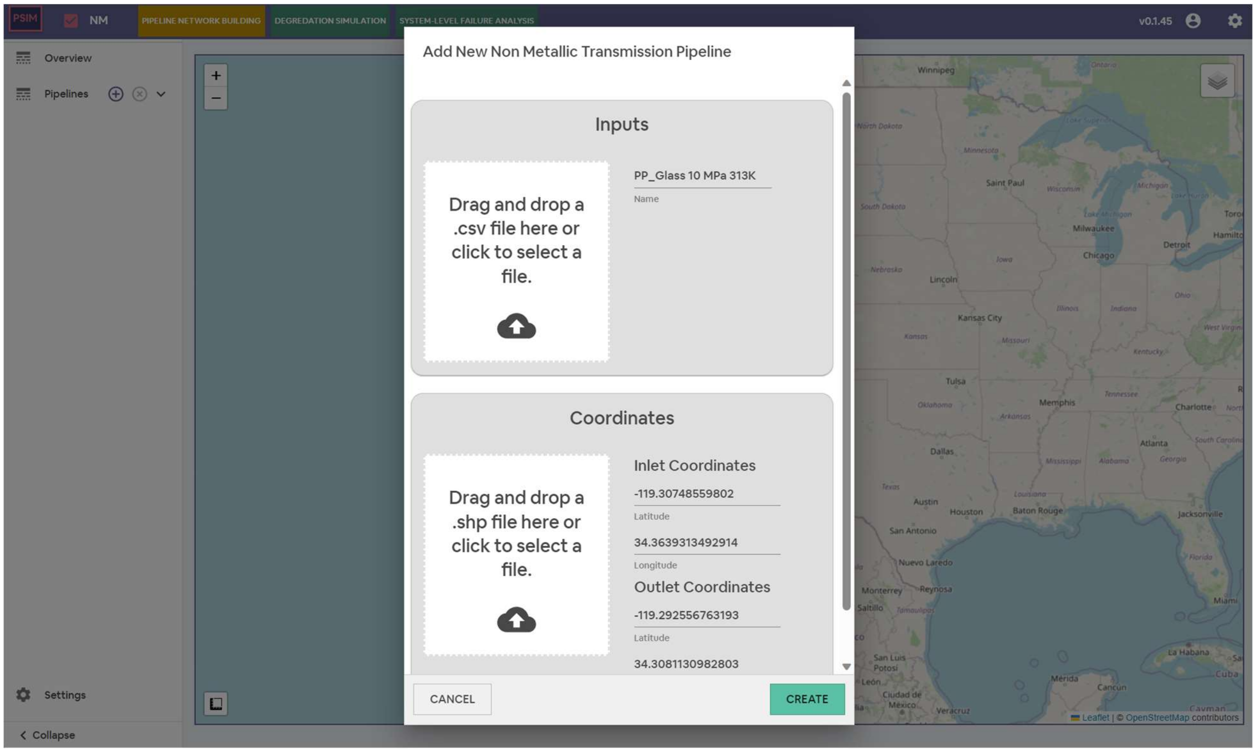

Add New Non Metallic Transmission Pipeline

Inputs

Drag and drop a .csv file here or click to select a file.

Name: PP_Glass 10 MPa 313K

Coordinates

Drag and drop a .shp file here or click to select a file.

Inlet Coordinates

Latitude: -119.30748559802

Longitude: 34.3639313492914

Outlet Coordinates

Latitude: -119.292556763193

34.3081130982803

Figure 10.2 Non-Metallic Pipe Inputs Prompt

After creating a pipe using the prompt, the map will now show the pipe created in the corresponding location as seen in Figure 10.3.

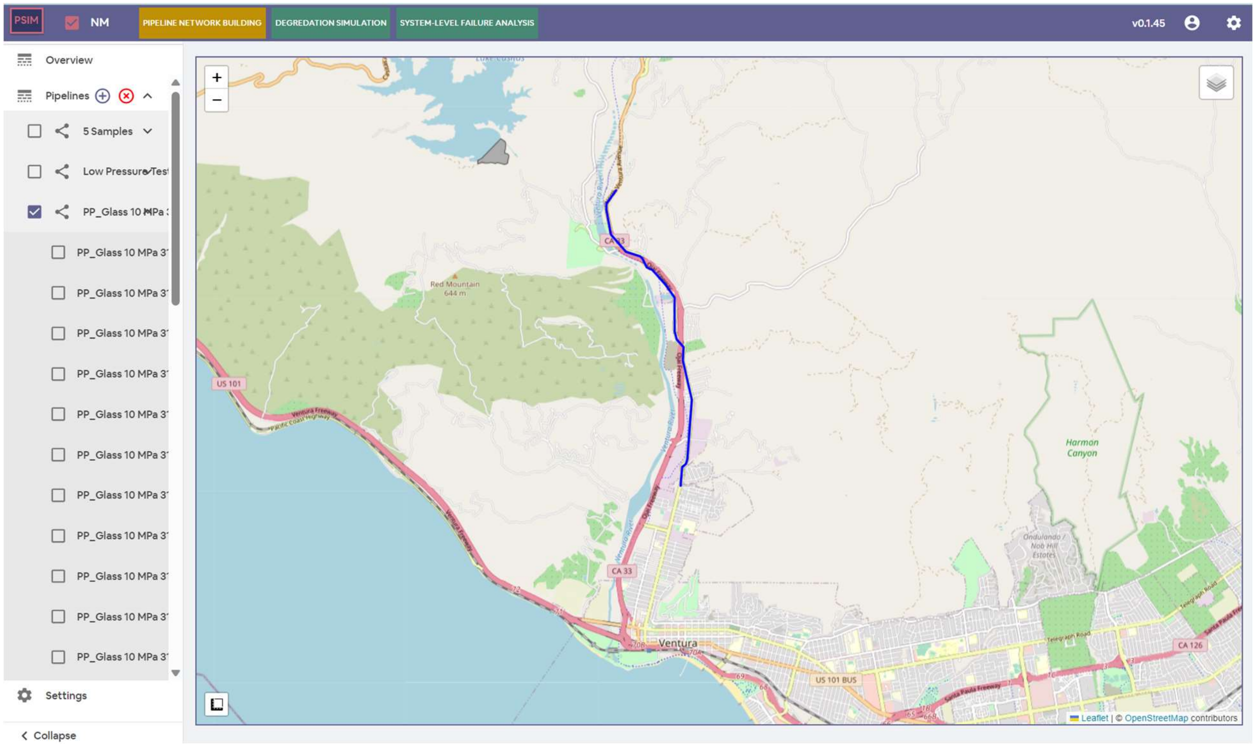

Figure 10.3. Example pipe located in the Ventura area, shown as the blue line

Next, by navigating to the "Degradation Simulation" tab, the user is able to view and edit the simulation inputs and run the simulation using the "simulate" button. Once the simulation is complete, the user is presented with five result graphs: the probability of failure over time, water absorption results, oil absorption results, stiffness results for each sample, and the average stiffness retention in each direction. The appearance of these results for a sample pipe under a low internal pressure are shown in Figures 10.4 through 10.7. In the first and last of these figures, the header shown displays the average loss of longitudinal stiffness and the probability of failure at the end of the simulation.

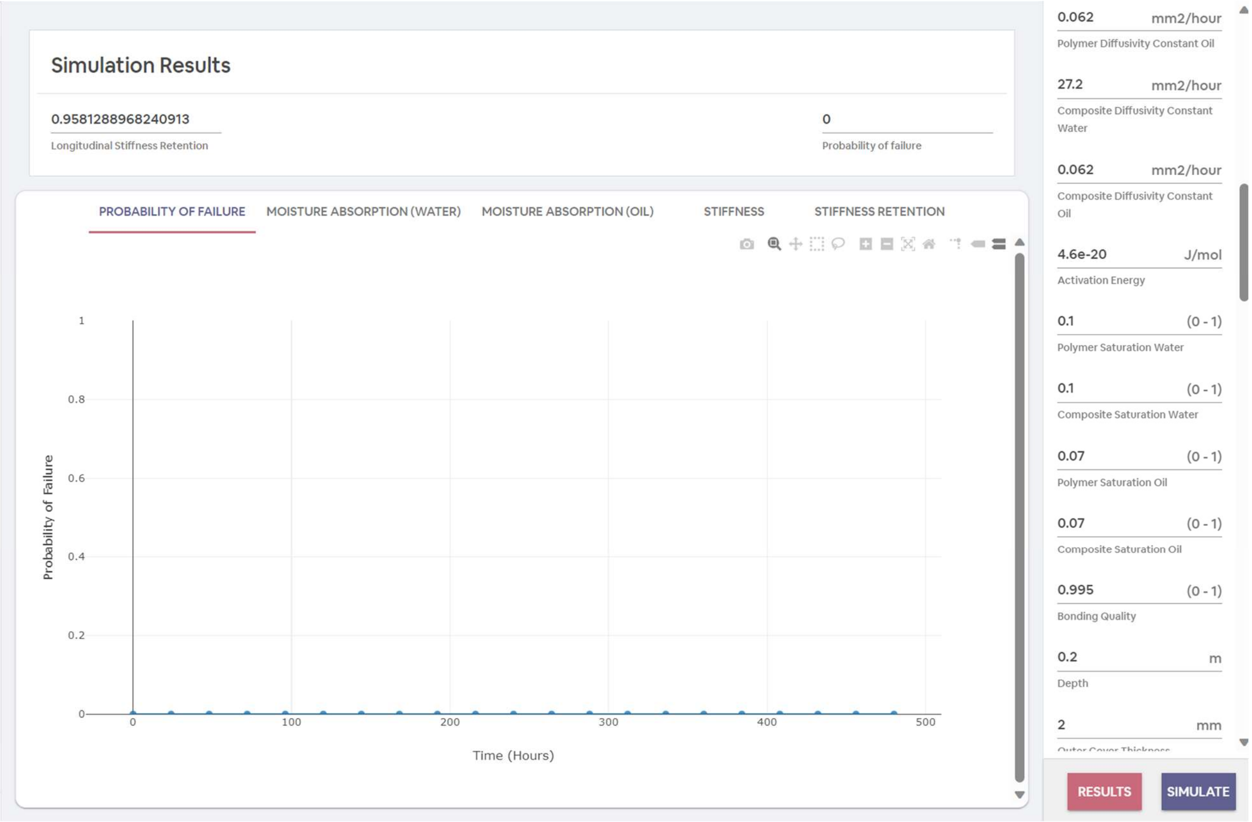

Simulation Results

0.9581288968240913
Longitudinal Stiffness Retention

0
Probability of failure

0.062 mm2/hour
Polymer Diffusivity Constant Oil

27.2 mm2/hour
Composite Diffusivity Constant Water

0.062 mm2/hour
Composite Diffusivity Constant Oil

4.6e-20 J/mol
Activation Energy

0.1 (0 - 1)
Polymer Saturation Water

0.1 (0 - 1)
Composite Saturation Water

0.07 (0 - 1)
Polymer Saturation Oil

0.07 (0 - 1)
Composite Saturation Oil

0.995 (0 - 1)
Bonding Quality

0.2 m
Depth

2 mm

Figure 10.4. Failure results for the sample pipe, plotted in a single curve against the amount of time elapsed in the simulation. In this simulation the internal pressure was low, resulting in no failures

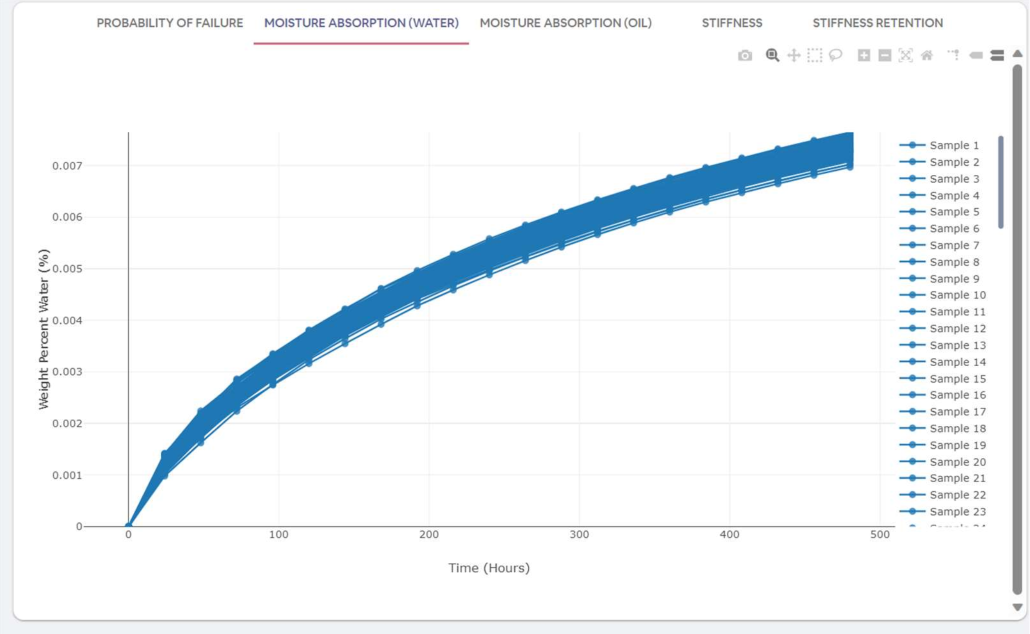

Figure 10.5. Moisture absorption results for both oil and water each sample plotted as individual lines

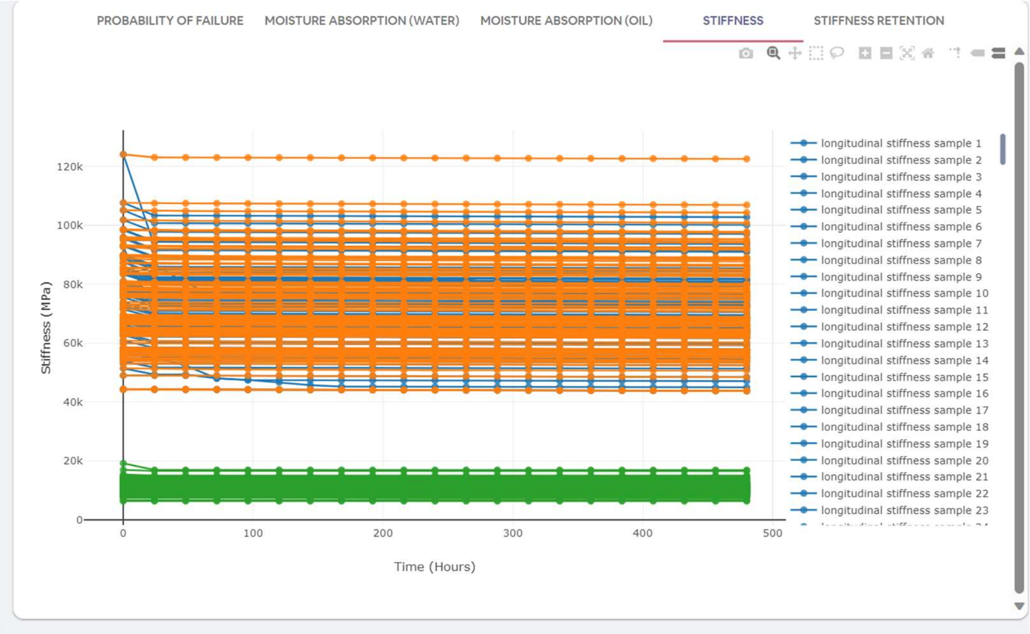

Figure 10.6. Stiffness value results for each sample in all three directions. When many samples are simulated, a large amount of data will be presented on this graph, which may make difficult to read. In this case the user can hide individual results by clicking on the name of the curve using the legend on the right.

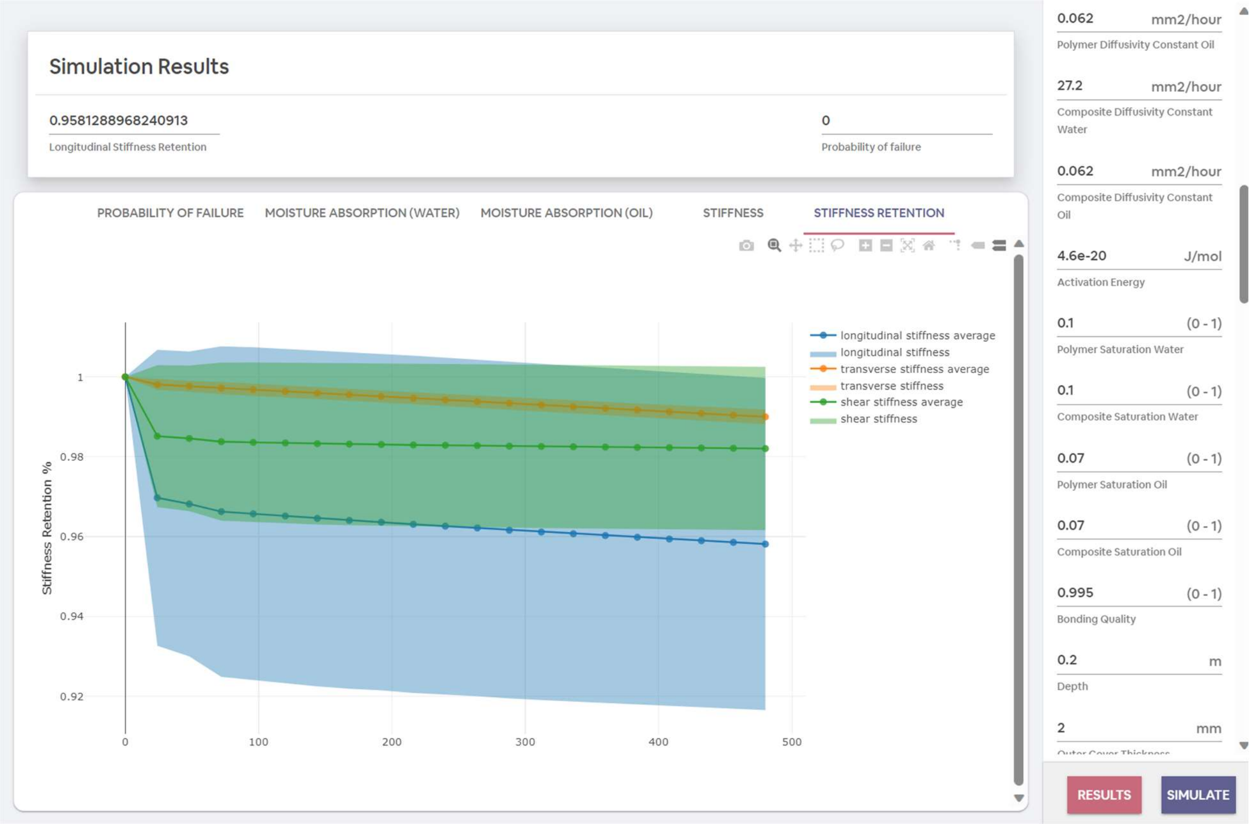

Simulation Results

0.9581288968240913
Longitudinal Stiffness Retention

0
Probability of failure

0.062 mm2/hour
Polymer Diffusivity Constant Oil

27.2 mm2/hour
Composite Diffusivity Constant Water

0.062 mm2/hour
Composite Diffusivity Constant Oil

4.6e-20 J/mol
Activation Energy

0.1 (0 - 1)
Polymer Saturation Water

0.1 (0 - 1)
Composite Saturation Water

0.07 (0 - 1)
Polymer Saturation Oil

0.07 (0 - 1)
Composite Saturation Oil

0.995 (0 - 1)
Bonding Quality

0.2 m
Depth

2 mm

Figure 10.7. The stiffness retention curve shows the scaled results for the retained longitudinal, transverse, and shear stiffness as an average (solid line) and standard deviation (semi-transparent area)

Once the laminate failure results have been simulated, they are used in a fault tree failure analysis model, which looks at the likelihood of a transmission failure over time by combining the laminate failure results with other potential causes of failure, shown in Figure 10.8.

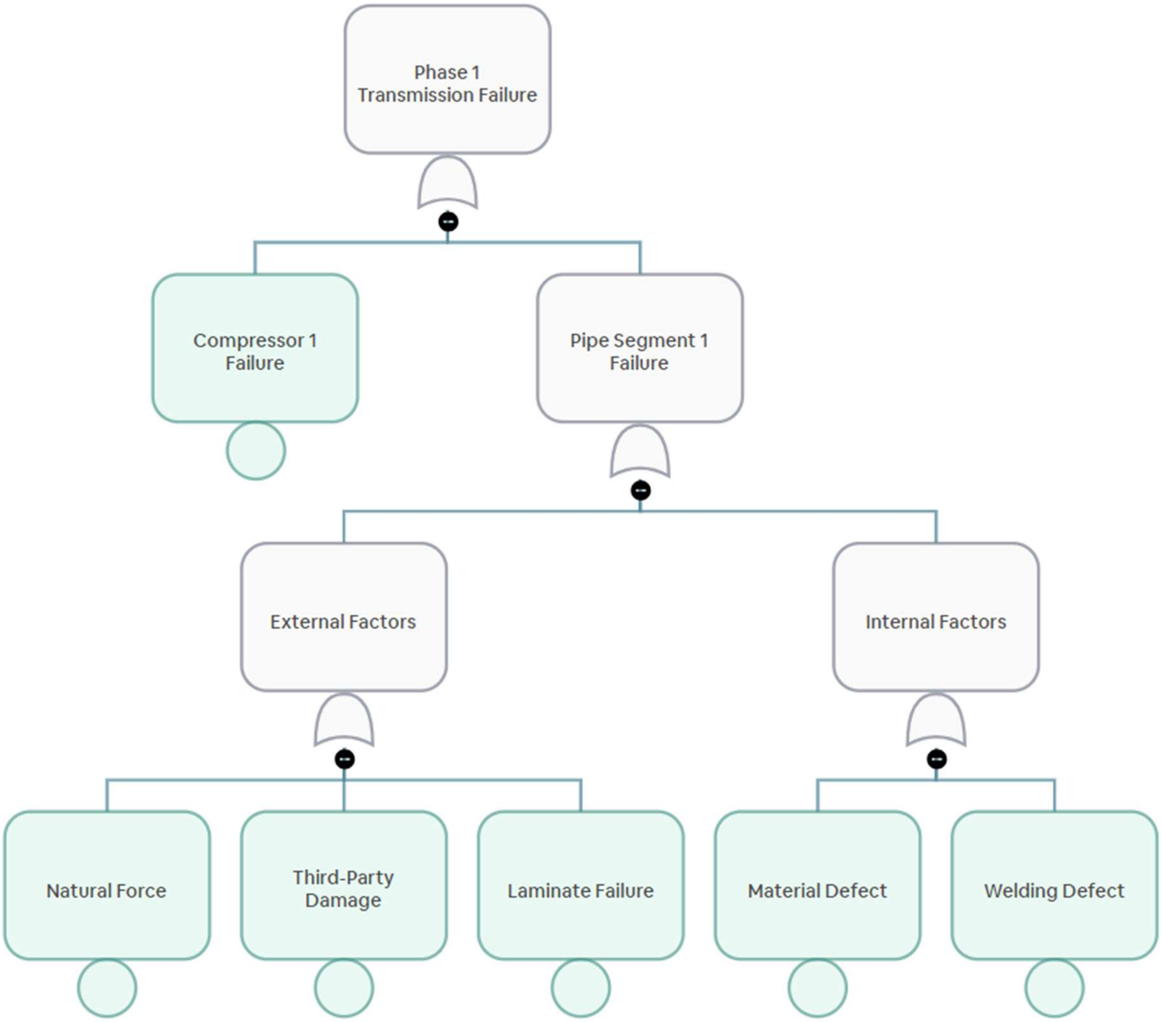

Figure 10.8. Fault tree of potential transmission phase failures including the laminate pipe and compressor. Other forms of laminate damage not based on natural degradation are included in this fault tree as well.

The properties of all nodes except for "laminate failure" were determined by research on the historical failure data on transmission pipe failures, performed by Wadie Chalgham [69], which was introduced in the original PSIM for metallic pipes.

Compressor failure is defined as a non-parametric time-dependent reliability function, shown in Figure 10.9, which behaves similarly to an exponential distribution.

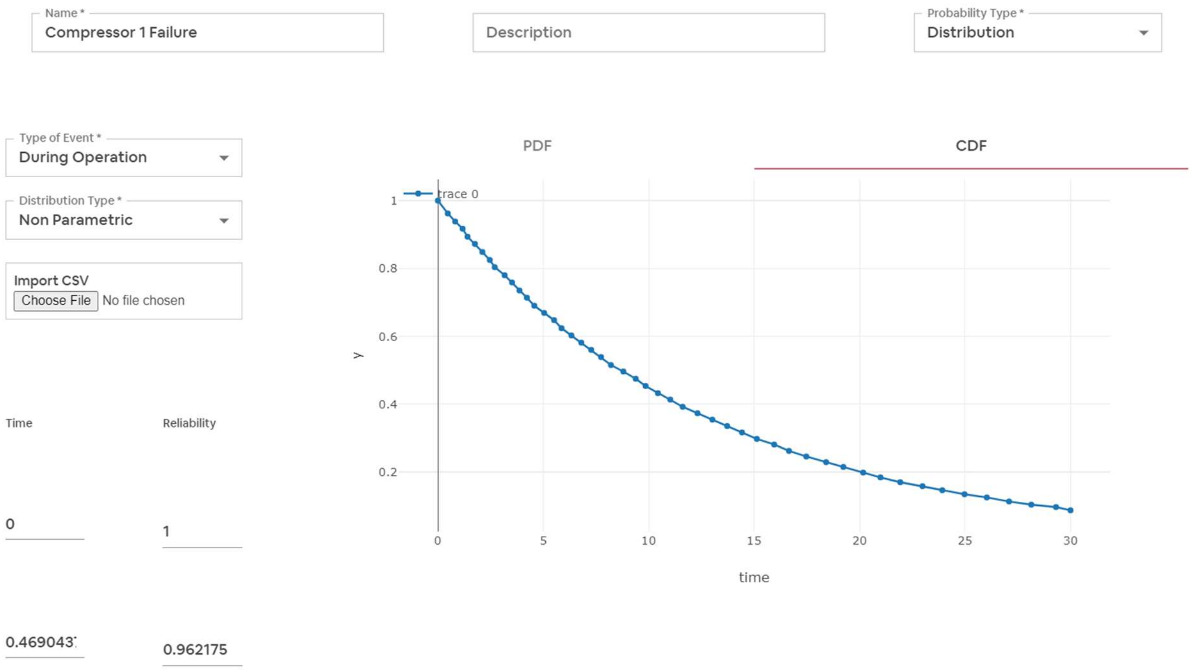

Name*: Compressor 1 Failure

Description

Probability Type*: Distribution

Type of Event*: During Operation

Distribution Type*: Non Parametric

Time	Reliability
0	1
0.469043	0.962175

Figure 10.9. Quantification for the compressor failure event

Natural force is defined using a lognormal probability distribution with a median of 0.00026266 and error factor of 5. Third-Party damage uses the same distribution type, with a median of 0.0075406 and error factor of 5.

The probability of the material defect and welding defect events are defined using a lognormal distribution as well, with a median of 0.0005688 for a material defect and 0.000523 for a welding defect. Both events have an error factor of 5.

10.4 Summary

This chapter introduced the Non-metallic Pipeline System Integrity Management tool (PSIM-NM) which was integrated with the existing online application of PSIM to allow the model developed by this work to be used publicly for real applications.

11 Conclusions and Future Work

As interest in using thermoplastic composite materials in the oil and gas industry grows, efforts to understand and predict the behavior of these materials under combined loading and environmental stresses have arisen in the form of numerous experimental, analytical, and numerical studies. Due to the complex nature of composite materials like TCP and RTP, however, there exists a research gap in connecting the environmental degradation resulting from exposure to factors such as fluids and elevated temperatures to the likelihood of failure over the lifetime of a pipe or segment.

In this research, I proposed a methodology for accounting for the effects of fluid absorption from interior and exterior oil and/or water, thermal degradation, and thermal softening on the mechanical properties of a pipe using a probabilistic Bayesian network model, which uses empirical data to estimate the range of potential degradation over a given time window. This methodology has been implemented in a pipe simulation model, which accepts inputs about the local temperature and fluid exposure conditions, as well as information about the pipe design and diffusion behavior, and predicts ranges of expected water and oil absorption, estimates degradation in the longitudinal, transverse, and shear stiffness, and determines the probability of ply failure under the defined loading conditions. Laminate failure was modeled using a progressive failure approach, in which the stiffness of the failed plies is greatly reduced over time, leading to higher stresses on the remaining undamaged plies. The results of each modeled process were compared with experimental data to verify the behavior of TCP and RTP specimens subjected to the same conditions as those in the model. It was found that the model accurately predicts pipe degradation under moderate conditions, but at high temperatures the model under-estimates the severity of material degradation. Future work is needed to improve the model's performance in these areas.

The simulation was built as a python code, which has been implemented as a new module within the existing Pipeline System Integrity Management (PSIM) web application. This module allows a user to input custom parameters for a pipe segment and simulate the fluid absorption, degradation, and laminate failure probability over time, allowing for uncertainty in the inputs, environmental conditions, and internal physical process parameters. The PSIM incorporates the laminate failure module as a part of a fault tree analysis for failure of a particular transmission phase; the fault tree analysis includes potential failure causes such as third-party damage, natural disasters, design faults, and compressor failures.

Future work is needed to continue to expand the modeling capabilities to include corrosive and abrasive elements in fluids such as acids, particulates, and bacteria. It is known that the presence of these factors can have significant impacts on fluid absorption and material degradation, but the extent to which these elements affect the material throughout the wall thickness can be difficult to predict, especially when factoring in the influence of polymer fillers. Another phenomenon that requires further work is the stiffening effect, which can occur when a polymer material is first exposed to elevated temperatures, which can result in additional curing, or to pressures, which can enhance consolidation of the laminate. Finally, expanding the degradation modeling to include the changes in the polymer glass transition temperature as fluid is absorbed is an important addition to this model that will be made in the future. In order to consider these factors, more data is required on the effects of corrosive and abrasive elements, both independently and in concert, on the performance of TCP and RTP laminates.

Additionally, within the thermomechanical modeling, future work to incorporate flexural and other non-axisymmetric loading modes is needed in order for this model to be usable for offshore flexible riser applications, where flexure is one of the primary loading mechanisms. Finally, future work is needed to complete the PSIM-NM tool, with the aim of including recommended maintenance practices and sensor optimization.

Appendix: Calculation of Strain Constants

This appendix details the equations used for solving the unknown constants of integration in the thermomechanical model developed by Bakaiyan et al.

For a laminate of *N* plies, of which an arbitrary ply k has the following strains in the $r, \theta,$ and z directions:

$$\varepsilon_r^{(k)} = \frac{du_r^{(k)}}{dr}$$

$$\varepsilon_\theta^{(k)} = \frac{u_r^{(k)}}{r}$$

$$\varepsilon_r^{(k)} = \frac{du_z^{(k)}}{dr} = \varepsilon_0$$

$$\gamma_{zr}^{(k)} = 0$$

$$\gamma_{\theta r}^{(k)} = \frac{du_\theta^{(k)}}{dr} - \frac{u_\theta^{(k)}}{r}$$

$$\gamma_{z\theta}^{(k)} = \frac{du_\theta^{(k)}}{dr} = \gamma_0 r$$

For an isotropic ply, the solution for u_r is:

$$u_r^{(k)} = D^{(k)}r + \frac{E^{(k)}}{r} + \left(\left(\frac{\lambda^{(k)}\ln r}{2} - \frac{\lambda^{(k)}}{4}\right)(A - T_\infty) + \frac{\xi_r^{(k)}}{4\bar{C}_{33}^{(k)}}(2A + 2B\ln r - B) + \frac{\lambda^{(k)}B}{4}\left((\ln r)^2 - \ln r + \frac{1}{2}\right)\right)r$$

Where the term λ is given by Equation 4.26.

$$\lambda^{(k)} = \frac{\xi_r^{(k)} - \xi_\theta^{(k)}}{\bar{C}_{33}^{(k)}}$$

For an orthotropic ply, the solution for u_r is:

$$u_r^{(k)} = D^{(k)} r^{\beta^{(k)}} + E^{(k)} r^{-\beta^{(k)}} + \alpha_1^{(k)} \varepsilon_0 r + \alpha_2^{(k)} \gamma_0 r^2 + \left(\eta^{(k)} (A - T_\infty) + \frac{\frac{B \xi_r^{(k)}}{\bar{C}_{33}^{(k)}} - 2\eta^{(k)} B}{1 - \beta^{(k)2}} + \eta^{(k)} B \ln r \right) r$$

The terms A and B are the temperature at the inner wall of the pipe and temperature delta, respectively.

The terms α_1, α_2, β, *and* η can be expressed are calculated from the transformed stiffness coefficients of the ply:

$$\alpha_1^{(k)} = \frac{\bar{C}_{12}^{(k)} - \bar{C}_{13}^{(k)}}{\bar{C}_{33}^{(k)} - \bar{C}_{22}^{(k)}}$$

$$\alpha_2^{(k)} = \frac{\bar{C}_{26}^{(k)} - 2\bar{C}_{36}^{(k)}}{4\bar{C}_{33}^{(k)} - \bar{C}_{22}^{(k)}}$$

$$\beta^{(k)} = \sqrt{\frac{\bar{C}_{22}^{(k)}}{\bar{C}_{33}^{(k)}}}$$

$$\eta^{(k)} = \frac{\lambda^{(k)}}{1 - \beta^{(k)2}}$$

The solution to the integration constants $D^{(k)}$, $E^{(k)}, \gamma_0$, and ε_0 is obtained from:

$$\begin{bmatrix} \varepsilon_0 \\ \gamma_0 \\ D^{(1)} \\ \dots \\ D^{(N)} \\ E^{(1)} \\ \dots \\ E^{(N)} \end{bmatrix} = [a]\backslash[b]$$

a is a *2N+2* by *2N+2* matrix and b is an array of size *2N+2*. The first two values of b have initial values calculated from the pressure P, axial force F, and moment M, which are later modified for each ply:

$$b^{(1)} = \frac{r^2 P}{2} + \frac{F}{2\pi} + \sum_k \left({\sigma_{z1}}^{(k)} - {\sigma_{z2}}^{(k)} \right)$$

$$b^{(2)} = \frac{M}{2\pi} + \sum_k \left({\tau_1}^{(k)} - {\tau_2}^{(k)} \right)$$

Likewise, the first two rows of a are calculated as follows. Note that for the following equations, the parameters $A^{(k)}$, alphabetically through $M^{(k)}$ are short-hands for equations which will be detailed in this appendix.

$$a^{(1,\ k)} = {E_2}^{(k)} - {E_1}^{(k)}$$

$$a^{(1,\ N+k)} = {F_2}^{(k)} - {F_1}^{(k)}$$

$$a^{(1,\ 2N+1)} = \sum_k \left({G_2}^{(k)} - {G_1}^{(k)} \right)$$

$$a^{(1,\ 2N+2)} = \sum_k \left({H_2}^{(k)} - {H_1}^{(k)} \right)$$

$$a^{(2,\ k)} = {J_2}^{(k)} - {J_1}^{(k)}$$

$$a^{(2,\ N+k)} = {K_2}^{(k)} - {K_1}^{(k)}$$

$$a^{(2,\ 2N+1)} = \sum_k \left({L_2}^{(k)} - {L_1}^{(k)} \right)$$

$$a^{(2,\ 2N+2)} = \sum_k \left({M_2}^{(k)} - {M_1}^{(k)} \right)$$

For all plies up to $k = N$, two unique values of b and rows of a are calculated, with the exception of the very first and last ply.

$$b^{(2k+2)} = {\sigma_{r,p}}^{(k)} - {\sigma_r}^{(k)}$$

$$b^{(2k+3)} = {u_p}^{(k)} - u^{(k)}$$

$$a^{(2k+2,\ k)} = {A_2}^{(k)}$$

$$a^{(2k+2,\ k+1)} = -{A_{1,p}}^{(k)}$$

$$a^{(2k+2,\ N+k)} = {B_2}^{(k)}$$

$$a^{(2k+2,\ N+k+1)} = -{B_{1,p}}^{(k)}$$

$$a^{(2k+2,\ 2N+1)} = C^{(k)} - {C_p}^{(k)}$$

$$a^{(2k+2,\ 2N+2)} = {D_2}^{(k)} - {D_{1,p}}^{(k)}$$

$$a^{(2k+3,\ k)} = {\mathcal{a}_2}^{(k)}$$

$$a^{(2k+3,\ k+1)} = -{\mathcal{a}_{1,p}}^{(k)}$$

$$a^{(2k+3,\ N+k)} = {\mathcal{b}_2}^{(k)}$$

$$a^{(2k+3,\ N+k+1)} = -{\mathcal{b}_{1,p}}^{(k)}$$

$$a^{(2k+3,\ 2N+1)} = {c_2}^{(k)} - {c_{1,p}}^{(k)}$$

$$a^{(2k+3,\ 2N+2)} = {d_2}^{(k)} - {d_{1,p}}^{(k)}$$

For $k = 1$, the 3rd row of a is calculated as:

$$b^{(3)} = -P - {\sigma_r}^{(k)}$$

$$a^{(3,\ 1)} = {A_1}^{(k)}$$

$$a^{(3,\ N+1)} = {B_1}^{(k)}$$

$$a^{(3,\ 2N+1)} = C^{(k)}$$

$$a^{(3,\ 2N+2)} = {D_1}^{(k)}$$

For $k = N$, only one row of a is calculated

$$b^{(2N+2)} = -{\sigma_r}^{(1)}$$

$$a^{(2N+2,\ N)} = {A_2}^{(k)}$$

$$a^{(2N+2,\ 2N)} = {B_2}^{(k)}$$

$$a^{(2N+2,\ 2N+1)} = C^{(k)}$$

$$a^{(2N+2,\ 2N+2)} = D_2{}^{(k)}$$

The unknowns above are calculated differently for isotropic and orthotropic plies. In the following equations, r_1 refers to the inner radius of the ply, r_2 to the outer radius, and $\bar{C}_{ij}^{(k)}$ to the compliance of the k^{th} ply in the *ij* direction.

Note: for ply 1, a modification of equations for all equations is used for $A_1{}^{(k)}$ through $D_1{}^{(k)}$and $\sigma_r{}^{(1)}$ which replaces r_2 with r_1

$$\eta_z^{(k)} = \bar{C}_{11}^{(k)}\alpha_1{}^{(k)} + \bar{C}_{12}^{(k)}\alpha_2{}^{(k)} + \bar{C}_{13}^{(k)}\alpha_3{}^{(k)} + 2\bar{C}_{16}^{(k)}\alpha_6{}^{(k)}$$

$$\eta_\theta^{(k)} = \bar{C}_{21}^{(k)}\alpha_1{}^{(k)} + \bar{C}_{22}^{(k)}\alpha_2{}^{(k)} + \bar{C}_{23}^{(k)}\alpha_3{}^{(k)} + 2\bar{C}_{26}^{(k)}\alpha_6{}^{(k)}$$

$$\eta_r^{(k)} = \bar{C}_{31}^{(k)}\alpha_1{}^{(k)} + \bar{C}_{32}^{(k)}\alpha_2{}^{(k)} + \bar{C}_{33}^{(k)}\alpha_3{}^{(k)} + 2\bar{C}_{36}^{(k)}\alpha_6{}^{(k)}$$

$$\eta_g^{(k)} = \bar{C}_{61}^{(k)}\alpha_1{}^{(k)} + \bar{C}_{62}^{(k)}\alpha_2{}^{(k)} + \bar{C}_{63}^{(k)}\alpha_3{}^{(k)} + 2\bar{C}_{66}^{(k)}\alpha_6{}^{(k)}$$

$$\lambda_k = \frac{\eta_r^{(k)} - \eta_\theta^{(k)}}{\bar{C}_{33}^{(k)}}$$

Isotropic Case:

$$A_2{}^{(k)} = \bar{C}_{23}^{(k)} + \bar{C}_{33}^{(k)}$$

$$\mathcal{a}_2{}^{(k)} = r_2$$

$$B_2{}^{(k)} = r_2{}^{-2}\left(\bar{C}_{23}^{(k)} - \bar{C}_{33}^{(k)}\right)$$

$$\mathcal{b}_2{}^{(k)} = \frac{1}{r_2}$$

$$C^{(k)} = \bar{C}_{13}^{(k)}$$

$$d_2{}^{(k)} = c_2{}^{(k)} = 0$$

$$D_2{}^{(k)} = r_2\bar{C}_{36}^{(k)}$$

$$\sigma_r{}^{(k)} = \left(\bar{C}_{23}^{(k)} + \bar{C}_{33}^{(k)}\right)\left(\frac{\lambda_k \ln(r_2)\,(A - T_i)}{2} + \frac{\eta_r^{(k)}(A + B\ln(r_2))}{2\bar{C}_{23}^{(k)}} + \frac{B\lambda_k(\ln(r_2)^2 - 1)}{4}\right)$$

$$+ \left(\bar{C}_{23}^{(k)} - \bar{C}_{33}^{(k)}\right)\left(-\frac{\lambda_k(A - T_i)}{4} - \frac{\eta_r^{(k)}B}{4\bar{C}_{33}^{(k)}} - \frac{B\lambda_k(\ln(r_2) + 0.5)}{4}\right) - \eta_r^{(k)}(A + B\ln(r_2) - T_i)$$

$$u^{(k)} = r_2\left(\left(\frac{\lambda_k \ln(r_2)}{2} - \frac{\lambda_k}{4}\right)(A - T_i) + \frac{\eta_r^{(k)}}{4\bar{C}_{33}^{(k)}}\left(2A + 2B\ln(r_2) - B\right) + \frac{B\lambda_k\left(\ln(r_2)^2 - \ln(r_2) + 0.5\right)}{4}\right)$$

$$E_2{}^{(k)} = \frac{r_2{}^2\left(\bar{C}_{12}^{(k)} + \bar{C}_{13}^{(k)}\right)}{2}$$

$$F_2{}^{(k)} = \left(\bar{C}_{12}^{(k)} - \bar{C}_{13}^{(k)}\right)\ln(r_2)$$

$$G_2{}^{(k)} = \frac{r_2{}^2\bar{C}_{11}^{(k)}}{2}$$

$$H_2{}^{(k)} = \frac{r_2{}^3\bar{C}_{16}^{(k)}}{3}$$

$$\sigma_z{}^{(k)} = \frac{r_2{}^2}{4}\left(\left(\bar{C}_{12}^{(k)} + \bar{C}_{13}^{(k)}\right)\left(\frac{\lambda_k(2\ln(r_2) + 1)(A - T_i)}{2} + \frac{\eta_r^{(k)}(2A + 2B\ln(r_2) - B)}{2\bar{C}_{33}^{(k)}} + \frac{B\lambda_k(2\ln(r_2)^2 - 2\ln(r_2) - 1)}{4}\right)\right.$$

$$\left. + \left(\bar{C}_{12}^{(k)} - \bar{C}_{13}^{(k)}\right)\left(-\frac{\lambda_k(A - T_i)}{2} - \frac{\eta_r^{(k)}B}{2\bar{C}_{33}^{(k)}} + \frac{B\lambda_k(-\ln(r_2) + 1)}{2}\right) - \eta_z^{(k)}(2A + 2B\ln(r_2) - B - 2T_i)\right)$$

$$J_2{}^{(k)} = \frac{r_2{}^3\left(\bar{C}_{26}^{(k)} + \bar{C}_{36}^{(k)}\right)}{3}$$

$$K_2{}^{(k)} = r_2\left(\bar{C}_{26}^{(k)} - \bar{C}_{36}^{(k)}\right)$$

$$L_2{}^{(k)} = \frac{r_2{}^3\bar{C}_{16}^{(k)}}{3}$$

$$M_2{}^{(k)} = \frac{r_2{}^4\bar{C}_{66}^{(k)}}{4}$$

$$\begin{aligned}\tau_2{}^{(k)} = \frac{r_2{}^3}{6}\Bigg(&\left(\bar{C}_{12}^{(k)} + \bar{C}_{13}^{(k)}\right)\left(\lambda_k(\ln(r_2) - 1/3)(A - T_i) + \frac{\eta_r^{(k)}(A + B\ln(r_2) - B/3)}{\bar{C}_{33}^{(k)}} + \frac{B\lambda_k(3\ln(r_2)^2 - 2\ln(r_2) - 7/3)}{6}\right) \\ &+ \left(\bar{C}_{12}^{(k)} - \bar{C}_{13}^{(k)}\right)\left(-\frac{\lambda_k(A - T_i)}{2} - \frac{\eta_r^{(k)}B}{2\bar{C}_{33}^{(k)}} + \frac{B\lambda_k(-6\ln(r_2) - 5)}{3}\right) - \frac{6\eta_g^{(k)}}{9}(3A + 3B\ln(r_2) - B - 3T_i)\Bigg)\end{aligned}$$

Orthotropic Case:

$$\omega_1 = \frac{\bar{C}_{12}^{(k)} - \bar{C}_{13}^{(k)}}{\bar{C}_{33}^{(k)} - \bar{C}_{22}^{(k)}}$$

$$\omega_2 = \frac{\bar{C}_{26}^{(k)} - 2\bar{C}_{36}^{(k)}}{4\bar{C}_{33}^{(k)} - \bar{C}_{22}^{(k)}}$$

$$\beta = \sqrt{\frac{\bar{C}_{22}^{(k)}}{\bar{C}_{33}^{(k)}}}$$

$$A_2{}^{(k)} = r_2{}^{\beta-1}\left(\bar{C}_{23}^{(k)} + \beta\bar{C}_{33}^{(k)}\right)$$

$$\mathcal{a}_2{}^{(k)} = r_2{}^{\beta}$$

$$B_2{}^{(k)} = r_2{}^{-\beta-1}\left(\bar{C}_{23}^{(k)} - \beta\bar{C}_{33}^{(k)}\right)$$

$$\mathcal{b}_2{}^{(k)} = r_2{}^{-\beta}$$

$$C^{(k)} = \bar{C}_{13}^{(k)} + \omega_1\left(\bar{C}_{23}^{(k)} + \bar{C}_{33}^{(k)}\right)$$

$$c_2{}^{(k)} = \omega_1 r_2$$

$$D_2{}^{(k)} = r_2\left(\bar{C}_{36}^{(k)} + 2\omega_2\bar{C}_{33}^{(k)} + \omega_2\bar{C}_{23}^{(k)}\right)$$

$$d_2{}^{(k)} = \omega_2 r_2{}^2$$

$$\sigma_r{}^{(k)} = \frac{B\bar{C}_{33}^{(k)}}{1 - \beta^2}\left(\lambda_k(A - T_i) + \frac{\eta_r^{(k)}B}{\bar{C}_{33}^{(k)}} - \frac{2B\lambda_k}{1 - \beta^2} + \lambda_k B\ln(r_2)\right) - \eta_r^{(k)}(A + B\ln(r_2) - T_i)$$

$$u^{(k)} = \frac{r_2}{1 - \beta^2}\left(\lambda_k(A - T_i) + \frac{\eta_r^{(k)}B}{\bar{C}_{33}^{(k)}} - \frac{2B\lambda_k}{1 - \beta^2} + B\lambda_k\ln(r_2)\right)$$

$$E_2{}^{(k)} = r_2{}^{\beta+1}\frac{\bar{C}_{12}^{(k)} + \beta\bar{C}_{13}^{(k)}}{\beta+1}$$

$$F_2{}^{(k)} = \frac{\left(\bar{C}_{12}^{(k)} - \beta\bar{C}_{13}^{(k)}\right)r_2{}^{-\beta+1}}{1-\beta}$$

$$G_2{}^{(k)} = \frac{r_2{}^2\left(\bar{C}_{11}^{(k)} + \omega_1\left(\bar{C}_{12}^{(k)} + \bar{C}_{13}^{(k)}\right)\right)}{2}$$

$$H_2{}^{(k)} = \frac{r_2{}^3(\bar{C}_{16}^{(k)} + 2\omega_2\bar{C}_{13}^{(k)} + \omega_2\bar{C}_{12}^{(k)})}{3}$$

$$\sigma_z{}^{(k)} = \frac{r_2{}^2}{2}\left(\frac{\bar{C}_{12}^{(k)} + \bar{C}_{13}^{(k)}}{1-\beta^2}\left(\lambda_k(A - T_i) + \frac{\eta_r^{(k)}B}{\bar{C}_{33}^{(k)}} - \frac{2B\lambda_k}{1-\beta^2} + \frac{\lambda_k B(2\ln(r_2) - 1)}{2}\right) + \frac{\lambda_k B\bar{C}_{13}^{(k)}}{1-\beta^2}\right.$$

$$\left. - \frac{\eta_z^{(k)}}{2}(2A + 2B\ln(r_2) - B - 2T_i)\right)$$

$$J_2{}^{(k)} = \frac{r_2{}^{\beta+2}\left(\bar{C}_{26}^{(k)} + \beta\bar{C}_{36}^{(k)}\right)}{\beta+2}$$

$$K_2{}^{(k)} = \frac{r_2{}^{-\beta+2}\left(\bar{C}_{26}^{(k)} - \beta\bar{C}_{36}^{(k)}\right)}{2-\beta}$$

$$L_2{}^{(k)} = \frac{r_2{}^3\left(\bar{C}_{16}^{(k)} + \omega_1\left(\bar{C}_{26}^{(k)} + \bar{C}_{36}^{(k)}\right)\right)}{3}$$

$$M_2{}^{(k)} = \frac{r_2{}^4(\bar{C}_{66}^{(k)} + 2\omega_2\bar{C}_{36}^{(k)} + \omega_2\bar{C}_{26}^{(k)})}{4}$$

$$\tau_2{}^{(k)} = \frac{r_2{}^3}{3}\left(\frac{\bar{C}_{12}^{(k)} + \bar{C}_{13}^{(k)}}{1-\beta^2}\left(\lambda_k(A - T_i) - \frac{\eta_r^{(k)}B}{\bar{C}_{33}^{(k)}} + \frac{2B\lambda_k}{1-\beta^2} + \frac{\lambda_k B(3\ln(r_2) + 1)}{3}\right) + \frac{\lambda_k B\bar{C}_{13}^{(k)}}{1-\beta^2}\right.$$

$$\left. - \frac{\eta_g^{(k)}}{3}(3A + 3B\ln(r_2) - B - 3T_i)\right)$$

The continuity equations, $A_{1,p}{}^{(k)}$, $\mathcal{a}_{1,p}{}^{(k)}$, $B_{1,p}{}^{(k)}$, $\mathcal{b}_{1,p}{}^{(k)}$, $C_p{}^{(k)}$, $c_{1,p}{}^{(k)}$, $D_{1,p}{}^{(k)}$, $d_{1,p}{}^{(k)}$, $\sigma_{r,p}{}^{(k)}$, and $u_p{}^{(k)}$ are calculated using modified versions of the equations above using the compliance matrix elements $\bar{C}_{ij}^{(k+1)}$ and thermal expansion coefficients ${\alpha_i}^{(k+1)}$ from the adjacent $(k+1)$ ply and r_2 as the radius.

For example, a complete b and a for a three-ply laminate would look like this:

$$\begin{bmatrix}
({E_2}^{(1)}-{E_1}^{(1)}) & ({E_2}^{(2)}-{E_1}^{(2)}) & ({E_2}^{(3)}-{E_1}^{(3)}) & ({F_2}^{(1)}-{F_1}^{(1)}) & ({F_2}^{(2)}-{F_1}^{(2)}) & ({F_2}^{(3)}-{F_1}^{(3)}) & \sum_{k=1}^{3}\left({G_2}^{(k)}-{G_1}^{(k)}\right) & \sum_{k=1}^{3}\left({H_2}^{(k)}-{H_1}^{(k)}\right) \\
({J_2}^{(1)}-{J_1}^{(1)}) & ({J_2}^{(2)}-{J_1}^{(2)}) & ({J_2}^{(3)}-{J_1}^{(3)}) & ({K_2}^{(1)}-{K_1}^{(1)}) & ({K_2}^{(2)}-{K_1}^{(2)}) & ({K_2}^{(3)}-{K_1}^{(3)}) & \sum_{k=1}^{3}\left({L_2}^{(k)}-{L_1}^{(k)}\right) & \sum_{k=1}^{3}\left({M_2}^{(k)}-{M_1}^{(k)}\right) \\
{A_1}^{(1)} & 0 & 0 & {B_1}^{(1)} & 0 & 0 & C^{(1)} & {D_1}^{(1)} \\
{A_2}^{(1)} & -{A_{1,p}}^{(1)} & 0 & {B_2}^{(1)} & -{B_{1,p}}^{(1)} & 0 & C^{(1)}-{C_p}^{(1)} & {D_2}^{(1)}-{D_{1,p}}^{(1)} \\
{\mathscr{a}_2}^{(1)} & -{\mathscr{a}_{1,p}}^{(1)} & 0 & {\mathscr{b}_2}^{(1)} & -{\mathscr{b}_{1,p}}^{(1)} & 0 & {c_2}^{(1)}-{c_{1p}}^{(1)} & {d_2}^{(1)}-{d_{1,p}}^{(1)} \\
0 & {A_2}^{(2)} & -{A_{1,p}}^{(2)} & 0 & {B_2}^{(2)} & -{B_{1,p}}^{(2)} & C^{(2)}-{C_p}^{(2)} & {D_2}^{(2)}-{D_{1,p}}^{(2)} \\
0 & {\mathscr{a}_2}^{(2)} & -{\mathscr{a}_{1,p}}^{(2)} & 0 & {\mathscr{b}_2}^{(2)} & -{\mathscr{b}_{1,p}}^{(2)} & {c_2}^{(2)}-{c_{1p}}^{(2)} & {d_2}^{(2)}-{d_{1,p}}^{(2)} \\
0 & 0 & {A_2}^{(3)} & 0 & 0 & {B_2}^{(3)} & C^{(3)} & {D_2}^{(3)}
\end{bmatrix}$$

$$\begin{bmatrix}
\dfrac{r^2P}{2}+\dfrac{F}{2\pi}+\sum_{k=1}^{3}\left({\sigma_{z1}}^{(k)}-{\sigma_{z2}}^{(k)}\right) \\
\dfrac{M}{2\pi}+\sum_{k=1}^{3}\left({\tau_1}^{(k)}-{\tau_2}^{(k)}\right) \\
-P-{\sigma_r}^{(1)} \\
{\sigma_{r,p}}^{(1)}-{\sigma_r}^{(1)} \\
{u_p}^{(1)}-u^{(1)} \\
{\sigma_{r,p}}^{(2)}-{\sigma_r}^{(2)} \\
{u_p}^{(2)}-u^{(2)} \\
-{\sigma_r}^{(3)}
\end{bmatrix}$$

References

[1] IEA, "Offshore Energy Outlook 2018," IEA, Paris, 2018.

[2] A. Somasekhar, "Offshore oil spending to rise more than 20% this year, SLB says," *Reuters,* 21 June 2023.

[3] AMPP, "Oil and Gas Production," [Online]. Available: https://www.ampp.org/resources/what-is-corrosion/corrosion-reference-library/oil-gas. [Accessed 15 October 2022].

[4] G. Marsh, "Thermoplastic composite solution for deep oil and gas reserves," *Reinforced Plastics,* pp. 26-29, July/August 2013.

[5] J. Osborne, "Thermoplastic pipes - lighter, more flexible solutions for oil and gas extraction," *Reinforced Plastics,* pp. 33-38, January/February 2013.

[6] A. Gibson, "The Cost Effective Use of Fibre Reinforced Composite Materials Offshore," University of Newcastle Upon Tyne, 2002.

[7] S. Feih and e. al., "Testing Procedure for the Single Fiber Fragmentation Test," Forskningscenter Risø: Denmark, 2004.

[8] T. Anderson, M. Vermilyea, J. N. Dodds, D. Finch and J. Latto, "Qualification of Flexible Fiber-Reinforced Pipe for 10,000-Foot Water Depths," in *Offshore Technology Conference*, Houston, Texas, 2013.

[9] J. Wilkins, "Qualification of Thermoplastic Composite Pipes," in *ASME 2018 37th International Conference on Ocean, Offshore and Arctic Engineering*, Madrid, Spain, 2018.

[10] J. de Kanter and J. Leijten, "THERMOPLASTIC COMPOSITE PIPE: ANALYSIS AND TESTING OF A NOVEL PIPE SYSTEM FOR OIL & GAS," in *ICCM 17*, Edinburgh, UK, 2009.

[11] W. D. Callister and D. G. Rethwisch, Fundamentals of Materials Science and Engineering: An Integrated Approach, John Wiley & Sons, Inc., 2019.

[12] B.V. and P.N., "What is a Reinforced Thermoplastic Pipe (RTP) or Flexible Composite Pipe (FCP)?," Soluforce, 2020. [Online]. Available: www.soluforce.com/soluforce/benefits/What-is-RTP/What-is-Reinforced-Thermoplastic-Pipe-RTP.php..

[13] M. Kremers, "A brief history of Thermoplastic Composite Pipe," 27 March 2017. [Online]. Available: https://www.linkedin.com/pulse/brief-history-thermoplastic-composite-pipe-marcus-kremers. [Accessed 4 December 2022].

[14] DNV, *Thermoplastic composite pipes,* DNV, 2018.

[15] DNV, *Composite Components,* DNV, 2013.

[16] American Petroleum Institute, *Specification for unbonded flexible pipe (API 17J),* 2014.

[17] American Petroleum Institute, *Qualification of spoolable reinforced plastic line pipe (API 15S),* 2013.

[18] M. van Onna, J. de Kanter and B. Steuten, "Advancements in Thermoplastic Composite Riser Development," in *ASME 2012 31st International Conference on Ocean, Offshore and Arctic Engineering*, Rio de Janeiro, Brazil, 2012.

[19] D. D. N. Qi, X. Cai, H. Li, Z. Shuhui and M. Yan, "Application and Qualification of Reinforced Thermoplastic Pipes in Chinese Oilfields," in *International Conference on*

Pipelines and Trenchless Technology, Beijing, China, 2011.

[20] D. Qi, H. Li, X. Cai, N. Ding and S. Zhang, "Application of Non-metallic Composite Pipes in Oilfields in China," in *International Conference on Pipelines and Trenchless Technology*, Wuhan, China, 2012.

[21] "Damage Tolerance and Durability of Composites," 2013.

[22] J. de Kanter and J. Leijten, "Thermoplastic Composite Pipe: Analysis and Testing of a Novel Pipe System for Oil & Gas".

[23] API-5L, *Specification for Line Pipe.*

[24] S. Wang, L. Yao and X. Meng, "Bending Mechanical Behavior Analysis of Glass-Fiber Reinforced Thermoplastic Pipe Based on a Nonlinear Solid Element Model," *Journal of Marine Science and Technology,* vol. 26, no. 4, pp. 575-586, 2018.

[25] K. Yu, E. Morozov, M. Ashraf and K. Shankar, "Analysis of flexural behaviour of reinforced thermoplastic pipes considering material nonlinearity," *Composite Structures,* vol. 119, pp. 385-393, 2015.

[26] J. C. Hastie, I. A. Guz and M. Kashtalyan, "Numerical modelling of spoolable thermoplastic composite pipe (TCP) under combined bending and thermal load," *Ships and Offshore Structures,* p. DOI: 10.1080/17445302.2021.1958534, 2021.

[27] M. Raji, N. Zari, R. Bouhfid and A. e. k. Qaiss, "Durability of composite materials during hydrothermal and environmental aging," in *Durability and Life Prediction in Biocomposites, Fibre-Reinforced Composites and Hybrid Composites*, 2019, pp. 83-119.

[28] H. GangaRao and R. Liang, "Creep response characterization and life prediction of GFRP composites under bending. Research and application of composite materials in

infrastructure," in *The Workshop on Global Innovations in Infrastructure with Advanced Composites*, Nanjing, China, 2014.

[29] D. o. D. -. S. Practice, "MIL-STD-889 - Dissimilar Metals," 22 August 2016. [Online]. Available: https://roofonline.com/building-components/metal-technical-information/milstd889c-department-of-defense-standard-practice-dissimilar-metals/. [Accessed 8 October 2022].

[30] R. Ouellette and J. Rawn, "12 - Amines and Amides," Boston, Elsevier, 2015, pp. 315-342.

[31] A. Berens and H. Hopfenberg, "Diffusion and relaxation in glassy polymer powders: 2. Separation of diffusion and relaxation parameters," *Polymer,* vol. 19, pp. 489-496, 1978.

[32] L. Kumosa, B. Benedikt, D. Armentrout and e. al., "Moisture absorption properties of unidirectional glass/polymer composites used in composite (non-ceramic) insulators," *Composites A: Applications,* vol. 35, pp. 1049-1063, 2004.

[33] J. Wang, H. GangaRao, R. Liang and W. Liu, "Durability and prediction models of fiber-reinforced polymer composites under various environmental conditions: A critical review," *Journal of Reinforced Plastics & Composites,* vol. 35, no. 3, pp. 179-211, 2016.

[34] S. Kajorncheappunngam, "The effects of environmental aging on the durability of glass/epoxy composites," PhD Thesis, West Virginia University, USA, 1999.

[35] J. Zhou, X. Chen and S. Chen, "Durability and service life prediction of GFRP bars embedded in concrete under acid environment," *Journal of Nuclear Engineering Design,* vol. 241, pp. 4095-4102, 2011.

[36] G. Wu, Z. Dong, X. Wang and e. al., "Prediction of long-term performance and durability of BFRP bars under the combined effect of sustained load and corrosive solutions," *Journal of*

Composites Construction, vol. 19, p. 04014058, 2015.

[37] Y. Bai, T. Keller and T. Vallee, "Modeling of stiffness of FRP composites under elevated and high temperatures," *Composites Science Technology,* vol. 68, pp. 3099-3106, 2008.

[38] J. Jansen, "Plastic Failure through Molecular Degradation," January 2015. [Online]. Available: http://read.nxtbook.com/wiley/plasticsengineering/january2015/consultantscorner.html. [Accessed 29 November 2022].

[39] V. Jha, N. Dodds, D. Finch, J. Latto, G. Karabelas, T. Anderson, P. Baehmann and M. Vermilyea, "Flexible Fiber-reinforced Pipe for 10,000-foot Water Depths: Performance Assessments and Future Challenges," in *Offshore Technology Conference*, Houston, Texas, 2014.

[40] M. Farshad, "New Automated Long-term Extrapolation Method for Plastic Pipes under Hydrostatic Pressure," *Journal of Thermoplastic Composite Materials,* vol. 19, pp. 569-574, 2006.

[41] R. L. Mazur, P. C. Oliveira, M. C. Rezende and E. C. Botelho, "Environmental effects on viscoelastic behavior of carbon fiber/PEKK thermoplastic composites," *Journal of Reinforced Plastics & Composites,* vol. 33, no. 8, pp. 749-757, 2014.

[42] M. Arhant, P. Davies, C. Burtin and C. Briancon, "Thermoplastic Matrix Composites for Underwater Applications," in *20th International Conference on Composite Materials*, Copenhagen, 2015.

[43] X. Gabrion, V. Placet, F. Trivaudey and L. Boubakar, "About the thermomechanical behaviour of a carbon fibre reinforced high-temperature thermoplastic composite,"

Composites Part B, vol. 95, pp. 386-394, 2016.

[44] M. Eftekhari and A. Fatemi, "Tensile behavior of thermoplastic composites including temperature, moisture, and hygrothermal effects," *Polymer Testing,* vol. 51, pp. 151-164, 2016.

[45] A. Bahtui, K. Kidykas, J. Richardson and J. Wilkins, "Qualification of Thermoplastic Composite Risers: Combined Pressure and Bending Loading," in *ASME 2019 38th International Conference on Ocean, Offshore and Arctic Engineering*, Glasgow, Scotland, 2019.

[46] M. Robert, R. Roy and B. Benmokrane, "Environmental Effects on Glass Fiber Reinforced Polypropylene Thermoplastic Composite Laminate for Structural Applications," *Polymer Composites,* pp. 604-611, 2010.

[47] H. Bel Haj Frej, R. Léger, D. Perrin and P. Ienny, "A Novel Thermoplastic Composite for Marine Applications: Comparison of the Effects of Aging on Mechanical Properties and Diffusion Mechanisms," *Applied Composite Materials,* vol. 28, pp. 899-922, 2021.

[48] M. A. A. Bakar, Z. Mustaffa, N. N. Idris and M. E. A. B. Seghier, "Experimental program on the burst capacity of reinforced thermoplastic pipe (RTP) under impact of quasi-static lateral load," *Engineering Failure Analysis,* vol. 128, p. 105626, 2021.

[49] E. Spencer, "Understanding the Mechanical Properties of Fibre-Matrix Interfaces in Flexible Composite Pipe Materials," Department of Materials Imperial College London, London, 2021.

[50] Y. Bai, N. Wang, P. Cheng, B. Yu, M. Badaruddin and M. Ashri, "Collapse of Reinforced Thermoplastic Pipe (RTP) Under External Pressure," in *ASME 30th International*

Conference on Ocean, Offshore and Arctic Engineering, Rotterdam, The Netherlands, 2011.

[51] Y. Bai, W. Xu, P. Cheng, N. Wang and W. Ruan, "Behaviour of reinforced thermoplastic pipe (RTP) under combined external pressure and tension," *Ships and Offshore Structures,* vol. 9, no. 4, pp. 464-474, 2014.

[52] Y. Bai, B. Yu, P. Cheng, N. Wang, W. Ruan, J. Tang and A. Babapour, "Bending Behavior of Reinforced Thermoplastic Pipe," *Journal of Offshore Mechanics and Arctic Engineering,* vol. 137, p. 021701, 2015.

[53] H. Xia, C. Shi, J. Wang, X. Bao, H. Li and G. Fu, "Effect of Thickness and Winding Angle of Reinforcement Laminates on Burst Pressure Capacity of Thermoplastic Composite Pipes," *Journal of Offshore Mechanics and Arctic Engineering,* vol. 143, p. 151802 (8), 2021.

[54] C. Shi, H. Xia, J. Wang, X. Bao, H. Li and G. Fu, "Partially-plastic theoretical model of thermoplastic composite pipes and comparison of composite failure criteria," *Composite Structures,* vol. 280, p. 114834, 2022.

[55] J. C. Hastie, M. Kashtalyyan and I. A. Guz, "Failure analysis of thermoplsatic composite pipe (TCP) under combined pressure, tension and thermal gradient for an offshore riser application," *International Journal of Pressure Vessels and Piping,* vol. 178, p. 103998, 2019.

[56] H. Qiao, Y. Zhang, Y. Bai, P. Cheng, Y. Lu and P. Han, "Study on reinforced thermoplastic pipe under combined tension and internal pressure," *Ships and Offshore Structures,* vol. 13, pp. 86-97, 2018.

[57] Y. Wang, M. Lou and Y. Wang, "Stochastic analysis of failure pressure in reinforced

thermoplastic pipes under axial loading and external pressure," *Ocean Engineering,* vol. 240, p. 109963, 2021.

[58] J. Wang, C. Shi, G. Fu, Z. Liu, X. Bao and H. Li, "Numerical Evaluation on Lateral Impact Resistance of Thermoplastic Composite Pipes in terms of Internal Pressure Capacity," in *ASME 2020 39th International Conference on Ocean, Offshore and Arctic Engineering*, Virtual, Online, 2020.

[59] H. Bakaiyan, H. Hosseini and E. Ameri, "Analysis of multi-layered filament-wound composite pipes under combined internal pressure and thermomechanical loading with thermal variations," *Composite Structures,* vol. 88, pp. 532-541, 2009.

[60] D. Beniaguev, "Historical Hourly Weather Data," 2017. [Online]. Available: https://www.kaggle.com/datasets/selfishgene/historical-hourly-weather-data?select=temperature.csv. [Accessed May 2023].

[61] P.-Y. Le Gac, M. Arhant, M. Le Gall and P. Davies, "Yield Stress Changes Induced by Water in Polyamide 6: Characterization and Modeling," *Polymer Degradation and Stability,* vol. 137, pp. 272-280, 2017.

[62] H. Xin, H. Mosallam, Y. Liu and e. al., "Mechanical characterization of a unidirectional pultruded composite lamina using micromechanics and numerical homogenization," *Construction Building Materials,* no. 216, pp. 101-118, 2019.

[63] G. Shen, G. Hu and B. Liu, in *Mechanics of Composite Materials, second ed.*, Beijing, Tsinghua University Press, 2006.

[64] V. Jha, D. Finch, N. Dodds and J. Latto, "Optimized Hybrid Composite Flexible Pipe for Ultra-Deepwater Applications," in *ASME 34th International Conference on Ocean,*

Offshore and Arctic Engineering, St. John's, Newfoundland, Canada, 2015.

[65] C. Herakovich, Mechanics of Fibrous Composites, New York: Wiley, 1997.

[66] J. Hastie, I. Guz and M. Kashtalyan, "Effects of thermal gradient on failure of a thermoplastic composite pipe (TCP) riser leg," *International Journal of Pressure Vessels and Piping,* vol. 172, pp. 90-99, 2019.

[67] S. C. Tan and J. Perez, "Progressive Failure of Laminated Composites with a Hole under Compressive Loading," *Journal of Reinforced Plastics and Composites,* vol. 12, no. 10, 1993.

[68] K.-Y. Wu, "Reliability-Based Integrity Management of Natural Gas Pipelines Subject to Spatio-Temporal Corrosive Environment," PhD Dissertation, University of California, Los Angeles, 2020.

[69] W. Chalgham, "System-Level Prognosis and Health Monitoring Modeling Framework and Software Implementation for Gas Pipeline System Integrity Management," Ph.D Thesis Mechanical Engineering, University of California, Los Angeles, 2020.

[70] Y. Tu and A. Ouano, "Model for the Kinematics of Polymer Dissolution," *IBM Journal of Research Development,* pp. 131-142, 1977.

[71] Y. Tu, "A Multi-Phase Stefan Problem Describing the Swelling and Dissolution of Glassy Polymer," *Quarterly ofo Applied Mathematics,* pp. 269-285, 1977.

[72] M. Arhant, C. Briancon, C. Burtin and P. Davies, "Carbon/polyamide 6 thermoplastic composite cylinders for deep sea applications," *Composite Structures,* vol. 212, pp. 535-546, 2019.

[73] A. Mubashar, I. Ashcroft, G. Critchlow and e. al., "Moisture absorption-desorption effects

in adhesive joints," *Int J Adhes Adhes,* vol. 29, pp. 751-760, 2009.

[74] V. Karbhari and G. Xian, "Hygrothermal effects on high V (F) pultruded unidirectional carbon/epoxy composites: moisture uptake," *Composites B: Engineering,* vol. 40, pp. 41-49, 2009.

[75] X. Jiang, H. Kolstein and F. Bijard, "Moisture diffusion in glass-fiber-reinforced polymer composite bridge under hot/wet environment," *Composites B: Engineering,* vol. 45, pp. 407-416, 2013.

[76] B. A. Miller-Chou and J. L. Koenig, "A review of polymer dissolution," *Progress in Polymer Science,* vol. 28, pp. 1223-1270, 2003.

[77] M. Mohvaldin, M. Ismail and E.-K. Noaman, "Evaluation of Different Modelling Methods Used for Erosion Prediction," NACE, Shanghai, China, 2011.

[78] "Delamination," Wikipedia, September 2022. [Online]. Available: https://en.wikipedia.org/wiki/Delamination. [Accessed 29 November 2022].

[79] H. Ashrafizadeh, R. Schultz, B. Xu and P. Mertiny, "Development of a Novel Technique Using Finite Element to Simulate Creep in Thermoplastic Fiber Reinforced Polymer Composite Pipe Structures".